UC Berkeley
UC Berkeley Electronic Theses and Dissertations

Title
Fluids for Soft Gripper Design: Robots in Real-World Environments

Permalink
https://escholarship.org/uc/item/5n36j278

Author
Li, Monica Shaojin

Publication Date
2023

Peer reviewed|Thesis/dissertation

Fluids for Soft Gripper Design: Robots in Real-World Environments

By

Monica Shaojin Li

A dissertation submitted in partial satisfaction of the

requirements for the degree of

Doctor of Philosophy

in

Engineering Science - Mechanical Engineering

in the

Graduate Division

of the

University of California, Berkeley

Committee in charge:

Professor Hannah Stuart, Chair
Professor Oliver O'Reilly
Professor Ronald Fearing

Summer 2023

Fluids for Soft Gripper Design: Robots in Real-World Environments

Abstract

Fluids for Soft Gripper Design: Robots in Real-World Environments

by

Monica Shaojin Li

Doctor of Philosophy in Engineering Science - Mechanical Engineering

University of California, Berkeley

Professor Hannah Stuart, Chair

For forceful and dexterous manipulation, robots must be able to physically interact with the environment. In the real-world, the environment is dynamic and unstructured. For example, fragile objects and adversarial contact conditions, e.g. a slippery fluid film, may be present. Embodied intelligence and active control strategies are two approaches that tackle these challenges. Soft robots and grippers exemplify embodied intelligence, as the inherent behavior of soft materials allows passive compliance and distributed loading. A sense of touch, also known as tactile sensing, provides feedback for active controllers to provide additional adaptability and articulation. Human hands seamlessly integrate both compliance and tactile sensing, with underactuated joints and soft compliant skin covered with nerve endings. While case studies demonstrate soft robots or tactile sensors in the field, few systems have both.

My dissertation explores the design of embodied dexterity and tactile sensing in robots through fluids. Fluids – liquids, gasses – are ubiquitous. Many soft robots use fluids for actuation, e.g. pneumatic or hydraulic. Fluids for robotic sensing and contact design are less prevalent. In this dissertation, I first present how we can employ airflow for tactile sensing. This design uses pneumatic acoustic resonance to sensitize soft, skin-like surfaces and grippers. I then show how we can mitigate the slippery effects of lubrication for frictional grasping by adding soft, patterned finger pads to existing grippers.

Contents

List of Figures

List of Tables

Acknowledgments

I give my deepest and most sincere appreciation to my advisor, Hannah Stuart. First and foremost for her unconditional support and contagious enthusiasm. From Hannah, I have learned how to conduct scientific research in the context of engineering and robotics, and communicate it in an effective way. I hope we keep in touch for the many years to come.

I want to thank Oliver O'Reilly and Ron Fearing for sitting on my dissertation committee. Oliver welcomed me into the Berkeley community and has supported my studies since I was a prospective graduate student. Ron's expertise and insight in robotics helped frame my research along prior work. I also want to thank my qualifying exam committee: Reza Alam, Oliver O'Reilly, Dennis Lieu, and Suncica Canic for working with me and accommodating the remote nature of the COVID-19 pandemic. Thanks to the mechanical engineering staff: the administration and the student machine shop, especially Yawo, Dennis and Tom.

Thanks to the NASA Space Technology Research Fellowship (NSTRF) through which I had the opportunity to work with my mentors and collaborators at the Jet Propulsion Laboratory: Chris, Paul, Spencer, Arash, Patrick, Skylar (Caltech), and Laurie. Thanks to the collaborators I met through marine field testing: Pim, Ale, Rene, and Vincent. Space and the ocean will forever pique my curiosity.

Thanks to my wonderful labmates in the Embodied Dexterity Group, pictured in Appendix B.2. Special thanks to Tae, who lent his expertise in tactile sensing and to Michael, Laura, and Cyndia, the cubical cube that kept me company in the basement of Etcheverry. To my friends and family, especially Max and Val, for I could not have done it without you. Lastly, thanks to Berkeley for being in such a beautiful location. Though I will miss my afternoon jogs in the East Bay hills and weekend trips to Marin and the Sierras, I feel fortunate to have made the friends and memories from these adventures.

Chapter 1

Introduction

Humans first developed robots for industrial applications and operation in controlled environments, such as automotive factories and laboratories [84]. We envision and are developing robots for operation in unstructured environments, i.e. the real-world. These robots could explore and sample otherwise inaccessible areas such as the deep ocean [37, 125] and the Martian surface [80]. Deploying real-world robots is still an open challenge [8]. For instance, robots must adapt to external disturbances that may result in unintentional collisions. Grasped objects may be fragile and have adversarial contact conditions, e.g. covered in a slippery fluid film. My dissertation tackles these challenges by focusing on the physical contact interface between robot and world.

In these dynamic and unstructured real-world environments, robots must be adaptable and able to react to external stimulus. Two approaches address adaptability at the contact: embodied intelligence and active control. Systems with embodied intelligence have a physical morphology that passively adapts and complies to its surroundings [14]. Embodied intelligence also corresponds to underactuation, where more degrees of freedom than degrees of actuation give the system passive compliance. One example of embodied intelligence is the Universal Gripper, which can gently pick up various shaped objects with binary control input without sensing [12]. Other soft grippers passively comply to grasp fragile objects [117, 1, 109] and have been tested in the field [37]. The human hand is also soft and underactuated [36]. At the same time, it is covered with nerve endings that provide feedback for active control. Tactile sensing, or a sense of touch, is critical for human manipulation [51] as well as for advanced, real-world robots [20, 70].

Human hands have passive compliance and tactile sensing seamlessly integrated together, enabling execution of tasks with high dexterity. Implementation of tactile sensors on robot grippers is often in the form of electronic components at the contact location [23], requiring wires to be routed from the contact to the rest of the robot body. These wires, as well as the sensors themselves, may break from fatigue loading or unintentional collisions, as noted in Cutkosky and Provancher [20] and from personal experience. Researchers have equipped robots with tactile sensing without electronics near the contact using suction flow for underwater sensing [79] and pressure sensing in fluid-innervated soft structures [123]. In

Chapter 2, I present a tactile sensor for soft skin-like surfaces with no electronics near the contact. I extend this tactile sensor design to soft grippers in Chapter 3. This sensor is pneumatically actuated, as are many soft grippers.

In addition to sensing, robots impart forces to the environment at the contact. Thus, designing for contact and adversarial contact conditions is critical for real-world robots [18]. Grippers can pickup objects with two frictional contacts [77]. But with liquids present, these contact surfaces may become slippery and exhibit low friction due to fluid lubrication. While researchers have designed robotic surfaces to exert high shear forces [3, 92], these structures fail to function on smooth, unclean surfaces. In Chapter 4, I show how adding soft surface features to existing robotic grippers can increase friction for grasping smooth objects in wet or submerged conditions.

I summarize my dissertation contributions and discuss directions for future work in Chapter 5. In addition to my dissertation, during my PhD I designed a gripper for marine sampling on a small mobile vehicle and conducted field expeditions testing these robotic systems. I present this work in Appendix A and share photos from field testing and my graduate studies in Appendix B.

1.1   List of publications

The results presented in this dissertation have been taken from a number of publications from the same author.

- Chapter 2 is based on:

    – M. Li and H. S. Stuart. "AcousTac: Tactile sensing with acoustic resonance for electronics-free soft skin." *Soft Robotics.* [under review]

- Chapter 3 is based on:

    – M. Li, T. M. Huh, C. R. Yahnker, H. S. Stuart. "Resonant pneumatic tactile sensing for soft grippers." *Robotics and Automation Letters.* 2022, vol. 7, no.4, pp. 10105-10111 © 2022 IEEE

- Chapter 4 is modified from:

    – M. Li, D. Melville, E. Chung, H. S. Stuart. "Milliscale Features Increase Friction of Soft Skin in Lubricated Contact." *Robotics and Automation Letters.* 2020, vol. 5, no. 3, pp. 4781-4787 © 2020 IEEE

- Appendix A is based on:

    – M. Li, R. van der Zande, A. Hernández-Agreda, P. Bongaerts and H. S. Stuart, "Gripper Design with Rotation-Constrained Teeth for Mobile Manipulation of Hard, Plating Corals with Human-Portable ROVs," *OCEANS 2019 - Marseille, France.* 2019, pp. 1-6 © 2019 IEEE

Chapter 2

Tactile sensing for soft skin

Sound is a rich information medium that transmits through air; people communicate through speech and can even discern material through tapping and listening. To capture frequencies in the human hearing range, commercial microphones typically have a sampling rate of over 40kHz. These accessible acoustic technologies are not yet widely adopted for the explicit purpose of giving robots a sense of touch. Some researchers have used sound to sense tactile information, both monitoring ambient soundscape and with embedded speakers and microphones to measure sounds within structures. However, these options commonly do not provide a direct measure of steady state force, or require electronics integrated somewhere near the contact location. In this work, we present AcousTac, an acoustic tactile sensor for electronics-free force sensitive soft skin. Compliant silicone caps and plastic tubes compose the resonant chambers that emit pneumatic-driven sound measurable with a conventional off-board microphone. The resulting frequency changes depend on the external loads on the compliant end caps. Non-idealized vibration of the caps results in a boundary condition transition when first making contact, initially producing nonmonotonic signals. We characterize two solutions – adding a distal hole and mass to the cap – resulting in monotonic and nonhysteretic force readings with this technology. We can tune each AcousTac taxel to specific force and frequency ranges, based on geometric parameters, including tube length and end-cap geometry and thus uniquely sense each taxel simultaneously in an array. We demonstrate AcousTac's functionality on two robotic systems: a 4-taxel array and a 3-taxel astrictive gripper. Simple to implement with off-the-shelf parts, AcousTac is a promising concept for force sensing on soft robotic surfaces, especially in situations where electronics near the contact are not suitable. Equipping robots with tactile sensing and soft skin provides them with a sense of touch and the ability to safely interact with their surroundings.

2.1 Introduction

Soft robotic surfaces and skins generate inherent safety useful in human robot physical interaction and interaction with fragile objects [89]. Soft systems and mechanisms physically

embody the ability to adapt to dynamic and unexpected loads through passive compliance [60, 100]. As a result, soft robots also exhibit durability in harsh environments [121]. This motivates the development of soft, compliant coverings for otherwise rigid robots, for both robot and environmental safety. For example, the CoboSkin includes variable stiffness inflatable units to tune impact dynamics [90]. A recent review by Niiyama points out how soft skin is essential for humanoid robot application[83]. Yet, these hardware solutions are slow to translate to industrial settings, as compared with sensing and software based collision avoidance [108]. The design of soft skins for various robotic applications therefore remains a relevant area for ongoing development.

Artificial skin can also provide robots with a sense of touch that enables adaptive control for dexterous manipulation tasks [22]. Composition of sensitive skins relies on a wide variety of materials, including those with resistive, piezoelectric, and magnetic properties; the history and breadth of tactile sensor design is reviewed in chapters, reports, and books [20, 46, 23, 128]. Skin with channels filled with liquid-phase gallium-indium alloy is one method for generating sensitive skin, in which overlaid channel patterns are individually sensitive to unidirectional strain and contact pressure [91]. Numerous other works utilize bulk resistivity and embed cavities of conductive material in soft structures, where contact forces change the shape and therefore resistance [124, 38, 57]. All of these works describe a direct electronics-based measurement of the contact point. For skin made of multiple materials, challenges arise regarding the durability of traditional electronics, integration of soft and hard conductive materials without failure from stress concentrations or fatigue at connectors, and long-term life and reliability of experimental new materials at the contact point [99, 23]. Early development of self-healing soft tactile skin combats some of these durability issues [69].

Removing electronics and delicate materials from the contact point altogether represents another approach to generating mechanically resilient touch sensation. Various options place an intermediary material between physical stimuli and electric transducers to achieve such isolation. For example, recent work by Sun, et al. generated a camera-based structure, as a successor technology to GelSight [134], that shifts the camera to the base of the finger; it provides an indirect measure of force while improving mechanical durability of the appendage [115]. Pneumatics and hydraulics are another avenue for transmitting data throughout soft structures for remote sensing. Monitoring the pressure in a closed fluidic system provides rich tactile sensing information [123, 32]. In open fluidic tactile sensors, flow rate monitoring discerns object presence and surface characteristics for underwater [79] and in air [47] applications. In these examples, transducers are physically in-line with flow or pressure differential tubes routed away from the contact location. Vibrations transmitted through structures provide yet another method specialized for dynamic tactile sensing [21]. Resonant frequency-based contact detection informs robotic reaching and grasping, such as work by Backus, et al. that used accelerometers in compliant fingers [4]. Such vibration measurements require the vibrations to transmit effectively through the robotic structure itself.

Beyond the use of sight, pressure, or structural vibrations to measure contact from a distance, sound is another medium through which to measure touch. Sound, generated

through either the active or passive emission, can be measured with a microphone. The sounds of two surfaces sliding across each other tell us about relative movement and the material type, shown for rigid-rigid contact in [25]. Coincidental noise during manipulation can even be used to provide force feedback during teleoperation [104]. These signals change with material properties, and do not provide a direct measure of either static or dynamic contact forces. In an active sensing application, a receiver monitors the ultrasound signal transmitted through an air cavity, that changes with stress in the surrounding compliant material [106]. Researchers embed a microphone in a soft pneumatic finger and later add an embedded speaker that outputs a frequency sweep to detect contact with high spatial resolution [127, 135]. Acoustic vibrations between robots assist in shared communication and coordination [26]. These active acoustic examples achieve more specific measurands than in passive sound generation, however the emitter/receiver pairs are embedded or located in close proximity to the contact.

In the present work, we present AcousTac, an active, pneumatically-driven, acoustic tactile sensing method suitable for force measurements using a generic microphone located outside the skin. The idea is that robots, with a regulated air supply and a built-in microphone on the body, can include this sensing modality without the addition of new electronics. Instead of using an electronic sound emitter, we take inspiration from wind instruments to produce sound at the skin. Air-driven resonance is an ancient concept, with musical instruments emerging thousands of years ago.[1] In recent years, researchers have used simulations to model and design musical instruments [30, 33]. We design a tactile array using air-driven pipe resonance, because it is based on a simple theoretical model and uncomplicated to fabricate. This design has no electronic components at the contact area, removing the need to robustly integrate fragile components and route wires in soft skin. In our prior work, we generated such resonance in tubes along the length of a soft finger in order to detect the pose and fingertip contact, and estimate force with a fully-rigid probe [64]. The present work represents the first study looking at this modality for force sensitive soft skin, and includes new observations about how resonant modes and sound of a soft structure change when interacting with an object.

Overview

In Section 2.2, we describe the theoretical basis for AcousTac design, which includes models of taxel length and resonant frequency, relationships of taxel deformation with force, and proposed alterations of boundary conditions. The taxel implementation is presented in Section 2.3, along with a description of the experimental and signal processing methods used to characterize the sensor. Results from experimental characterizations of different single taxels in Section 2.4 reveal the effect of tube length and end cap modifications on the range and sensitivity of AcousTac. We demonstrate a system of AcousTac sensors in a 4-taxel array and a 3-taxel astrictive gripper in Section 2.5. Design guidelines, additional

---

[1]The flute may even date back 60,000 years [10].

observations, and limitations and future work are described in Section 2.6. Section 2.7 summarizes the impact of this work in the broader context.

2.2 Taxel design

In the following sections, we describe the theory behind the design parameters examined in this work. We present tradeoffs in generating acoustic resonance in structures that respond to variable force ranges and with different compliant boundary conditions.

Resonant frequency and tube length

In one dimensional (1D) theory, a tube that is open on one end and closed on the other has a fundamental resonant wavelength, λ, four times the tube length, L (Fig. 2.1A). Frequency, f, is related to wavelength, λ, by $\lambda = c/f$, where c is the the speed of sound. Resonant frequency, f_{oc}, of an open-closed tube is therefore

$$f_{oc} = \frac{c}{4L}. \tag{2.1}$$

For a tube open on both ends (Fig. 2.1B), the resonant wavelength is twice the tube length, such that the resulting frequency, f_{oo}, is

$$f_{oo} = \frac{c}{2L}. \tag{2.2}$$

For both the open-open and open-closed boundary condition, frequency is inversely proportional to length. The frequency will be higher for a smaller sensors with shorter tubes. We propose to fit experimental data to a modification of Eqn. 2.1 in this case, with the constants b_i such that

$$f = \frac{b_1}{b_2\,L} + b_3. \tag{2.3}$$

In the case of a tube with a soft end cap at one end, this boundary condition appears to lie between the open and closed idealized cases, as the soft material partially damps and reflects vibrations, still resulting in resonance. When external forces deform the soft end-cap (Fig. 2.1C), the length of the tube changes; the frequency also changes. Linear approximation of Eqn. 2.1 shows that the shorter the tube length L, the greater frequency change Δf for a change in length δ, where L is the unloaded length. As such, shorter tubes are more sensitive to end cap deformations. For a linear approximation of the open-closed tube, change in frequency relates to length as

$$\Delta f = -\frac{c}{4}\frac{\delta}{L^2}, \;\; \Delta f \propto \frac{\delta}{L^2} \tag{2.4}$$

The above 1D theory assumes a thin tube, $L >> D$, where D is the inner diameter of the tube. In practice, taxel tubes have a non-zero diameter and a particular inlet geometry
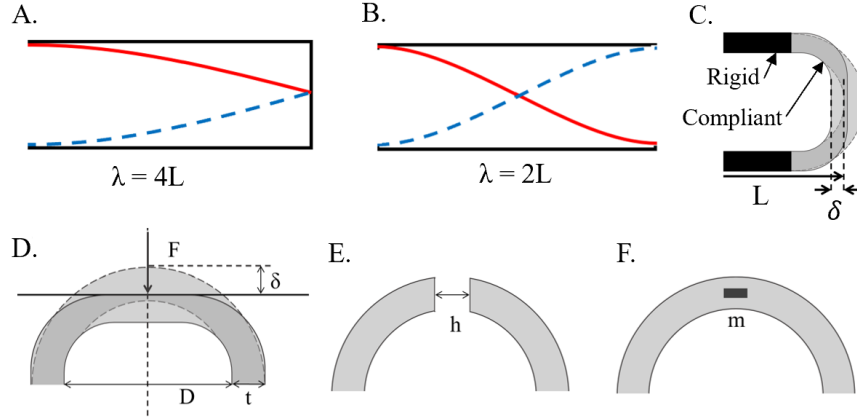
Figure 2.1: A. Open-closed boundary condition, where L is one-quarter of the wavelength λ. B. Open-open boundary condition. L is half wavelength. We imagine the boundary condition as open-damped, where the damped end is in between open and closed. C. Schematic denoting rigid tube length L and compliant cap deformation δ that changes the total length of the taxel. D. Schematic of hemispherical cap. A normal force F deforms the cap by distance δ. This deformation decreases the total length of the taxel and increases the resonant frequency. The inner diameter of the cap d is kept constant. We test varying wall thickness t and adding E. a hole with diameter h and F. mass m.

which makes the measured resonant frequency deviate from theory. Regardless, the 1D model serves as a useful design tool to predict first-order trends. Additional factors known to contribute to resonant frequency, are kept constant for this study. For example, as flow rate increases, higher harmonics dominate the resonance; this work assumes the fundamental frequency mode across all designs.

Force on compliant hemispherical shell

Deformations of the end-cap alter tube length and result from externally applied normal compressive forces. Frequency is therefore a measure of force. Designers can tune force sensing range and resolution by varying end-cap stiffness. Both material selection and geometry alter the force-deformation response. Generally, the stiffer the cap, the greater the force range and the lower the resolution and sensitivity. From the elastic contact theory model for small deformations of a rubber hemisphere [119], force F relates to displacement δ as

$$F \propto \delta^{3/2}. \tag{2.5}$$

In this work, the end-cap is a hemispherical shell with a wall thickness t and inner diameter D that experiences large deformations (Fig. 2.1D). We therefore propose an empirically fit approximation of Eqn. 2.5 with constants β_i for each cap design

$$F = \beta_1 \delta^{\beta_2} + \beta_3. \tag{2.6}$$

Altering end-cap boundary conditions

Due to the physical properties of the soft compliant end-cap, the unloaded cap behaves somewhere in between an open and closed boundary condition, and we refer to this as *damped*. In this damped boundary condition, the cap is a flexible, oscillating surface, resulting in a frequency higher than in the closed condition and lower than in the open condition. When a rigid object contacts the cap, the boundary condition undergoes a transition from damped to closed, lowering the resonant frequency.

This will occur even without gross deformations or substantial changes in tube length L. However, this transition between different boundary conditions occurs across a range of light contact forces greater than zero, until there is no relative vibration between the object and cap surface. For forces higher than this boundary condition transition phase, gross deformations reduce length and increase frequency. We therefore expect a nonmonotonic sensor signal, with a minimum value under light contact forces.

In this work, we propose and investigate two design features to mitigate or remove this resonance property, and produce reliable measures of force. Specifically, we explore the introduction of a hole or mass at the tip of the end-cap.

Hole

As in Fig. 2.1E, we add a hole of diameter h to the center of the compliant cap. Adding a hole to the cap makes an unloaded cap behave more similarly to an open boundary. When an object occludes the hole and loads the cap, the end then transitions to the closed boundary condition. For a given tube length, the resonant frequency of the open-open boundary condition is twice the frequency of the open-closed boundary condition. Higher flow excites higher resonant frequency, and we generally expect increasing flow rate to excite higher modes. Therefore, selecting a flow rate that actuates closed tube resonance but not the open tube's creates a change in amplitude at the transition between no contact and contact. By coupling both amplitude and frequency measurements, contact force is uniquely determined, overcoming the nonmonotonic force-frequency relationship in the transition region. In addition to flow, some geometries, including the edge-orifice shape and inner tube diameter, are more conducive to certain resonance modes than others.

Mass

As in Fig. 2.1F, we add a mass m to the cap to bring it towards the closed boundary condition, even without contact. The mass increases the inertia of the compliant surface and further dampens the pressure oscillations. Sufficient mass removes the nonmonotonic behavior of the frequency, such that the boundary condition does not change upon contact.

2.3 Methods

Taxel implementation and test parameters

A rigid tube and compliant end-cap compose each taxel. We individually fabricate these components and assemble them together into a single taxel, which is then rigidly mounted to an acrylic plate for testing. The rigid tube is a specified length L (Fig. 2.2A), additive manufactured with PLA (Makergear M3-1D 3D Printer, nozzle diameter 0.35 mm). The length of the resonant tube varies between 41 and 65 mm, in increments of 6 mm. These 6 mm intervals ensure the resonant frequencies of the different taxels do not overlap. The inner diameter is 6 mm. The smallest cross section is 1.4 mm, located immediately before the edge-orifice, the angled cutout of the tube wall. The inlet and edge-orifice geometry are consistent across all taxels.

The end-cap is the soft element in the taxel. We fabricate and test a range of cap thicknesses t, hole diameters h, and added mass m (Fig. 2.2B) to assess the effect of these parameters. We cast silicone (Smooth-On Dragon Skin 30) in a two-part mold to make the caps. All caps have the same 7 mm inner diameter hemisphere, regardless of thickness, and a 5 mm long cylindrical cavity, also 7 mm in diameter, that stretches over the open end of the rigid tube.

To assess taxel stiffness and force range, the wall thickness t of the caps ranges from 1 to 5 mm (t1 through t5), at 1 mm increments. To test the effect of hole size, we compare caps with 3 mm wall thickness, across 0, 1, 3 and 5 mm hole sizes. A complete set of thicknesses (t1 through t5) are tested for both without (h0) and with a 3 mm hole (h3) to test coupling between these parameters. The caps with holes are cast with dowel pins of specified diameter in the negative mold. We add cylindrical magnets to the compliant caps to assess the addition of mass. Each magnet has a mass of 50 mg, a diameter of 2 mm, and a height of just less than 1mm. We test caps of 1, 3, and 5 mm wall thickness, and vary the number of magnets between 1 and 4 (m1 through m4). This results in an added mass of up to 200 mg. For the 1 mm thickness cap, we adhere 1 magnet to the outer surface with glue. For 3 mm and 5 mm thickness, the first magnet is embedded into the cap during the casting process. We increase mass by adding more magnets to the inner surface of the cap, which utilizes their magnetic attraction to attach them.

In this study, we characterize all the different end-cap designs using one resonant tube length $L = 59$ mm. When comparing the different rigid tube lengths, we use a single end-cap design with 3 mm wall thickness, and no hole nor mass (t3h0).

Taxel characterization test setup

We characterize each taxel individually using the experimental setup shown in Fig. 2.2C. The taxel is fixed to the tabletop. Wall compressed air flows through flexible 8.3 mm (3/8") tubing and a flow meter (analog 1-10 LPM) before entering the resonant tube, which is kept between 4 to 5 L/min. A robot arm (UR-10, Universal Robots) and 6DOF wrist force/torque
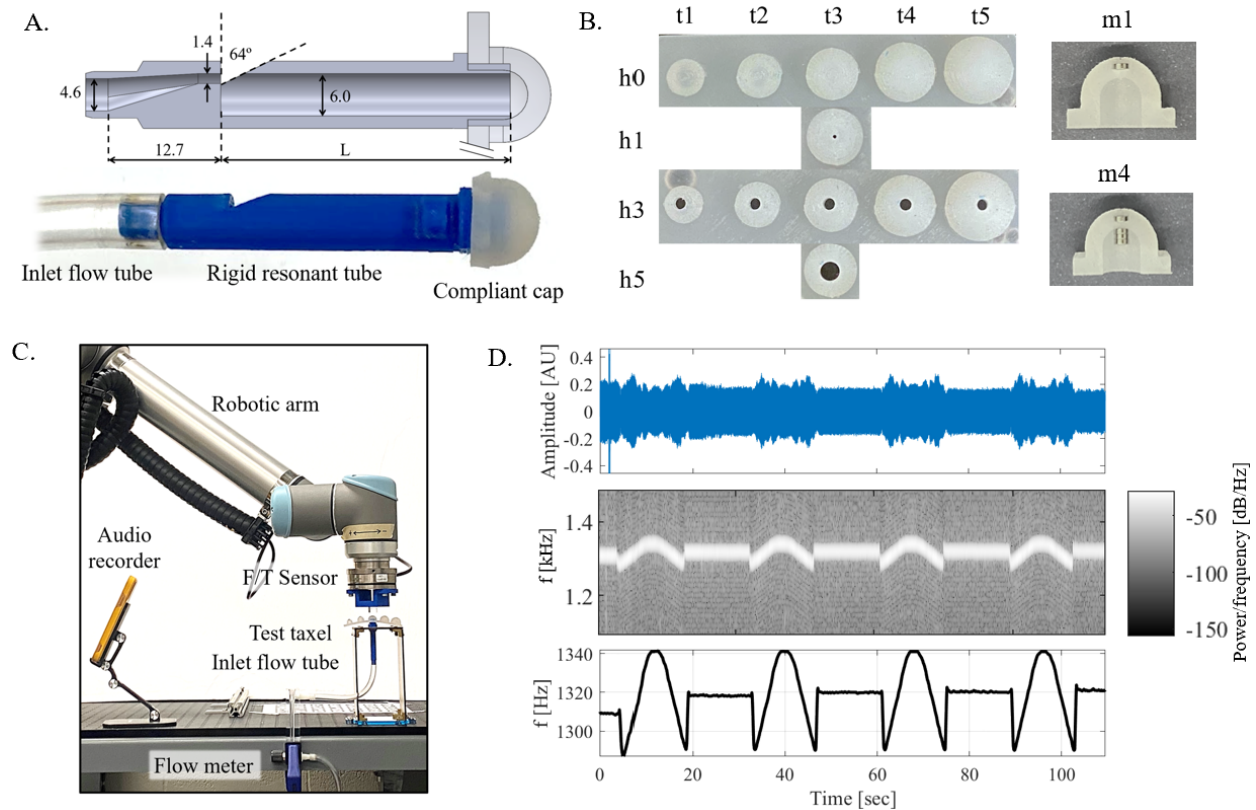
Figure 2.2: A. Taxel schematic L = 41 + 6n [mm]. All dimensions in mm, except for edge-orifice angle in degrees. Photo of fabricated taxel, analogous to above. Flow enters the resonant tube from the left. The hemisphere on the right is compliant and adhered to the rigid structure. B. Photo of the caps tested. We varied wall thickness t and hole diameter h. The number indicates the wall thickness or hole diameter in millimeters. C. Photo of experimental setup for taxel characterization. D. Example data from processing the raw audio signal to spectrogram for frequency, then picking out the maximum amplitude frequency.

sensor (Axia80, ATI) cyclically palpate the taxel, moving at 0.5 mm/s until at least 5 N of normal force. We increase the tested force range with cap thickness. Robot Operating System (ROS) software records force and position at 2.0 kHz and 3.3 kHz, respectively. A smartphone (iPhone 11) located approximately 0.5 m away records sound at a sampling rate of 44.1 kHz. Ambient lab noise is approximately 65 dB, less than the approximately 90 dB sound level when a taxel is active.

Audio processing

Fig. 2.2D shows an example of the audio signal and processing outcome for four palpations of the t3h0 end-cap. We perform data processing using the pipeline detailed in [64]. We extract the resonant frequency from the raw amplitude data at 25 Hz, using the built-in MATLAB functions *spectrogram()* and *tfridge()* and binning frequency in 2.5 Hz intervals. For caps with holes, we are also interested in the amplitude of the audio signal. We generate an envelope of the raw audio by finding the max absolute amplitude value for every 22.7 ms (1000 data points) then taking a smooth average for every 113 ms (5000 data points). The amplitude is then downsampled to 25 Hz to match the sampling rate of extracted frequency.

Characterization tests without a hole h0t1-h0t5 or with a mass m1-m4 all consist of at least 3 palpation cycles performed within 80 sec each. In the amplitude thresholding tests when a hole is present, h3t1-h3t5 and h1t3-h5t3, we only report points above the set threshold, which is approximately 12 sec of data over at least 2 palpation cycles. The specific amplitude thresholds in each hole case are individually selected as the minimum value to avoid a nonmonotonic relationship between force and frequency in that design's data set.

In later demonstrations with systems of 3 and 4 taxels emitting sound simultaneously, we assume that the achievable frequency range of each taxel does not overlap with any other. This is achieved by assigning a unique tube length to each taxel. We process data within the expected frequency range for each taxel separately.

2.4   Results: Taxel characterization

Tube length, L

In Fig. 2.3A, we plot the measured frequencies for the four rigid tube lengths from two normal force loads: 5 N and 10 N. We also show the 1D theory for an open-closed cavity from Eqn. 2.1. The measured frequency is consistent with the theory, in which longer tubes exhibit lower resonant frequency. Table 2.1 presents fitting constants from Eqn. 2.3. The end-cap geometry is a negligible constant length offset and is not included in our calculations.

Table 2.1: Fitting constants for Eqn. 2.3 plotted in Fig. 2.3A.

Fit constants	f_{oc}	5N	10N
b_1	340	290	280
b_2	4	4.6	4.8
b_3	0	260	290

Fig. 2.3B shows the full characterization curves for frequency as a function of force, with loads ranging from zero to greater than 10 N. By design, the frequency ranges do not
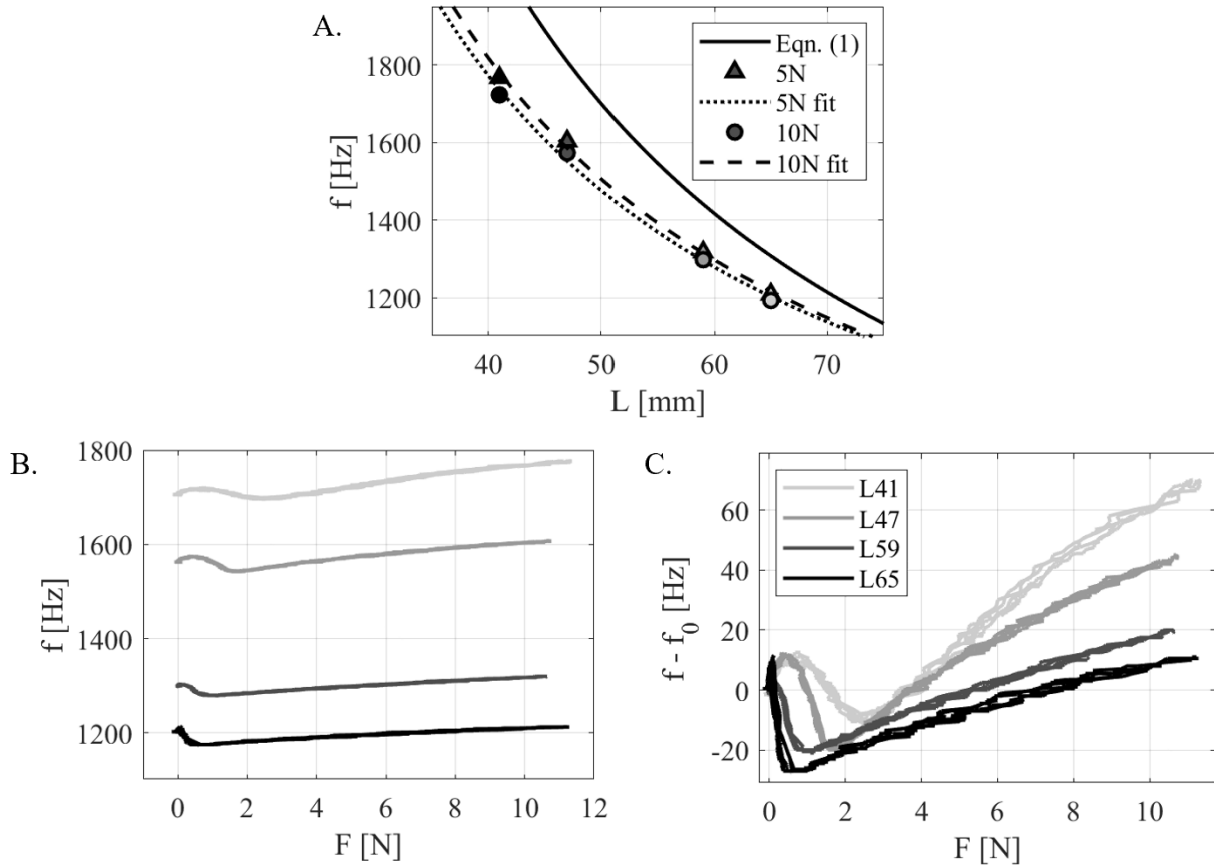
Figure 2.3: Calibration curves for taxels with varying tube length L with cap t3h0. A. Tube length and frequency f. The 1D theoretical model (Eqn. 2.1) is shown in a solid black line. Experimental data for resonant frequency loaded at $5\,N$ (triangle) and $10\,N$ (circle). This data is fitted with Eqn. 2.3, shown with the dotted black lines. B. Resonant frequency with force F for all four tested tube lengths. C. Net frequency change from unloaded condition, $f - f_0$, plotted with force.

overlap each other to streamline later signal processing when multiple taxels emit sound at the same time. In Fig. 2.3C, we plot the same data but now as the net change in frequency; measured frequency f is subtracted by unloaded frequency f_0 to inspect the calibration curve shape. All four taxels demonstrate a nonmonotonic frequency relationship, with both local maxima and minima observed at forces less than $3\,N$. As force increases from initial contact, the frequency increases, then decreases, then increases again. This behavior is likely due to the boundary condition changing from damped to closed as the force increases. After the boundary condition transitions, at forces greater than $3\,N$, the shorter length taxels with higher unloaded frequency have steeper slopes. This is consistent with Eqn. 2.4. We do not observe any hysteresis in the signal for these taxel lengths.

Cap wall thickness, t

We plot cap deformation versus force in Fig. 2.4A for caps with no hole (t1h0-t5h0). In the tested displacements, thicker caps provide a more linear force displacement curve, which is steeper than thinner caps at lower displacements. The softer, thinner caps have a linear region at low forces, then start to saturate. Table 2.2 shows the fitting constants for these caps using Eqn. 2.6.

Table 2.2: Fitting constants for Eqn. 2.6 for the data plotted in Fig. 2.4A.

Thickness, t [mm]	F_{max} [N]	β_1	β_2
1	2	0.94	1.36
2	6	1.56	1.77
3	11	2.66	1.64
4	15	2.65	1.68
5	15	3.52	1.50

Fig. 2.4B shows how the amplitude of sound produced by the taxel changes with deformation. A negative value of δ denotes the distance between contact surface and top of the cap, e.g., a -2 mm deformation means they are separated by 2 mm. Prior to contact, thinner caps exhibit lower audio amplitudes and are closer to the open boundary condition than thicker caps. However all cap thicknesses demonstrate a downward deviation in audio amplitude centered between 0 and 2 mm of contact. In Fig. 2.4C, the resonant frequency f is plotted as a function of force F. All the caps produce nonmonotonic boundary condition transitions, while the thinner caps show greater frequency fluctuations during the boundary condition change. The thinnest cap signal saturates at around 3 N of load, where the cap is compressed against the rigid resonant tube and can deform no more. The force-frequency slopes are consistent with cap stiffness trends.

Cap design feature: Hole, h

Fig. 2.4D shows the audio amplitude with varying cap wall thickness in designs with a 3 mm diameter hole (t1h3-t5-h3). As compared with the cases without a hole, all taxels have a lower amplitude when there is no contact. Upon contact, varied deviations in the amplitude arise. However, all signals increase and remain above the unloaded amplitude with enough deflection. This amplitude cross-over threshold occurs for the smallest deflection for the thinnest cap, which also has the lowest amplitude prior to initial contact. In Fig. 2.4E, the force-frequency relationship is plotted while employing the amplitude crossover threshold to produce monotonic results. The shape of the force sensing curves is similar to those found in Fig. 2.4C, except for the omission of data at the lowest force levels. Table 2.3 reports
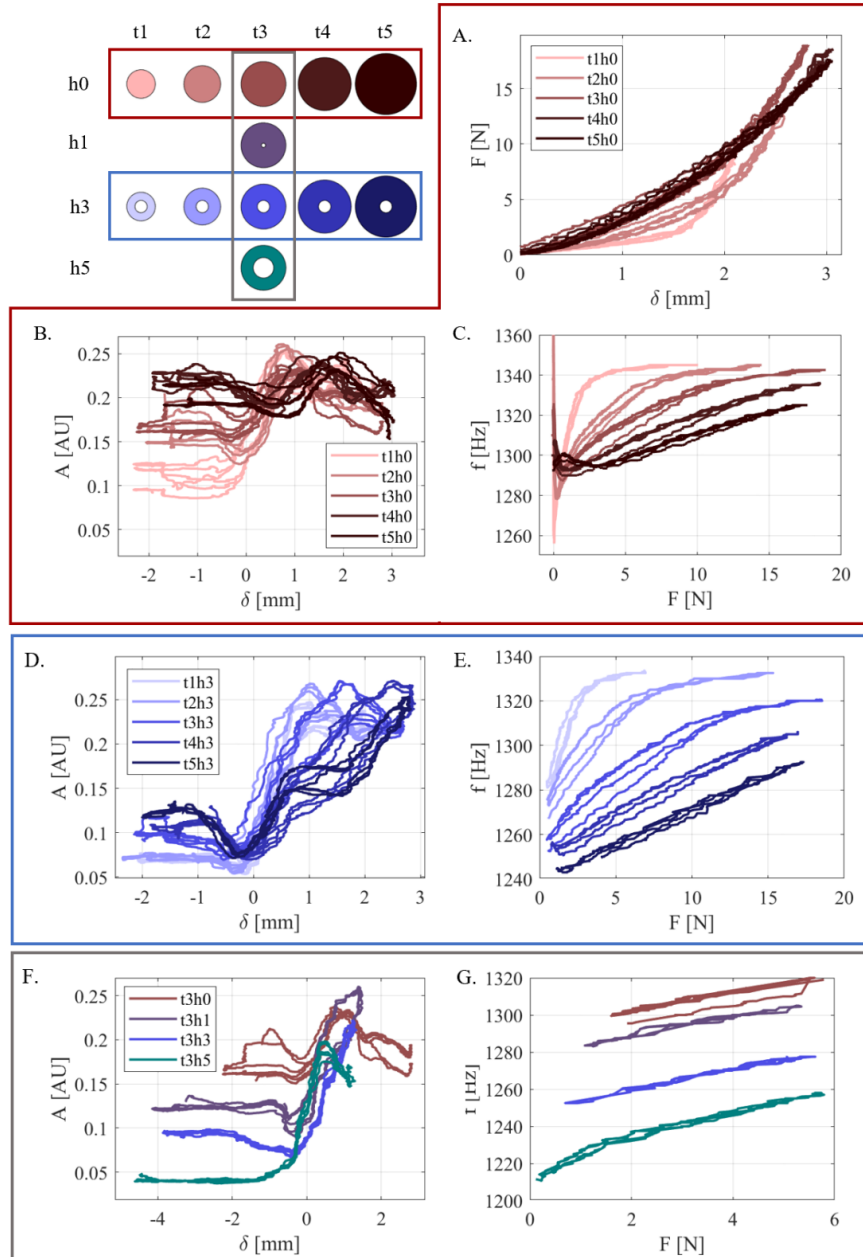
Figure 2.4: Characterization of cap wall thickness t and hole diameter h, and their relationships with force F, displacement δ, audio amplitude A, and frequency f. A color coded schematic is used as a legend of tested cap parameters.

the each force taxel's resulting approximate linear ranges and sensitivities. The lower bound of force range is from the minimum detectable force after amplitude thresholding. Visual inspection dictates the upper bound as where the signal begins to saturate.

Table 2.3: Amplitude threshold value, force range and sensitivity for caps with 3mm hole, plotted in Fig. 2.4E.

t [mm]	Threshold [AU]	F_{min} [N]	F_{max} [N]	Sensitivity [Hz/N]
1	0.17	0.5	2.6	19
2	0.15	0.6	6.1	8.8
3	0.12	0.5	10.	5.1
4	0.13	1.3	15	3.6
5	0.15	1.5	15	3.2

In Fig. 2.4F, amplitude is plotted across caps with the same thickness, 3 mm, but with varying hole size (t3h0-t3h5). Larger holed caps exhibit lower sound amplitude prior to contact, which is expected as they are more physically similar to an open tube. As a result, the larger hole allows for a lower amplitude threshold. As seen in the monotonic force-frequency curves in Fig. 2.4G and tabulated values in Table 2.4, caps with larger holes capture smaller forces in their sensing range when using amplitude thresholds. With the exception of the t3h5 calibration curve, for which the hole is a substantial size compared with the cap and lower forces are measured, these sensitivities are within 8% of each other.

Table 2.4: Amplitude threshold value, force range and sensitivity for caps with 3mm wall thickness, plotted in Fig. 2.4G.

h [mm]	Threshold [AU]	F_{min} [N]	Sensitivity [Hz/N]
0	0.22	1.6	5.1
1	0.19	1.1	4.9
3	0.14	0.9	5.3
5	0.06	0.2	7.9

Cap design feature: Mass, m

Fig. 2.5 depicts how magnets attached to the tip of the cap alter force-frequency relationships in the transition region, where A, B, and C show the results for the 1, 3, and 5 mm cap thicknesses, respectively. The added mass varies from 50 g (m1) to 200 g (m4), with darker lines indicating higher mass. Overall, increasing mass mitigates the frequency fluctuations from the boundary condition transition. We observe nonmonotonic behavior in the tested force range with 50 mg added mass in all the three cap thicknesses. This boundary condition effect resolves with 200 mg for 1 mm thickness and 3 mm thicknesses, and 50 g for 5 mm thickness caps. As expected, the thinner caps require more mass to remove the boundary
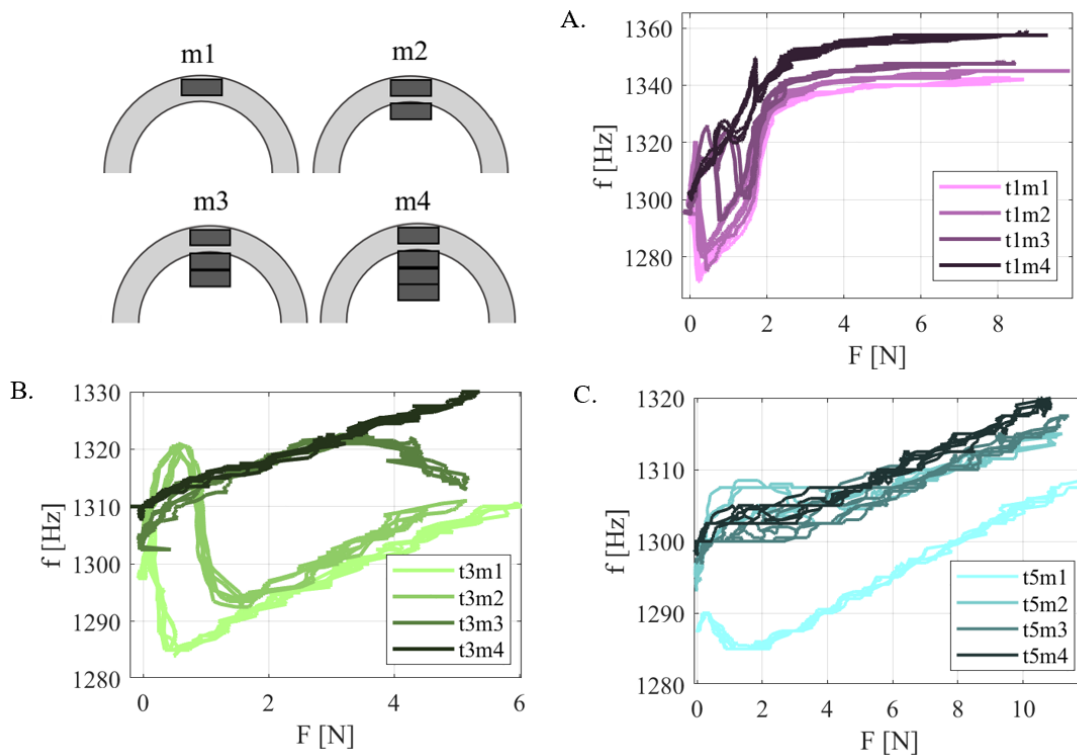
Figure 2.5: Characterization of added mass m, as shown in the schematic legend of stacked magnets used as mass on cap. Frequency f versus force F for wall thickness for A. 1 mm, B. 3 mm, and C. 5 mm caps. Darker lines indicates higher masses.

condition transition. For both the 1 and 3 mm thicknesses, intermediate levels of mass shifts the minima frequency locations to higher force levels. The mechanism that causes the t3m3 force-frequency curve to have this upward then downward sloping shape is unclear; the decrease is out of the typical force range for a boundary condition transition and perhaps due to the mechanics of the added mass on the cap. The magnets have nonzero volume and are rigid, which may account for the hysteretic effect observed within some transition regions, e.g., in t1m3.

2.5 AcousTac demonstrations

Test systems

Two multi-taxel systems are shown in Fig. 2.6: (A) a tactile array and (B) an astrictive gripper.

First, we combine four taxels of different lengths for an indicied, force and contact sen-
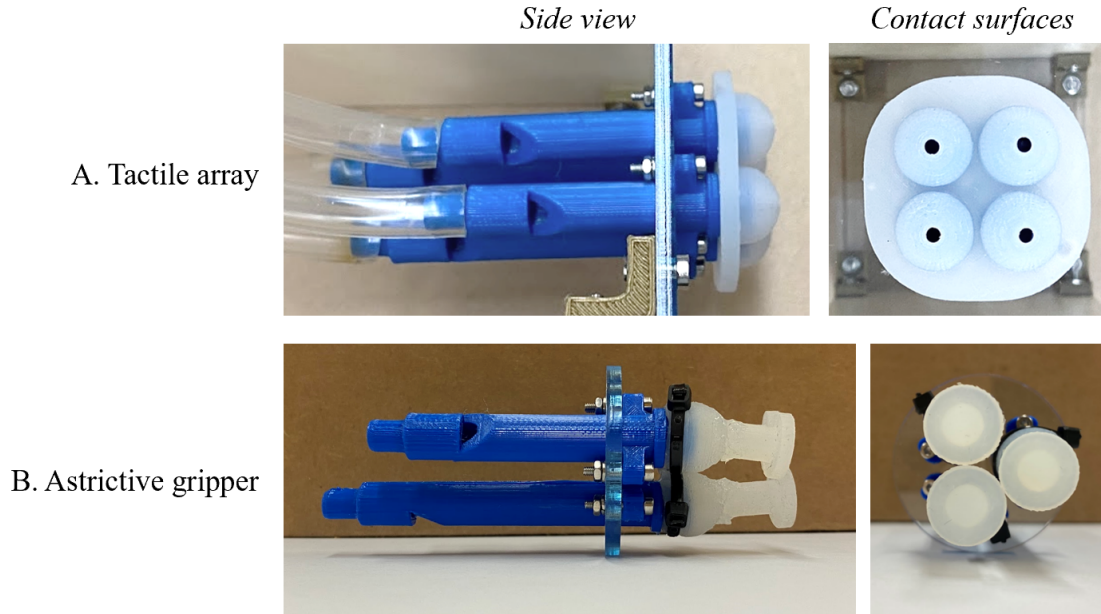
Figure 2.6: A. Tactile array with four taxels of length L = 41, 47, 59, 65 mm. Caps have 3 mm wall thickness and a 3 mm hole diameter (t3h3). B. Astrictive gripper with three taxels of length L = 41, 47, 59 mm. Caps have 2.5mm wall thickness and suction cups adhered to the tops.

sitive 2x2 array. The taxel lengths are consistent with those in Sec. 2.4: 41, 47, 59, and 65 mm. We position the four taxels in a grid pattern, spaced 15 mm apart center-to-center. The end-caps have a 3 mm wall thickness and 3 mm hole (t3h3). For the processing of the signal from the L59 taxel, we use the sensitivity value from Table 2.3 to translate frequency to force. For the three other taxel lengths, we scale the force by a ratio of L^2 according to Eqn. 2.4. All taxels receive air from the same source. As varying flow rate produces slight differences in each taxel's frequency, and can change as neighboring taxel holes get covered, the measured frequency at light contact is set as the unloaded frequency as an initialization calibration procedure.

Next, we integrate three taxels into a force sensitive astrictive gripper. Inspired by prior work [47, 53], we implement passive suction cups to grip onto objects. The taxels are evenly spaced 15.9 mm apart, with rigid tube lengths of 41, 47, and 59 mm. The caps have 2.5 mm wall thickness, and we adhere a suction cup to each cap using an air-cured silicone glue (Smooth-On Sil-Poxy). The suction cups are similarly cast from silicone (Smooth-On Dragon Skin 30) and are 13 mm in diameter and 2.5 mm thick. The suction cups sit on posts 7 mm in diameter and 11 mm tall. We affix the caps to the rigid tube and wet the suction surface with tap water to increase suction force. Because the introduction of suction cup structures to the caps alters the frequency response of this system, we report frequency and

not force.
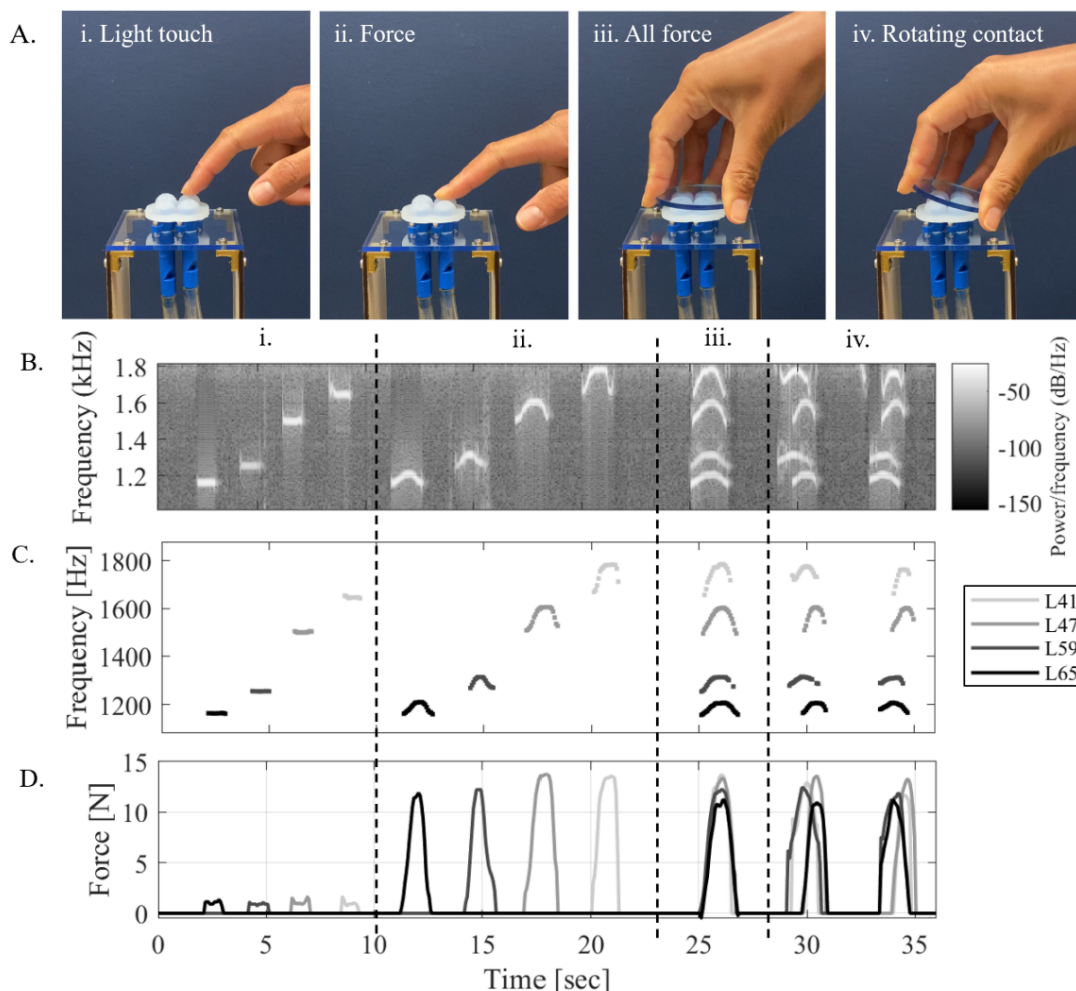
Figure 2.7: Robotic demonstration of tactile array with caps t3h3. We palpate taxels indi-
vidually, with a light touch (i) and then with a forceful touch (ii). We then use an acrylic
round to press all the taxels down simultaneously (iii). Then we use the same round and
roll/rotate across the taxels, across both directions (iv). A. Photos corresponding to the
sequences. B. Spectrogram. C. Signal processed with amplitude and frequency over time.
D. Normal force over time.

Tactile array interaction

Shown in Fig. 2.7A, we contact and palpate the caps individually with one finger and
together with a piece of acrylic over four different sequences. First (i), we make light contact
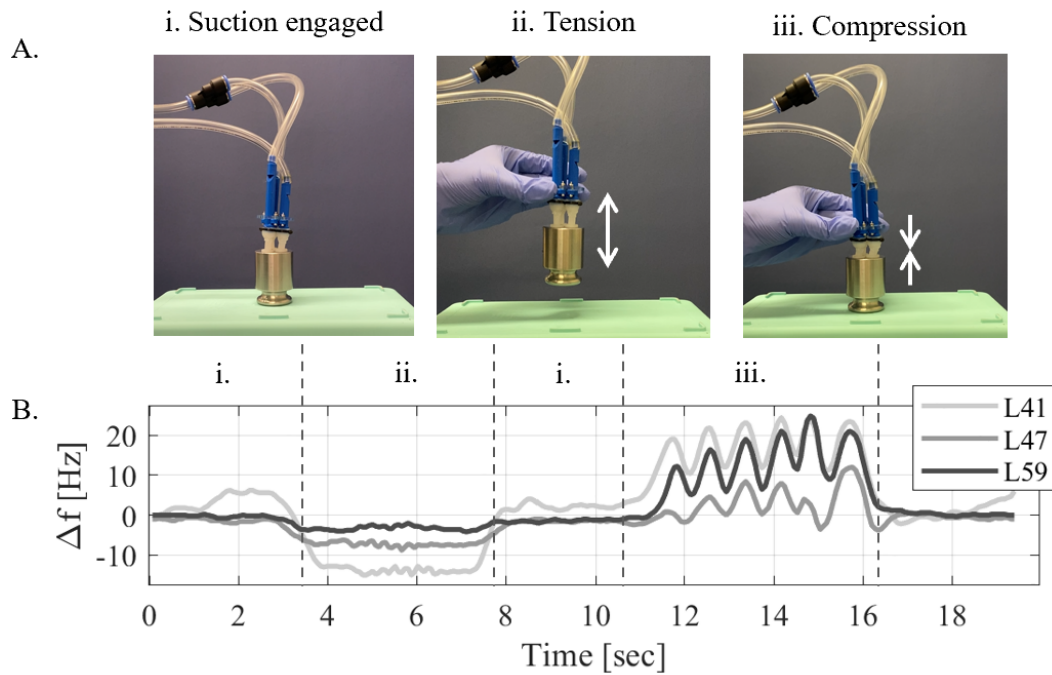
Figure 2.8: Demonstration of suction cup gripper with three AcousTac taxels tested on a 500 g weight. All three suction cups are engaged (i), and exhibiting some load due to air hose routing. Gripper is lifted along with the weight, and then hefted so the weight bounces up and down (ii). Weight is set back on the surface and compression forces are applied (iii). A. Photos from demonstration. B. Net frequency change of the three taxels over time.

with each taxel individually, started from L65 and ending with L41. In the same order, we push down on each taxel individually with greater force (ii). In the third sequence (iii), an acrylic plate is pushed down on all the taxels simultaneously. In the last sequence (iv), the same acrylic piece applies a rolling forceful contact across the array in two orientations rotated by 90 degrees, side to side and front to back. Fig. 2.7B shows the audiospectrogram in the relevant frequency range. We extract the peak frequencies from the spectrogram (Fig. 2.7C) and translate them to force (Fig. 2.7D). Signals are as expected. With rolling contact, we observe two taxels loaded prior to the other two, showing the different between the two rolling orientations. We use a linear mapping enabled by the addition of a hole and therefore monotonic force-frequency relationship. This tactile array demonstrates the practicality of holes in the caps, exhibiting low amplitude of sound when not in contact, and resonance when loaded.

Astrictive gripping

Shown in Fig. 2.8A, we manipulate a 500 g weight, imparting tension and compression via suction cup gripping. Fig. 2.8B shows the net frequency of the three taxels. In the demonstration, the suction cups adhere to the smooth, flat surface of the weight (i). The gripper lifts the weight and hefts repeatedly with weight still attached (ii), varying the tension loading. In part (iii), we compress the suction cups against the weight. The resonant frequency signals show expected trends, in which the sensor captures the oscillating tension forces at approximately 4 Hz in (ii) and the larger compression force at about 1 Hz in (iii).

2.6   Discussion

The experimental results show the substantial effects of tube and cap geometry on the sound signals generated by AcousTac. Parameters including tube length and cap wall thickness affect frequency and force measurements as expected from simple first-principle design models. For example, as the tube length decreases, a given deformation results in a higher frequency output range. So, shorter tubes have higher sensitivities and also higher total frequencies. We leverage this length-frequency relationship in order to read multiple force signals simultaneously by assigning different tube lengths to different taxels in system demonstrations. Designers can further tune the cap wall thickness or material stiffness for a desired force sensing range. The fabrication of these taxels is simple, requiring only a 3D printer and silicone casting equipment. In part, the simplicity of this system is because there is no need for the integration of precise or sensitive electronics into the skin.

We observe a change in boundary conditions when contact occurs with the soft taxel cap. The compliant material produces a boundary condition that lies in between the open and closed cases. We posit that this damping results in the nonmonotonic force-frequency relationship that occurs upon initial touch during experiments. In order to tackle this issue, the addition of a hole or mass at the tip of the cap enables monotonic force readings, not otherwise achieved. When using holes, rather than mass, the sensor is generally quieter when no contact is being made, which is advantageous if operating near humans who may not want to hear the sensors at all times. The larger the hole, the quieter the sensor when not in contact. The presence of the hole also enables pre-touch and close proximity sensing; prior to contact, at distances of approximately 1 mm, a unique set of amplitude and resonant frequency signals are generated. At the same time, adding mass is a useful solution if a hole is not an appropriate option, for example when handling objects in wet or dirty environments where matter would enter the hole. In addition, the taxels with holes only produce reliable sounds when the hole becomes sealed by contact, which may not always occur.

Throughout this work, we use a common smartphone microphone to measure signals, demonstrating the accessibility and non-specialized requirements to implement AcousTac. In the current implementation, we implement audio processing parameters that dictate the temporal and force resolution. While this is not a physical limitation of the taxel sound

emission, sound collection hardware and processing speeds will influence overall system performance and the ability to detect fast transient loads. We operated experimental trials in a normal laboratory environment. In environments with loud or complex ambient noise, more sophisticated processing methods may be needed.

Limitations and future work

Spatial resolution is not the focus of this current work and could be improved in future work. Taxels need to be spaced far enough apart such that a deformed cap does not interfere with the neighboring taxel caps. Therefore, as taxel diameters get smaller, they can be packed more closely. As taxels reduce in size, output frequency, air supply, fabrication precision, and microphone requirements may need to change. Another issue could arise where the surrounding taxels interfere with the airflow near the edge-orifice. If the edge-orifice area of the tube is obstructed, resonance is inhibited, though we do not observe any issues for taxels spaced 15 mm apart. For sensors at substantially different length scales, a resonance generating geometry other than the current edge-orifice may be more appropriate from a resonance, packing, and physical implementation standpoint. With the addition of more taxels, future work should also investigate the limit on how many simultaneous frequencies can be produced within unique frequency ranges.

Throughout this work, we assume superposition holds for sounds signals from systems of multiple taxels. This seems to be true for the current design, where each taxel operates the same independently of the other taxels. However, with closely overlapping frequency bands, we observe heterodyning and difficulty processing the signals as a result. We also observe a dependence on microphone location due to constructive and destructive signal interference. Each taxel is separated by rigid materials in this study. When resonating soft structures are physically coupled together, their resonant frequencies can interact in complex and nonlinear ways [66], a topic to further investigate in fully-soft resonating structures.

We characterized AcousTac under normal loading conditions, yet oblique loading occurs in the real robot manipulation. As a preliminary test, we sheared caps with and without a hole under 5N normal force, with up to 2N lateral force. We did not find the sliding and shear forces to affect the normal force measurements. By modifying the cap geometry, AcousTac structures could potentially be specialized for other particular types of loading and deformation measurements in future work.

AcousTac uses the ambient atmosphere to transmit information. The atmosphere must be gaseous, as this resonance generation utilizes the compressible nature of the ambient air. The atmosphere also must be dense enough such that the sound propagates, i.e. not the vacuum of space. Extreme changes in temperature, density, and humidity would require additional calibration steps as they alter resonance and sound propagation [71]. As an open fluid system, the robot also needs to be able to provide a continuous flow of air when activating the sensors. Pneumatic systems for locomotion in untethered robots [27] and robots in extreme environments [68] could potentially power AcousTac for sensing on mobile robots. One relatively untapped benefit of active acoustic tactile sensing is that sound can be

measured across large distances, even without physical contact with the resonating system. Thus, if loud enough, information about robot contact state is detected by any microphone within audible range.

2.7 Conclusion

In this work, we present AcousTac, a pneumatic-driven electronic-free tactile sensor that emits deformation and force information through active acoustic resonance. AcousTac is capable of producing monotonic force measurements without hysteresis, captured by a remote microphone. Because there are no electronics located at the skin, the taxels are simple and cheap to fabricate and resilient to loading that might otherwise fatigue or break electrical wires or connectors. By characterizing a range of sensor parameters and comparing to theory, this work serves to guide future implementations of AcousTac across a range of force scales and applications. For example, it is an attractive option where electronics cannot function, e.g., in an Magnetic Resonance Imaging (MRI) machine or in harsh environmental conditions, e.g., when handling volatiles. AcousTac could also potentially be utilized for wireless communication between different agents, where any agent with a microphone can sense the state of another. Ultimately, sound holds great potential to enable soft robots to communicate information across distances without wires; with soft structures generating resonant sound, emitted frequencies sensitive to robot state can be harnessed with audio transducers that are already integrated in robotic systems.

Chapter 3

Sensing on a soft actuator

Soft robots capable of dexterous manipulation can enable the exploration of extreme environments. Equipping these robots with tactile sensing is a challenge, as sensors must be flexible, stretchable, and robust to environmental conditions. We present a tactile sensor design with a pneumatically driven acoustic resonator, without electronics near the end-effector. For applications to soft grippers, we measure the resonant frequency of a soft tube undergoing stretching and bending. A small hole along the resonant tube enables contact sensing and pretouch up to 2 mm away. We also measure resonant frequency for a rigid uni-axial force sensing probe. Grasping tasks utilize three sensing modalities of a soft gripper; finger pose, fingertip contact, and force in the palm all provide feedback for dexterous manipulation. We discuss and address in future work the effects of atmosphere and air flow rate on resonant frequency as well as limitations in signal processing of this sensor design.

3.1   Introduction

Soft robotic hands and grippers enable gently adaptive interactions through underactuation and compliant and deformable materials. These designs are already demonstrated in a wide range of potential applications – for example, soft hands can be particularly well suited to field missions when the end-effector must be capable, gentle and physically resilient [109, 126]. Equipping soft robots with a "sense of touch" is an active development area that enables new adaptive control methods for manipulation tasks [22].

While soft pneumatic robots have demonstrated survivability and operation in extreme conditions like snow, fire, and large external loads [121], challenges remain regarding the integration of electronics and sensors into articulated soft structures, discussed in [81]. New fabrication methods continue to emerge in order to integrate electronic sensors with soft actuators. Recent soft sensing works include additive manufacturing with conductive filaments [124] and with embedded electronic sensors [105], and screen printing with piezoresistive materials [38, 57]. Other sensing modalities include a camera on the end of a growing vine robot for steering and locomotion [42]. A microphone embedded in a soft finger detects where and
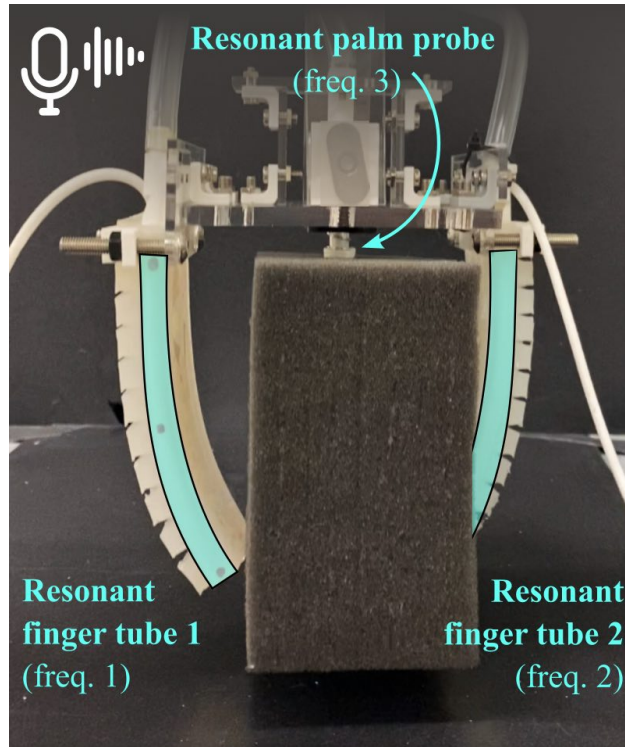
Figure 3.1: A robotic gripper with soft fingers employs embedded pneumatic resonance-based acoustic tactile sensors. Each finger can detect pose and contact, while a probe in the palm measures force. The single remotely located microphone simultaneously monitors the emitted resonant frequency of each sensor. The gripper has no integrated electronic components.

what the finger is tapping [135]. A challenge is to reduce the effects that large, repetitive strains, and resulting fatigue, have on the function of sensitive electronics over extended use.

Additionally, electronics may be unsuitable for some conditions, such as in easily combustible atmospheres (gas tanks, mine shafts) or in sensitive magnetic fields (MRI). An example of a recent trend towards soft robots that operate without electronics altogether includes pneumatic computation for gait control during locomotion [68, 27].

We present a new flexible tactile sensing modality, without electronics near the end-effector. Inspired by woodwind instruments, we integrate resonant tubes in the soft fingers and palm of a gripper. Emitted acoustic frequencies, dependent on the geometry of these resonant tubes, provide information about pose and contact of the fingers and force at the palm, and are monitored by a remotely located microphone (Fig. 3.1). We note that people perceive acoustic emissions during dexterous manipulation, with studies showing that sound plays a role during haptic exploratory procedures [43]. In application, we envision a robot topology akin to the human ear, where the sounds emitted at a distal end-effector are

perceived with a microphone on the body of a robot, proximal to the manipulator. To the authors' knowledge, this is the first presentation of tactile sensing where the signal travels through the atmosphere, and the end-effector has no electronics nor requires vision.

Overview

Section 3.2 provides the relevant theoretical background on acoustic resonance, with the measurand of frequency modulating as a function of cavity geometry. Section 3.3 describes the resonant tube geometries, acoustic measurements and processing methods employed throughout the experiments. We then present the implementation and calibration of specific resonant sensors analogous to the sub-components of a robotic gripper: (1) proprioceptive and contact sensors integrated into a soft finger in Section 3.4 and (2) a force probe for the palm in Section 3.5. In Section 3.6, we demonstrate the integrated gripper, as in Fig. 3.1, showing how multiple sensor readings can be detected simultaneously with a single off-board microphone. Future directions for this tactile technology are discussed in Section 3.7. Emphasized in Section 3.8, such acoustic sensing holds great potential for soft, electronics-free end-effectors.

3.2 Acoustic theory

Instabilities of airflow across objects can generate pressure waves that emanate through the atmosphere. Under certain conditions, these pressure waves amplify in a feedback mechanism known as resonance [16]. We purposefully design a pneumatic resonator (Fig. 3.2). A constant pressure drop drives airflow through a narrow inlet, across an edge and into a tube. Airflow oscillates above and below the end, emanating as pressure waves into the ambient atmosphere. The frequency of oscillation is dependent on the geometry of the resonant tube. We focus on tube length for this sensor design, where stretch and compression change tube length and resonant frequency. Adding a small hole along the side of the tube affects resonant frequency as well. Resonant frequency is a function of additional parameters such as edge-orifice shape (*fipple*), atmosphere and flow rate, which are kept constant throughout this study.

Resonance of a closed tube with varying length

The resonant frequency can be approximated from the geometry of the tube. In the 1D wave propagation model of a closed-closed tube, the fundamental wavelength or first harmonic is twice the tube length. Higher harmonics are multiples of this fundamental harmonic. Resonant frequency f_r for a closed tube is

$$f_r = \frac{nc}{2L} \tag{3.1}$$
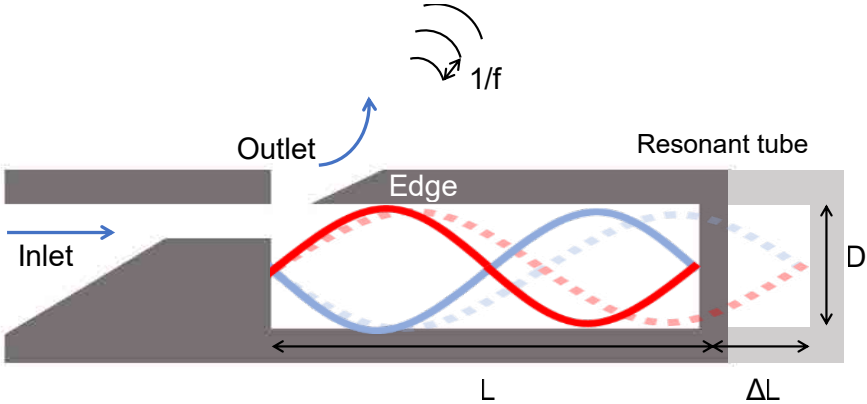
Figure 3.2: Cross-sectional schematic of pneumatic resonant structure. Air flows in from the left and is constricted through a slit. Air flows out above the edge and into the tube, traveling the length of the tube and back. These oscillations create pressure waves, with the oscillating frequency f governed by the cavity length L. The waveform (blue/red curve) represents the second resonant mode (closed-closed) of the given cavity. Increasing the resonant cavity length ΔL decreases the emitted frequency.
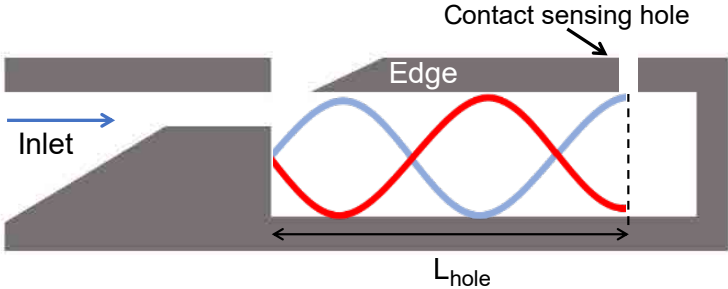
Figure 3.3: Cross-sectional schematic of pneumatic resonant structure for contact sensing. An unobstructed contact sensing hole changes its local boundary condition to an antinode. Contact at the sensing hole reverts the resonance back to closed-closed regime of a non-perforated tube.

for harmonic integer $n = 1, 2, 3...$, speed of sound c, tube length L. Many geometric parameters of the resonant structure alter the emitted frequency, e.g., fipple shape. We focus on tube length as an analog to finger pose and force sensing.

Resonance with small lateral opening

In addition to physically changing the resonant tube length, a lateral opening along the tube effectively changes the boundary condition, and thus the resonant modes and frequency. With a lateral hole as shown in Fig. 3.3, the hole location is likely in an antinode condition. Then the resonant mode n may be different from the mode without the hole, depending on the hole location. Computing actual f_r would require computational fluid dynamics solvers, which is beyond the scope of this chapter.

   We propose to detect contact of an object over the hole by measuring the difference in resonant frequency f_r before and after the contact. It is also difficult to model the resonant mode of partially closed or air-leaking hole; we present an experimental result from gradual hole closing in Sec. 3.4.

3.3   Experimental methods & acoustic processing

Throughout this study we utilize a flow divider geometry upstream of the resonant tube. This fipple has a maximum stream-wise gap length of 3.6 mm and the edge angle is 28.5°, as in Fig. 3.4 and helps create the oscillating pressure waves we detect as sound. The inlet is connected to a compressed air line by flexible hosing with a 8.3 mm (3/8") outer diameter, and the hose is over 4 m long with air pressure less than 34 kPa (5 psi). The resonant chambers, those described in Sections 3.4 and 3.5, are then attached to the other end with a press fit. One fipple is dedicated to each sensor, therefore the integrated gripper in Sec. 3.6 utilizes multiple fipples. We use a robot arm (UR-10, Universal Robots) and 6DOF wrist force/torque sensor (Axia80, ATI) for the following experiments. The experimental setup for pose estimation and gripper demo is depicted in Fig. 3.7. Sound is recorded with a smartphone (iPhone 11) at a sampling rate of 44.1 kHz for experiments in Sec. 3.4 and Sec. 3.6, and with an omnidirectional microphone at 48 kHz for experiments in Sec. 3.5. The microphones are located approximately one meter from the resonators.

   We analyze the audio recording to obtain the power spectral density (PSD) and compute resonant frequency (f_r). The spectrogram in Fig. 3.5A shows an example of the different resonant modes of acoustic emission from the fipple and resonant tube (90 mm in length, and 7.1 mm in diameter). We compute the f_r by choosing the frequency with the highest PSD as shown in Fig. 3.5B. Throughout the process, we utilized built-in functions in Matlab: $spectrogram()$ for PSD and $tfridge()$ for f_r.

   In computing the spectrogram, sampling window duration affects the PSD lobe width and thus affects the separation between f_rs from different sensors. We define $W_{0.1}$ as the width of the PSD lobe at 10% of the peak PSD value. Fig. 3.6 shows that the small Hamming window
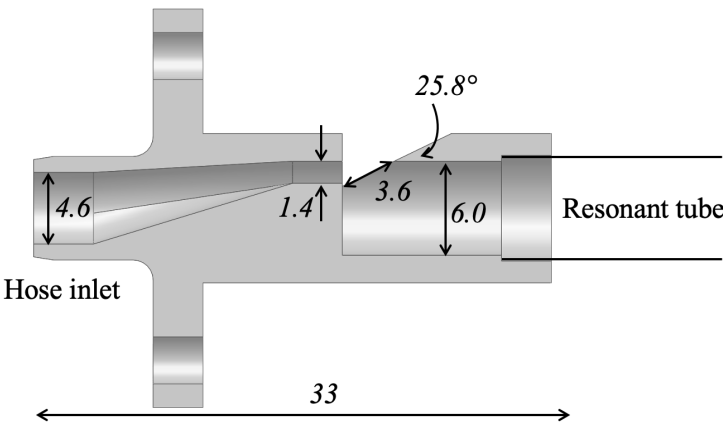
Figure 3.4: Cross sectional image of fipple geometry, with distance units in (mm). Air flow enters through hose inlet from the left.
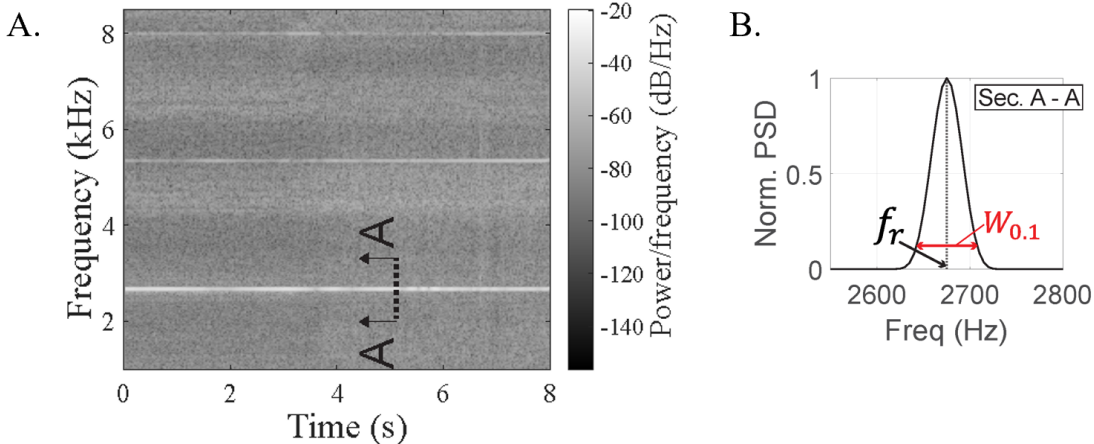
Figure 3.5: Spectrogram example of L=90 mm resonant tube and definition of f_r in the spectrogram. A. Spectrogram example of L=90 mm resonant tube and definition of f_r in the spectrogram. B. Cross sectional view of spectrogram taken from Section A-A.

size (< 20 ms) results in significantly wider $W_{0.1}$. Although the smaller window may update the information faster with low delay, the wide lobe allows fewer sensors not to overlap their f_r lobes. Because the $W_{0.1}$ does not decrease much for window size greater than 30 ms, we chose 33 ms as the Hamming window duration.
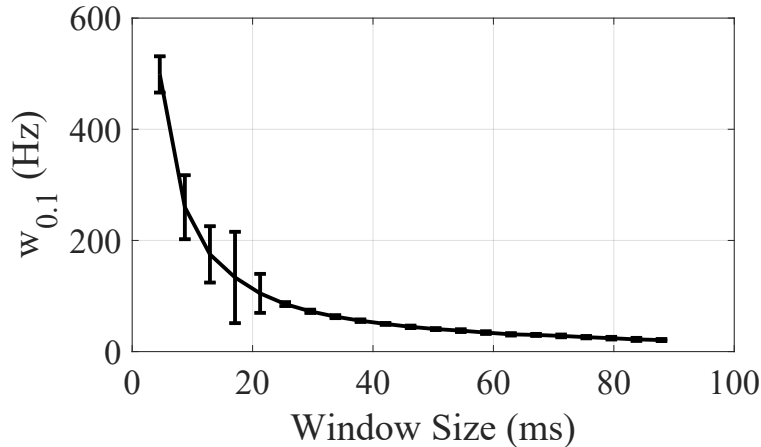
Figure 3.6: The effect of Hamming window size on the resonant frequency lobe when computing spectrogram.

3.4   Resonant Soft Finger

Implementation

We integrate the resonant pneumatic tactile sensor on a soft pneumatically-driven finger to measure proprioceptive curvature and detect contact. We use the design of the pneunet soft robotic gripper in *Soft Robotics Toolkit* [45] with a modified base layer to accommodate the resonant cavity tubes, as shown in Fig. 3.8. We cast the array of actuating bladders first and then cast the base layer with the resonant tube after the initial array is cured. The diameter of the tube is 6 mm and the length is 10 cm. Unlike the design in [45], we do not use any inextensible intermediate layers to simplify the fabrication process, and the entire body is silicone (Dragon Skin^TM 30). Two resonant tubes are on either side of the finger, maintaining symmetric free curling motion because each chamber structure stiffens its side of the finger. On a single finger, one tube can be used to measure pose while the other detects contact.

Pose estimation

We estimate the pose, or curvature of the gripper by measuring tube elongation. We first measure the resonant frequency (f_r) as the tube undergoes axial stretching. As shown in Fig. 3.9, we manually pulled a sample tube that was cutoff from the gripper in Fig. 3.8 left. We mark three red dots along the tube and track their location as we gently cyclically stretch the tube for 5 times. Fig. 3.9 right shows that f_r decreases as the tube elongates. Our sensor shows very low hysteresis unlike previous piezo-resistive bending sensors [38, 57].

Then, we test pose estimation using the pneumatic finger with the resonant tube integrated. We measure the curvature by detecting the three red dots marked on the gripper,
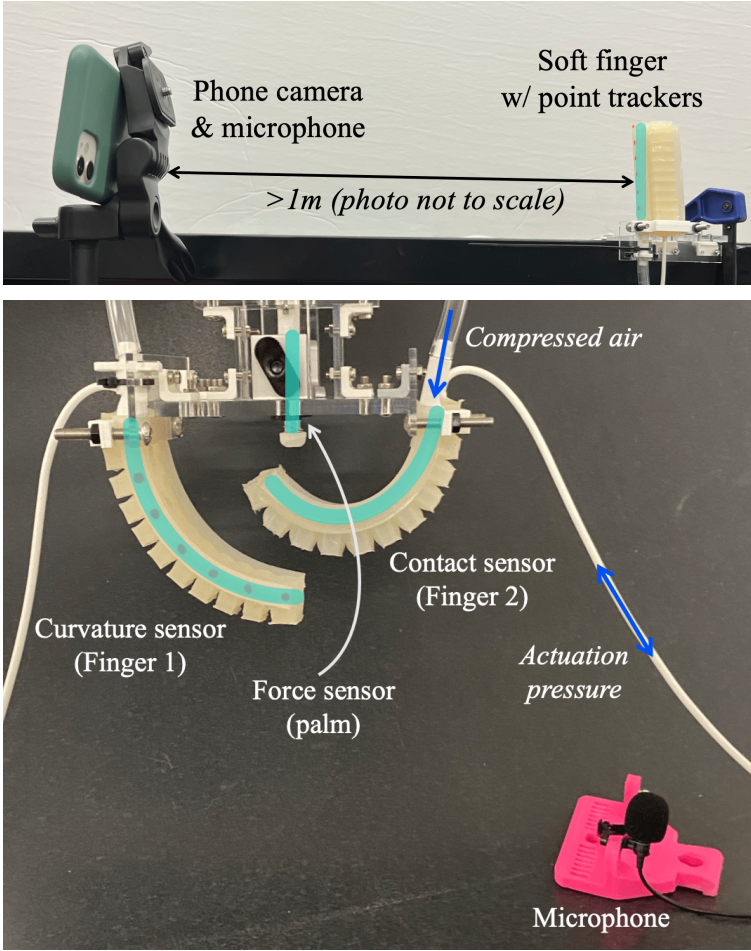
Figure 3.7: Experimental setup for both the sensor calibration (top) and gripper experiments (bottom). Resonant tubes are highlighted in cyan. The microphone is either built-in to the iPhone or plugged into a GoPro camera, and the microphone is located approximately 1m from the resonators.
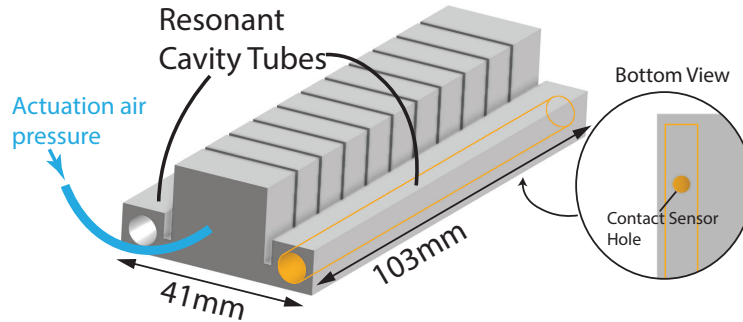
Figure 3.8: CAD of soft finger with resonant tubes. The contact sensor hole is located near the distal tip of the finger on the volar side. A fipple is fitted to the resonant cavity tube opening. The finger is actuated by pressurizing the central bladder chamber.

assuming circular curvature passing through three three marker locations. The result in Fig. 3.10 shows similar trends in f_r: the higher the curvature, the lower the f_r, and low hysteresis.

Contact sensing

We also characterize how frequency changes as the lateral opening on the fingertip is occluded. To test the contact sensing performance, we made a separate tube 11 cm long, using the same material as the soft fingers. We punched a hole (D=3.2 mm) at 10 mm from the distal end as shown in Fig. 3.8. Then, we placed the tube on top of a flat surface and slowly lowered a flat acrylic plate over the hole using the robot arm depicted in Fig. 3.11 left. We decremented the gap distance (h) while measuring the wrist force/torque sensor mounted on the robot arm. At close vicinity of the hole, decrements are 0.2 mm. At each h, we measured f_r for 330 ms and report the average f_r from each h in Fig. 3.11 (right). The distance $h = 0$ is determined as the point where the force/torque sensor measures a large change in the contact force.

Fig. 3.11 shows a gradual change in f_r with values of $h < 10\,mm$. Resonant frequency plateaus for $h > 10\,mm$ while the most signal change occurs between $0 < h < 2\,mm$. When the hole is clogged ($h < 0$), f_r saturates with respect to contact force. Contact vicinity sensing is particularly useful for controlling the soft gripper [65] because the inner surface of the gripper may not conform tightly to an object surface due to the curvature or weak grasp force. Soft finger sensor performance characteristics are listed in Table 3.1.

3.5   Resonant Force Probe

We present an alternative, rigid tube design characterization that uses the same principles as the soft finger, now implemented as a force probe for the gripper palm.
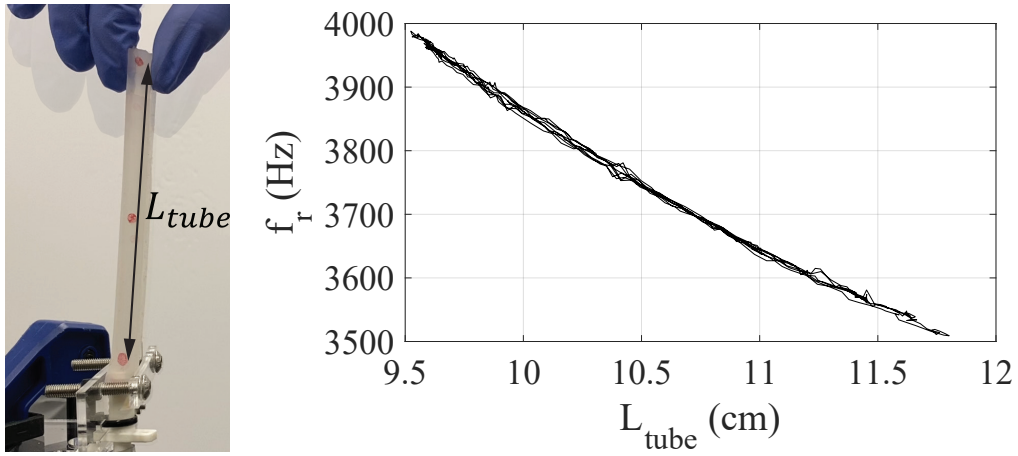
Figure 3.9: Stretch Test result of 5 loading cycles.
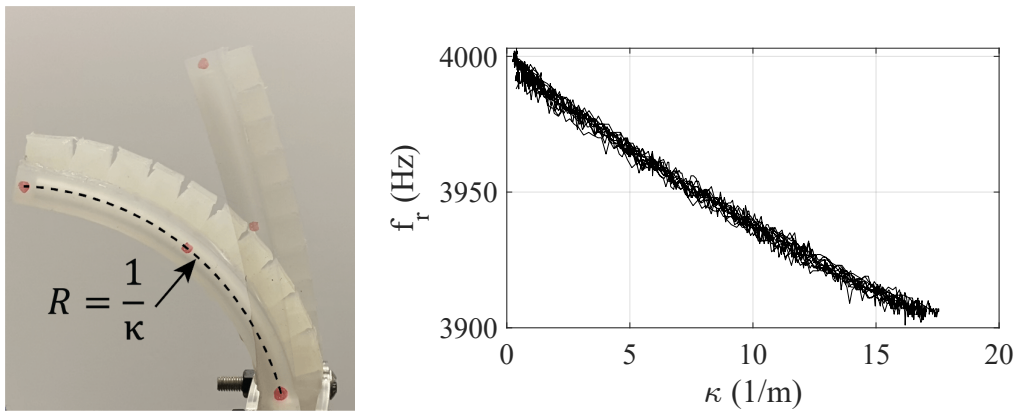
Figure 3.10: Bending Test result of 5 loading cycles.

Characteristic	Length (L_{tube})	Curv. (κ)	Contact (h)
Unloaded frequency [Hz]	3988	4003	4077
Full-scale output [Hz]	479	102	342
Dynamic range tested	$2.3\,\mathrm{cm}$	$17.3\,\mathrm{m^{-1}}$	$0\,\text{-}\,2\,\mathrm{mm}$

Table 3.1: Soft sensor performance characterization from the stretch, bending and contact test.

Implementation

This rigid resonant tube, shown in Fig. 3.12, is constructed using 3D printed PLA parts and telescoping aluminum tubes. A spherical PLA end-cap plugs the tube on the opposing
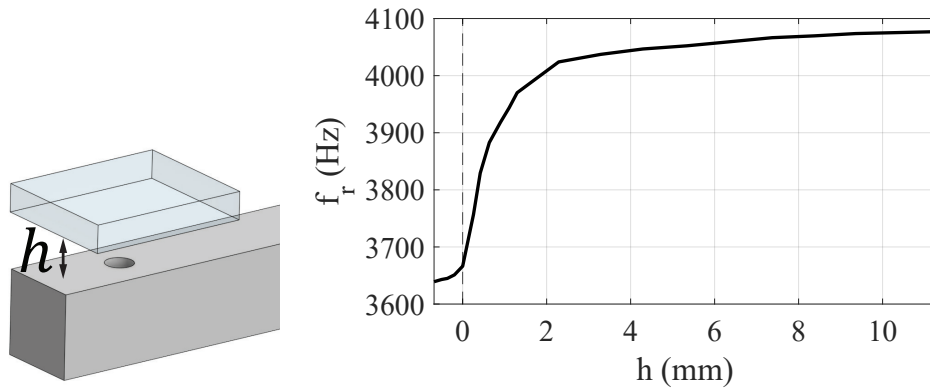
Figure 3.11: Contact Sensor Test
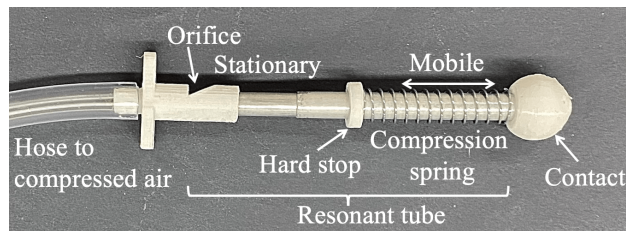
Figure 3.12: Force probe sensor. Air flows into the resonant tube from the left and out from the orifice above. Telescoping rods are employed to change the tube length; one is fixed and the other moves based on the force at the contact and stiffness of the spring. A hard stop is used to keep the mobile rod from falling out of the acrylic mounting structure (not shown).

end of the fipple. A thin foam is placed on the end-cap inside the tube to dampen pressure waves. The telescoping aluminum tubes have a clearance fit, which results in low sliding friction and low air leakage. The outer tube has an outer diameter of 7.1 mm (9/32").

For the purpose of characterization across different tube geometries and large length displacements, we test two different tube lengths, where the fipple edge to end distance when unloaded is either 90 mm (Test Taxel 1) or 130 mm (Test Taxel 2). The maximum displacement for both taxel designs is 25 mm. A spring restores the full length of the tubing when the taxel is unloaded. We test two different spring stiffnesses: 0.19 and 1.76 N/mm. For the gripper palm probe, we created a more compact version, with the resonant tube at 10 mm long when unloaded and a restoring spring stiffness of 1.0 N/mm.

Fig. 3.13 shows an example audiospectrogram of Taxel 1 during 5 compression cycles. Contact force decreases tube length and increases frequency, such that lower frequency is emitted when the taxel contact is unloaded. The fundamental frequency (n=1) is seen around 3 kHz and the second harmonic (n=2) is fainter in amplitude at about 6 kHz.
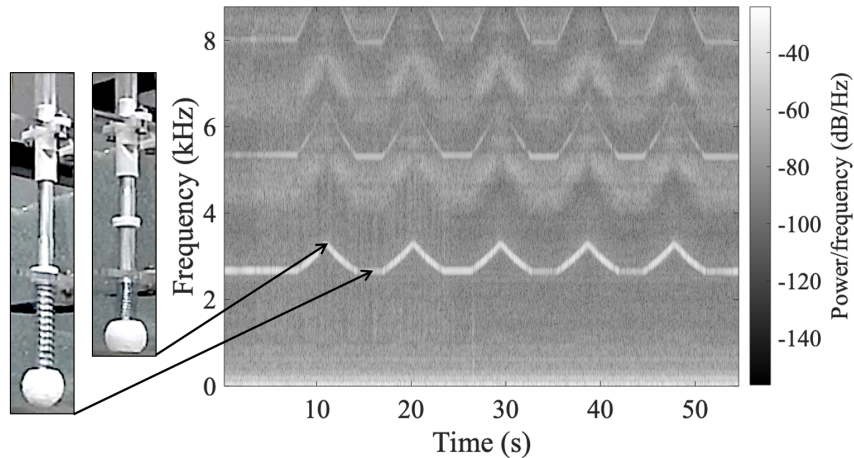
Figure 3.13: Audiospectrogram of Test Taxel 1 for 5 loading cycles.

Force sensing

We characterize the force sensor by rigidly mounting each taxel onto the robot arm and cyclically loading it at 6.2 mm/s against a rigid surface. Audio measurements are manually synced in post-processing. Characterizations for three combinations of force probe tube length and spring stiffness are presented in Table 3.2. The unloaded frequency of Taxel 2 ($T_{2,\text{soft}}$) is lower than Taxel 1 ($T_{1,\text{soft}}$) as it has a longer resonance cavity. Taxel 2 also has a lower full-scale output, expected from (3.1). The outputs of the two sensors with different tube lengths reside in frequency bands that do not overlap, allowing simultaneous measurements of the two. As expected, using the stiffer spring alters the sensitivity of Taxel 1 ($T_{1,\text{stiff}}$).

The calibration curves from 10 loading cycles for displacement and force are shown in Fig. 3.14, comparing $T_{1,\text{soft}}$ and $T_{1,\text{stiff}}$. The variation in displacement from the different springs, as seen in Fig. 3.14, is likely due to internal flexing of the acrylic mounting structure when subject to higher forces. Taxel sensitivity is linearly fit to all data, despite hysteresis that likely resulted from friction between the telescoping aluminum tubes. As a measure of sensor noise, the unloaded, or fully extended, frequency of Taxel 1 is recorded over 20 sec and results in a standard deviation of 1.65 Hz.

3.6 Robotic hand demonstration

We integrate two resonant soft fingers for opposed grasping on a robotic arm. We utilize the resonance tube in one finger for pose estimation and a tube in the other finger for contact sensing. Between the two fingers, the gripper palm has a resonant force probe. We demonstrate function of sensing modalities during object pick up and grasp failure of

Characteristic	$T_{1, soft}$	$T_{1, stiff}$	$T_{2, soft}$
Tube length [mm]	90	90	130
Spring stiffness [N/mm]	0.19	1.76	0.19
Unloaded frequency [Hz]	2650	2650	1840
Full-scale output (FSO) [Hz]	730	730	310
Dynamic range [N]	6.5	56	6.5
Sensitivity [Hz/N]	113	13	48

Table 3.2: Physical parameters and performance characterization of force probe sensor. The dynamic range of $T_{1, stiff}$ is linearly interpolated.
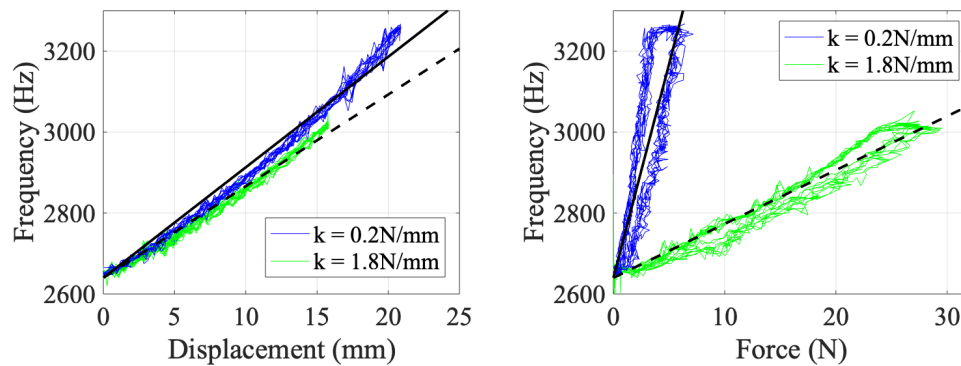
Figure 3.14: Calibration curves for Taxel 1. Frequency is linearly fit to displacement (left) and force (right). The soft spring is shown in blue and the stiff in green. 10 cycles are plotted.

a rectangular and circular foam object, showing varied gripper states represented in these sensor signals. While these two objects happen to also be soft, this sensitive soft gripper is applicable to objects with a variety of shapes and hardness. A video of these tasks is provided in supplemental media.

Gripper integration

We clamp the base of the soft fingers to the rigid palm base, shown in Fig. 3.7. A force probe is integrated in the center or the gripper, or palm. The inner distance between the two fingers is 108 mm (4 1/4"). The fingers are offset from the center by 26 mm (1.02") so they can curl fully without touching one another. The gripper design is not optimal and serves only as a platform to demonstrate the sensing modalities. The soft fingers are actuated by manual pressurization with 100 mL syringes. We sense curvature on Finger 1 (left) and contact on Finger 2 (right). The curvature sensor uses a different fipple geometry so the

frequency ranges of the sensors are distinct for ease of processing. The gripper is mounted onto the robotic arm with wrist force/torque sensing for the following grasping tasks.

Grasping tasks

Resonant tactile sensing is demonstrated for the grasping of a rectangular and cylindrical shaped foam object. Prior to grasping, both objects start on the table directly below the gripper. In state (1), the object is centered between the fingers and is not in contact with the gripper. In Fig. 3.15 towards the end of state (1), pressure increases and we detect an increase in curvature in the left (and right) finger. The fingers bend to grasp the cylindrical object, with an asymmetric pinch achieved by pressurizing Finger 1 more than Finger 2. We detect contact on Finger 2, demarcated by a sharp decrease in resonant frequency from A to B. During state (2), the object is in a steady grasp. As the object is pulled out of grasp, we observe an increase in frequency from B to A as contact is broken. In state (3), the object is no longer in the grasp and fingers are de-pressurized to state (4). This task shows how we can use the fingertip contact sensor to detect the presence and loss of grasped objects.

In the second task, we utilize the force sensor to detect objects in the palm to initiate grasping (Fig. 3.16). The robotic arm lowers the gripper until we detect palm force in state (2). The fingers close to grasp the object in state (3). The gripper lifts the object for state (4). When lifted, we do not detect force in the palm as the weight of the object pulls it away from the palm, but the constant curvature of the fingers indicate that the object remains in hand.

3.7 Discussion

This resonant pneumatic tactile sensor modality opens avenues for further investigation and innovation. While we designed this sensor to emit frequencies in the human hearing range, fipples and tubes may be designed to resonate in the ultrasonic range like dog whistles [118]. These sensors would have a shorter tube length, advantageous for miniaturization. They would also not be audible or distracting to people nearby. We show three simultaneous sensing elements on the gripper. The current audio processing fails when resonant frequencies overlap. To address this, we can make resonator geometry distinct, implement pneumatic valves switching each sensor, or incorporate more robust signal processing and learning.

In addition to elongation, pinching or compressing the soft resonant tube changes its frequency. Also, by coupling contact and curvature sensing in our current design, the signals simultaneously represent both phenomenon, making it difficult to discern the two with a single resonant tube. With multiple resonant tubes in a single finger, we can use one resonant tube for pose and the other for contact. The curvature effects can then be subtracted from the contact measurements to more accurately sense contact. Alternatively, future work could include the application of machine learning methods in order to interpret these complex signals in the context of manipulation.
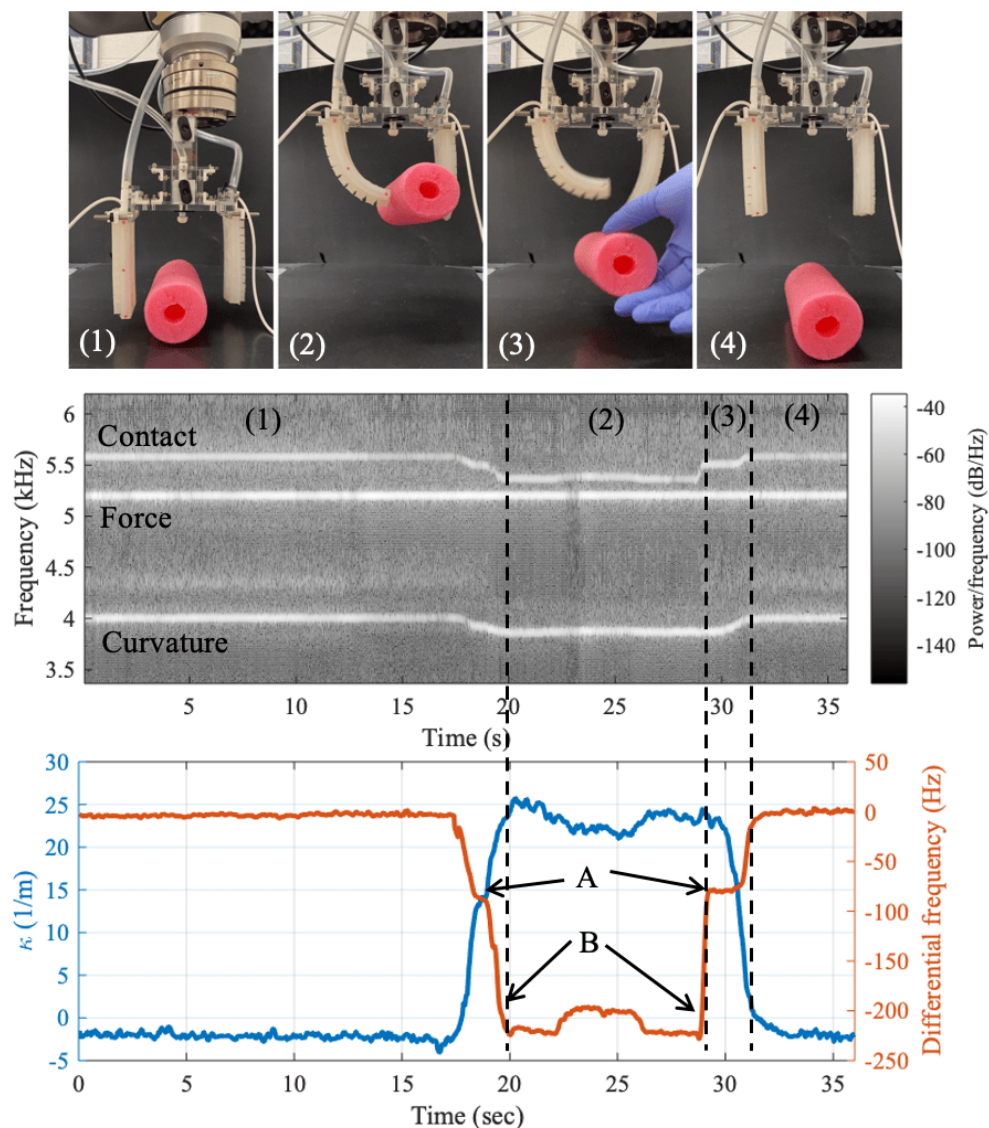
Figure 3.15: Contact detection during grasp. (1) pre-grasp. (2) grasping object. (3) object is pulled out and fingers are still curled. (4) uncurling fingers. We observe a sharp decrease in frequency from when the contact sensing hole is open (A) to closed (B). We detect a loss of contact when object is pulled out around 29 sec, and uncurl fingers.
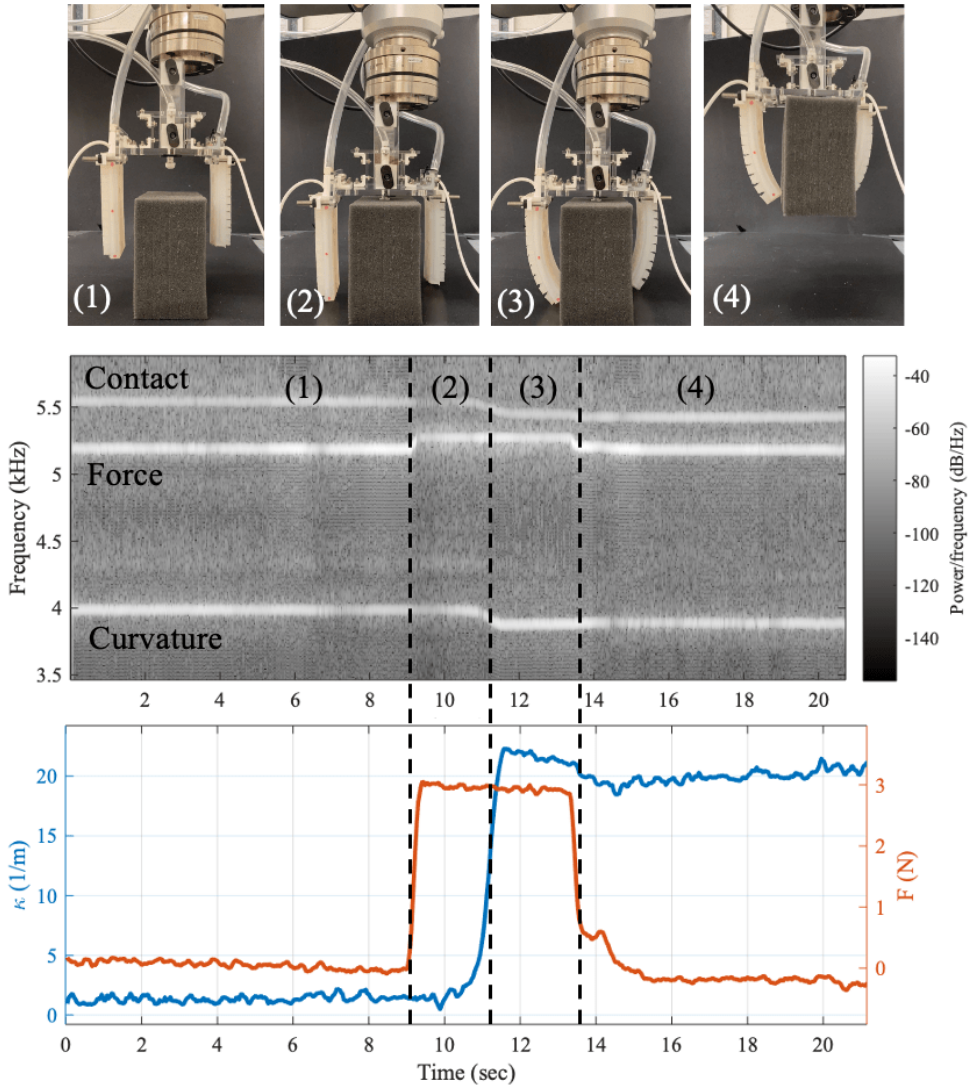
Figure 3.16: Object detection in palm and grasping. (1) pre-grasp position. (2) object detected in palm by force sensor. (3) grasping of object. (4) holding lifted object. The soft fingers are holding the object up and object is no longer pushing on palm.

As previously stated, resonant frequency depends on more than geometry. No resonance is produced without air flow. Increasing flow rate in a resonant system can result in slight increases in frequency as well as sudden jumps to higher harmonics. Atmospheric conditions, such as molecular composition and temperature will affect frequency as well. Hence, the sensor is most accurate when recalibrated prior to each use, or when coupled with other sensors that can measure atmospheric conditions or flowrate.

Issues may arise if the receiver cannot monitor the emitted frequencies, potentially due to high external noises or an insulated or obstructed emitter. Note that the resonance signal was easily detectable amidst typical research laboratory noises, from anywhere in the room. In environments where external disturbances are low in amplitude or not within the sensors' frequency range, this technology provides easy-to-integrate and inexpensive sensitivity that relays a rich understanding about the forces, contacts and movements experienced by soft systems.

3.8   Conclusion

Acoustic resonance chambers can equip soft robots with pose, contact and force sensing, taking advantage of the deformation inherent to these soft structures. One major benefit of this design is that electronics can be omitted from the end-effectors of robots, while rich signals are monitored with a single remote microphone located far from contact. Thus, these sensors are simple to integrate and can operate in conditions too harsh or impractical for electrical components in the end-effector. In this study, we find that these integrated pneumatic resonant sensors provide low hysteresis and capture the state of a soft gripper.

Chapter 4

Grasping in lubricated contact conditions

Real world environments, such as kitchens, present objects covered in viscous fluids: soap, oil, water, etc. Understanding and designing for slippery and submerged contact, where fluid lubrication is present, is a continuing challenge in the robotics community. Contact area, bending stiffness, and the presence of a viscous fluid affect friction. This work focuses on milliscale features (3 to 20 mm in size) of soft urethane skin on smooth, flat surfaces. We characterize the friction of soft skins, with varying size, and therefore bending stiffness, of cylindrical features, all with the same nominal contact area. In addition, a new method of frustrated total internal reflection with dye is introduced to visualize lubricated contact. We find that a small number of milliscale fingertip features maximizes friction force in the presence of lubrication, as compared both to un-patterned and many-featured skin designs. This holds true for a robotic gripper test, when pinching glass submerged in oil.

4.1 Introduction

Dexterous robots assisting in real world applications must capably execute manual tasks in the presence of variable contact conditions [81]. This chapter focuses on the wet and submerged environments present in applications varying from home service robots to remote ocean exploration. For example, dish-washing robots are being developed for at-home operation [120] and commercial purposes [2]. Robotic hands must grip objects covered in water, soap, oil, biofilms, etc. (Fig. 4.1). Slippery contact conditions can make it difficult to grasp objects with strength and reliability, and grasping with higher normal forces is not always feasible. This is especially true when handling fragile items like glassware. Modification of contact conditions through careful skin design can combat this slippery challenge. As stated in [18], "like the performance of a sports car which is ultimately limited by the tires on its wheels, the performance of a robotic hand is limited by the skin on its fingers."

Figure 4.1: Examples of manipulation with lubricated contact – a) The Robotiq gripper picks up a ceramic mug while using a set of soft fingerpads on extended fingertips. The latter of which prevents fluid exposure to electronics. b) Person washes dishes where water, soap and food residue make the pan slippery. Inset: Pressure distribution of a human fingertip that is wrinkly after prolonged exposure to wet conditions, cast in silicone rubber and pressed against the high-resolution tactile sensor developed for [28].

Soft robotic skin for frictional contact

Increasing friction through careful skin selection can aid in achieving force closure during robotic grasping [86]. Soft rubber is a popular skin option that distributes contact loads, reducing localized stress concentrations that could break fragile objects during grasping. Soft skin can also comply passively to an object's roughness and geometry, enabling interlocking between the surfaces. The details of geometry (i.e. number and shape of surface features) and material of soft skins contribute to their contact conditions. For example, in dry conditions, compliant cylindrical pads composed of a stiffer material result in higher friction [34]. One soft skin model describes how a set of discrete elastic cantilevers, where the stick-slip of each beam is modeled with Coulomb friction, can be combined to model friction of the system as a whole [44].

A number of works characterize how soft skin in dry contact conditions can be selected and controlled when applied to robotic manipulation. Grasp robustness is evaluated on a parallel-jaw gripper with silicone fingertips for a variety of surface features [39]. A friction-

tunable soft finger pneumatically induces ridges to control friction properties [122]. An increase in pressure is modeled and observed to increase the height of the finger's ridges and friction forces. In [85], a geometric surface design can passively switch between high and low contact area depending on normal force; it can either firmly grasp or slide past surfaces for different tasks. Friction of compliant fingertips is intentionally decreased by introducing fluid onto a slitted surface in [73]. These works do not address increasing friction during lubricated contact.

Researchers have noted how the fingerpads of humans, and some primates, wrinkle after prolonged exposure to water, shown in the inset of Fig. 4.1. The debate regarding the evolutionary role of water-induced wrinkling, and whether it improves the mechanics of manipulation in wet and submerged environments, is still ongoing [15, 41, 54]. A leading argument asserts that the tread-like features at the fingertips can enhance contact by reducing lubrication, similar to how treads reduce slipping on automobile tires and shoe soles, as in [59, 133]. However, a physical explanation that details the fluid lubrication effects with skin surface features, such as treads, still remains ambiguous. Recently, Mizushima, et al. [74] compared textured surfaces in dry and lubricated conditions to find that the size and shape of surface features affect friction. They focus on features 1 - 4 mm in size and found that slits perpendicular to the loading direction exhibit the highest friction coefficient when wet, among their tested geometries. The current study expands upon these findings to include large (>4 mm) cylindrical features. We also test whether trends for viscous squeeze flow translate to prehensile pinching in a real robotic hand.

Comparison to other contact technologies

Frictional soft skin is only one of many robotic contact solutions. For wet conditions, researchers are designing micropatterned surfaces that employ *capillary effect* for adhesion, enabling tasks like picking up a contact lens without squeezing [82]. Capillary effect can produce adhesion on wet surfaces [95] but is not applicable for grasping completely submerged objects as it relies on surface tension. *Gecko inspired adhesives* enable robots to resist large-scale shear forces on clean, dry surfaces [72, 98]. While surface functionalization can allow synthetic gecko adhesives to perform in wet conditions [61], it has not been applied to robotic manipulation. On rough surfaces, *microspines* are highly effective for applying tangential loads with a multifinger hand [129]. Spines have been applied effectively underwater via the JPL Nautilus Gripper that attaches onto rocks in the deep ocean [5] and a gripper composed of sets of blunted teeth for grasping hard corals [63]. However, interlocking with spines is not suitable for grasping smooth, flat, hard surfaces or when a surface should not be marred. *Suction* can enhance grasping, especially in submerged environments, and a constant suction flow at the fingertip increases grasp region of a hand [112]. This modality requires additional pumps and tubing to be installed on the robotic device. Contact technologies may also be combined. For example, a bio-inspired attachment mechanism utilizes both a suction seal and spines to grip onto smooth and rough surfaces underwater, resisting large normal and tangential forces [130].

We focus on passive, soft skin due to its mechanical simplicity, easy fabrication and integration, as well as its versatility in a wide number of applications.

Overview

Models for friction, bending stiffness and viscous fluid squeeze flow are presented in Section 4.2. Section 4.3 details the fabrication and experimental set-up used in testing frictional behaviors. A new method of visualizing lubricated contact area using frustrated total internal reflection is introduced. In Section 4.4, we find that an un-patterned soft skin has low friction in submerged conditions. Otherwise, friction force increases with bending stiffness of the surface features, a trend that holds true for dry and submerged trials. Lubricated friction force is therefore maximized at intermediate feature patterns. Section 4.5 discusses how the models for bending stiffness and lubrication support our experimental results. Section 4.6 highlights that milliscale skin features can enhance robotic grasping and describes future work for contact area imaging.

4.2 Friction Models and Fluid Effects on Contact

Models of dry friction, surface feature bending stiffness and viscous squeeze flow between two disks are detailed for comparison with experimental results in Section 4.4.

Contact models for dry friction

The simplest friction model is Coulomb or Amonton's Law. This model is best described by considering two cases. First, when there is no relative motion, the maximum friction force F_{fr} that is available to prevent motion is linearly proportional to the magnitude of the normal force F_N:

$$|F_{fr}| \leq \mu_s |F_N| \tag{4.1}$$

where μ_s is the coefficient of static friction. When relative motion is occurring, then the magnitude of the friction force is proportional to the magnitude of the normal force and it opposes the relative motion:

$$|F_{fr}| = \mu_k |F_N| \tag{4.2}$$

The coefficient μ_k is known as the coefficient of kinetic (or dynamic) friction.

Surface interactions between rubber and rigid objects typically match the Hertzian friction model [94]. Based on Hertzian elastic contact theory, friction force is proportional to the contact area between two surfaces; between a half-sphere and a flat plane, normal force is proportional to the cube of contact area [52]:

$$|F_{fr}| \propto R^2 \qquad R^3 \propto |F_N| \tag{4.3}$$

with radius of contact R. Combining the above, friction force is proportional to normal force to the two-thirds power. In actuality, friction is more nuanced. A power-scaling modification to Hertzian contact is used to more accurately model contact mechanics of soft robotic fingers, where contact radius is proportional to normal force to the 0-1/3 power [132]. This is an accurate model for elastic spherical contacts; but, changes in skin geometry and the presence of a lubricating film can have significant effects on friction that are not captured. In Section 4.4, we test for a trend between contact area and friction, with cylindrical features in lubricated conditions.

Bending stiffness of cylindrical surface features

Previously, researchers found that pad stiffness can either increase or decrease friction in dry conditions, depending on contact geometry [131]. For the cylindrical pad in contact with a flat, rigid face, researchers observed an increase in friction with increasing stiffness [34]. For skin pads with constant nominal contact area and feature height, varying the number of features changes their bending stiffness. A cantilevered beam with circular cross-section has stiffness k and moment of inertia I

$$k \;=\; \frac{3EI}{L^3}, \quad I \;=\; \frac{\pi R^4}{4} \tag{4.4}$$

with modulus of elasticity E, length of beam L, and mathematical constant π. R is the radius for a single contact. For n number of contacts that sum to the same nominal area A,

$$A = \pi R^2 = n\pi r^2. \tag{4.5}$$

We can write stiffness of a single feature as k_n:

$$k_n = \frac{3E}{L^3}\frac{\pi r^4}{4} = \frac{3E}{L^3}\frac{\pi R^4}{4n^2} \tag{4.6}$$

Assuming the superposition of stiffness for parallel features gives the total stiffness of a given skin pad, bending stiffness would decrease with the inverse of the number of features n:

$$k_{tot} = nk_n = \frac{3E}{L^3}\frac{\pi R^4}{4n} \;\Rightarrow\; k_{tot} \propto n^{-1} \tag{4.7}$$

In practice, when not all features are in contact with a surface, stiffness will be effectively lower. Furthermore, tangential forces deform flexible features, shifting contact to the edges. In the extreme case, flexible features bend so much that the cylinder walls are in contact with the surface. Bending stiffness estimated with Eqn. (4.4) is used when observing friction trends in Sec. 4.4.
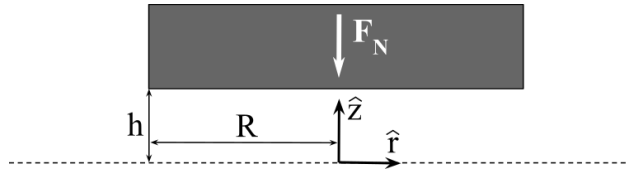
Figure 4.2: Schematic diagram for the Stefan-Reynolds equation that describes two parallel disks symmetrically squeezing together, showing only the top disk and the dashed center-line (representing the glass plate in this simplified model). The disk moves down at speed $\dot{h}$ given squeeze force F_N, as fluid flows out of the gap with height h.

Squeeze force of viscous fluid between two disks

The presence of a thin fluid film between end-effector and object can create slippery contact and result in grasp failure. For manipulation tasks in wet and submerged environments, dynamic fluid interactions must be taken into account. Derived in the Appendix and shown in the schematic diagram (Fig. 4.2), the Stefan-Reynolds equation describes fluid flow squeezing out of the gap between two parallel disks [62]. Assuming a Newtonian, incompressible fluid and the appropriate boundary conditions, the normal squeeze force to decrease the gap height for a single disk, F_N, is

$$F_N = -\frac{3}{8}\frac{\pi\eta\dot{h}R^4}{h^3} \tag{4.8}$$

with fluid viscosity η, closing velocity $\dot{h}$, radius R, and gap height h. Keeping all else constant, the squeeze force is proportional to viscosity, and in air this squeeze force usually goes unnoticed. The dynamic viscosity of canola oil, η_{oil}=5x10^{-2} kg/m·s [24], is more than three orders of magnitude greater than that of air, η_{air}=2x10^{-5} kg/m·s. Water has a dynamic viscosity of η_{water}=8x10^{-3} kg/m·s. Force increases as the fourth power of disk radius, indicating less force is required to squeeze smaller areas closer together. For a constant nominal contact area, contact consisting of many smaller circles rather than one large contact lowers total squeeze force required. Relating this to a fingerpad with multiple features,

$$F_{N,n} = \frac{1}{n}F_{N,tot} = -\frac{1}{n}\frac{3}{8}\frac{\pi\eta\dot{h}r^4}{h^3} \tag{4.9}$$

where $F_{N,n}$ is the normal force on a single feature on a pad with n features and $F_{N,tot}$ is the total normal force exerted. From Eqn. 4.9, we substitute in Eqn. 4.5 and rearrange to have

$$h^3 = -\frac{3}{8}\frac{\pi\eta\dot{h}R^4}{F_{N,n}n^3} \quad \Rightarrow \quad h \propto n^{-1}. \tag{4.10}$$

Thicker lubrication layers typically result in lower friction [40]. With the assumption that friction force decreases with gap height h, friction increases with feature number n. This formulation for viscous squeeze flow is based on normal force with a non-zero normal velocity, and has a limited application to sliding contact. However, we use it to provide insight on

the friction of soft contacts sliding across lubricated surfaces. We expect fluid lubrication effects to be most apparent in robotic hands with smooth, flat skin. Based on the analysis of bending stiffness and squeezed viscous flow, we expect a trade-off between stiffness and lubrication, which are both related to feature size.

4.3 Experimental Methods

This study tests soft skin pads with circular features of varying size and quantity with the same total nominal contact area. We use feature sizes up to 20 mm in diameter to fit on a humanoid robotic fingertip. The frictional behavior of skin pads is measured on dry glass and glass submerged in canola oil. Lubricated real contact area is imaged applying a modified frustrated total internal reflection technique.

Design and fabrication of soft skin pads

We designed soft skin pads to evaluate how surface feature size affects friction. Cylinders of varying size and quantity compose the surface features of the skin pads. Features fall within the same enclosed footprint and are circular to reduce asymmetry. (This is additionally addressed by changing orientation of the pads by 90° between the two experimental setups described in Sec. 4.3.) Surface features of each skin pad have a combined area of $32.3\,\text{mm}^2$ ($1/2\,\text{in}^2$), approximately the area of a United States penny. To evenly fit circular features into the same enclosed footprint, skin pads have 1, 3, 7, 13, 19, 31 and 55 features. Fabrication consists of casting urethane into negative molds, lasercut from acrylic. The size of the laser was accounted for to ensure constant nominal contact area across the different skins. The sets of skins were cast with urethane rubber of Shore A 30, 50, and 80 hardness (Smooth-On
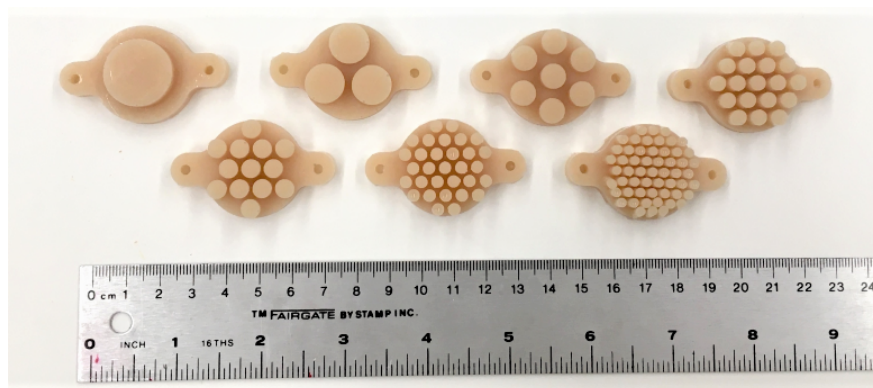
Figure 4.3: Photograph of soft skins cast with Shore A 30 hardness urethane (100% modulus $= 0.45\,\text{MPa}$). The total area of $32.3\,\text{mm}^2$ of each pad is divided into 1, 3, 7, 13, 19, 31 and 55 circular features. Both feature and base height are 6.4 mm.
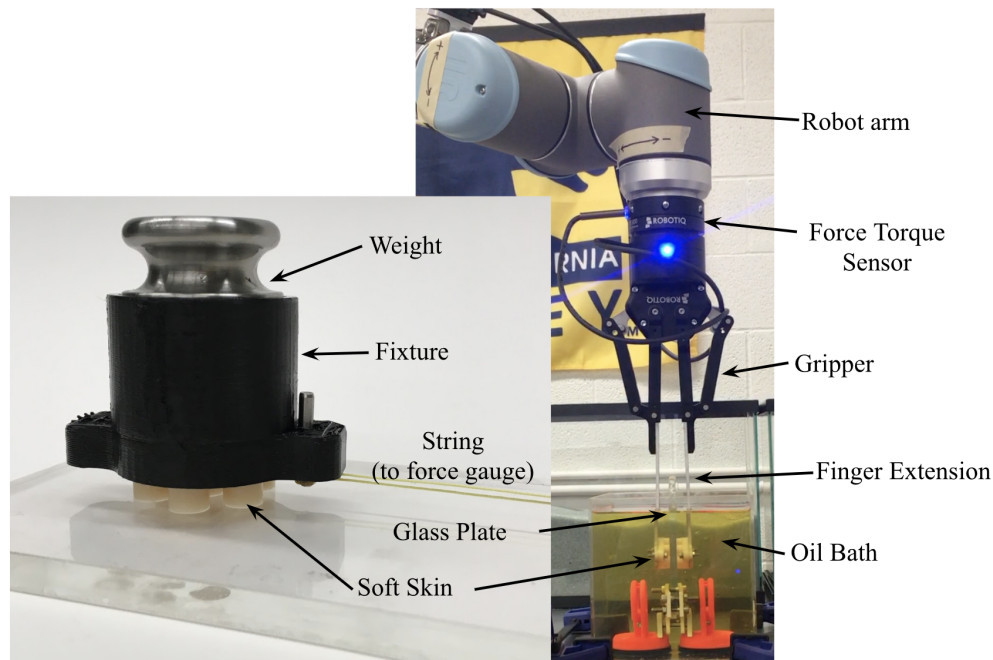
Figure 4.4: Experimental setup. Left: single-axis pull experiments. A soft skin and weight are fixed to a 3D printed mount. With a string attached to a force gauge, the skin is dragged across smooth glass, dry or submerged in oil, and the force is recorded real-time. Right: robotic arm with soft skin attached on the fingertips. The skin pinches and pulls up on a glass plate submerged in oil, and pullout force is recorded.

Vytaflex 30, 50 and Econ 80) with 100% modulus of 0.45, 1.48, 4.62 MPa, respectively. The bending stiffness of these contact pads ranges from 4.5 N/m for 55 Shore A 30 hardness features to 2600 N/m for the single 80A feature. All the features are 6.4 mm in height and are set on a 6.4 mm thick base, shown in Fig. 4.3.

Kinetic friction of soft skin on smooth glass

The resistive forces of these skin pads is tested on glass submerged in canola oil and clean, dry glass (Fig. 4.4 left). A 200 g mass is fixed above the skin pad, providing a normal force of approximately 2 N. A Mark-10 Series 4 force gauge is used to measure tangential forces as the weighted skin is dragged across a glass plate at approximately 10 cm/s via a tensioned string. Tangential force is recorded at 10 Hz averaged over one second for 10 trials. This measured force is divided by normal force for the kinetic friction coefficient. In this chapter we will refer to the *friction coefficient* of contact as the ratio of tangential to normal force, even though we acknowledge that it is only applicable to the specific testing conditions used, such as shearing rate. We assume that measuring the coefficient of kinetic friction provides a lower bound for coefficient of static friction.

Robotic pinching in a bath of oil

The internal squeezing force of a pinch grasp constrains contact surfaces differently than the constant normal force in the previous experiment. To verify translation of the results from weighted, single-axis experiments to robotics, the middle stiffness, 100% modulus = 1.48 MPa (Shore A 50 hardness), skin pads are also tested on a robotic gripper system. Skin pads are attached to extended fingertips of a 2-finger 140 Robotiq adaptive gripper for opposed pinching. The gripper is mounted on the UR10 robot arm from Universal Robots. The gripper pinches a glass plate in an oil bath and then moves upwards, dragging the skin pads across the glass with the positional uncertainty and drift of a real robotic system (Fig. 4.4 right). The Robotiq FT 300 Force Torque Sensor is used to measure pullout force of the glass. The squeeze force is approximately 4 N for the hard pinch and a 2 N for the light pinch. We compare this to dry pinching; however, the shear grasping forces were so high on the glass plate that a wooden block was used instead to avoid damage or finger wear. The finger pads are mounted to the robotic grasper such that they are loaded in an orientation perpendicular to the experiment in Sec. 4.3, to capture effects of contact feature orientation.

Contact imaging

An estimate of contact area is compared with measured friction force for dry and lubricated conditions. Real contact area between two surfaces often differs from apparent, or nominal, contact area. Frustrated total internal reflection (TIR) is an optical technique used to measure real contact area [7, 103]. LED lights with a red filter are wrapped around the edges of a 13 mm thick acrylic waveguide, as in Fig. 4.5. This technique relies on the difference in index of refraction between acrylic and air, 1.49 and 1.00 respectively, to achieve TIR.

When a surface comes into contact with one side of the waveguide, the red light scatters and is frustrated from the waveguide to the other side and recorded by a video camera (GoPro Hero4). In the lubricated case, a propylene glycol based dye (Americolor Candy Oil, green), refractive index similar to acrylic (1.43), covers the plate. We infer that the dye transmits light while maintaining TIR at the air interface. We chose a liquid with heavy pigment that absorbs transmitted light, thus enabling a measure of contact film thickness. Here, we assume a binary measure of contact based on color saturation and brightness of image. This measure is sensitive to post-processing and threshold selection. Characterizing the relationship between illumination, force and film thickness will be a part of future work. Even in dry conditions researchers have found increasing signal intensity with normal force [103].

The inset of Fig. 4.5 shows an example of the raw frustrated TIR image and contact area calculation of a single contact in wet and dry conditions. Images for dry contact were captured 0.1 sec before total slip and then matched with peak friction force. For the lubricated case, images and force measurements were taken midway through sliding. All images were collected using skin pads cast with Shore A 50 hardness urethane. A 100 g weight corresponding to 1 N of normal force was used for dry imaging because the heavier
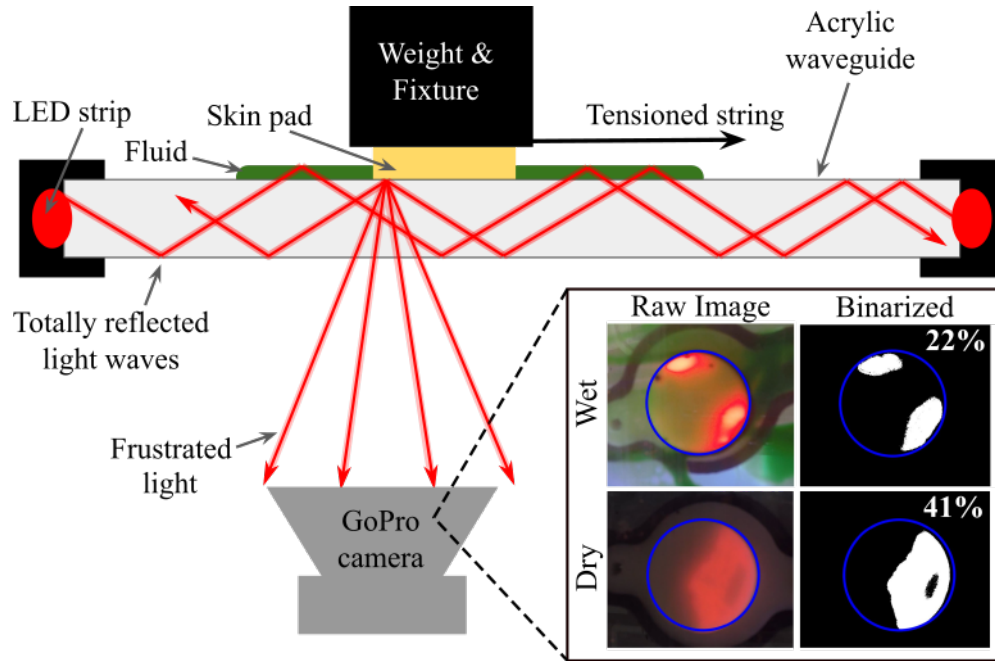
Figure 4.5: Schematic diagram of frustrated TIR technique setup. Light waves that initially undergo total internal reflection are scattered or frustrated from the acrylic waveguide by contact of the skin pad. This light is detected by a camera underneath and is used to estimate contact area. In the lubricated case, a fluid is selected that transmits the light while the pigmented fluid partially absorbs light such that skin pad contact is illuminated and the fluid is not. Raw frusturated TIR images and post-processing to calculate percent of real contact area (inset) are shown for wet and dry conditions. Nominal contact area is outlined in blue.

weight made tangential motion too difficult. Post-processing of images with a red color filter and binarization is used to calculate the percentage of real contact area compared to nominal contact area.

4.4 Results

Skin friction: feature size and stiffness

The kinetic friction coefficient of all skin designs in this study are plotted against number of features and total skin stiffness in Fig. 4.6. The skin pad exhibiting the highest kinetic friction coefficient has three features from the stiffest material. Overall for the stiffer materials (Shore A 50 and 80 hardness) and excluding the un-patterned pad, there is a positive correlation between summed stiffness k_{tot} and kinetic friction coefficient μ_k. In the presence of a lubricating fluid, the un-patterned skin pad requires little force to move, i.e. it is very slippery. This is consistent with previous studies where a smooth fingerpad was compared with

textures of 1 mm length scale [74]. For dry contact, the un-patterned skin pad exhibits the highest kinetic friction coefficient: between 1 and 3 for the skin materials tested. Differences in the kinetic friction coefficient between dry and submerged conditions are less apparent in skins with multiple surface features. The softest skin (Shore A 30 hardness) demonstrates increasing kinetic friction coefficient at the lowest stiffness range. We infer that the softest and most flexible features deform significantly during the experiments, resulting in new contact effects such as contact with the side walls of the features.

Robotic gripper pinch test

The mean and standard deviation of 30 gripper pullout force trials using Shore A 50 hardness pads, normalized with squeeze force, are plotted over the duration of the robotic grasping trials, shown in Fig. 4.7 for three cases: a strong (a) and light (c) pinch on glass submerged in canola oil, and on a dry wooden block (d). We take the initial peak pullout force over squeeze force to be the static friction coefficient. The time averaged pullout force over squeeze force after the initial peak is the kinetic friction coefficient. The static and kinetic friction coefficients from Fig. 4.7 (a) are synthesized in Fig. 4.7 (b). In oily conditions, pullout force for un-patterned contact was initially unnoticeable and gradually increased as the skin pads slid across the plate, indicating that the static friction coefficient for the un-patterned pad is lower than the kinetic. Skin pads with surface features have static friction coefficients greater than kinetic. For the featured skin pads, kinetic friction coefficient is relatively constant throughout the duration of the pull across glass. We observe lower kinetic friction coefficients for pads with many surface features, consistent with trends observed in Fig. 4.6. Thus, the friction trends from controlled lab experiments translate to more realistic grasping. In addition, any effect due to feature orientation, by rotating the finger pad orientation, is not observed.

A light pinch grasp yields similar results as hard grasping. Note that, under grasp forces of approximately 4 N smaller features visibly deformed as the skin was dragged across the glass but this was not observed with 2 N grasping. On dry wood, we observed no significant difference in pullout force for different surface features.

Contact Area Imaging

Imaging using the frustrated TIR technique provides insight for contact interactions between deformable and rigid surfaces. Presented in Fig. 4.8, we observe that contact area is not a strong indicator of friction force, indicating that Hertzian contact theory may not prove useful for these conditions. Note that, as described in Sec. 4.3, we are using an estimate of contact area specific to our sensor, so the results depend on this particular measurement method.

For dry contact, the soft skin does not slide. Rather, we observe a stick-slip behavior; sections of the pad are stuck to the surface while other sections are in motion, not in contact at all. The weight and fixture above the skin jiggle as portions of the skin surface undergo
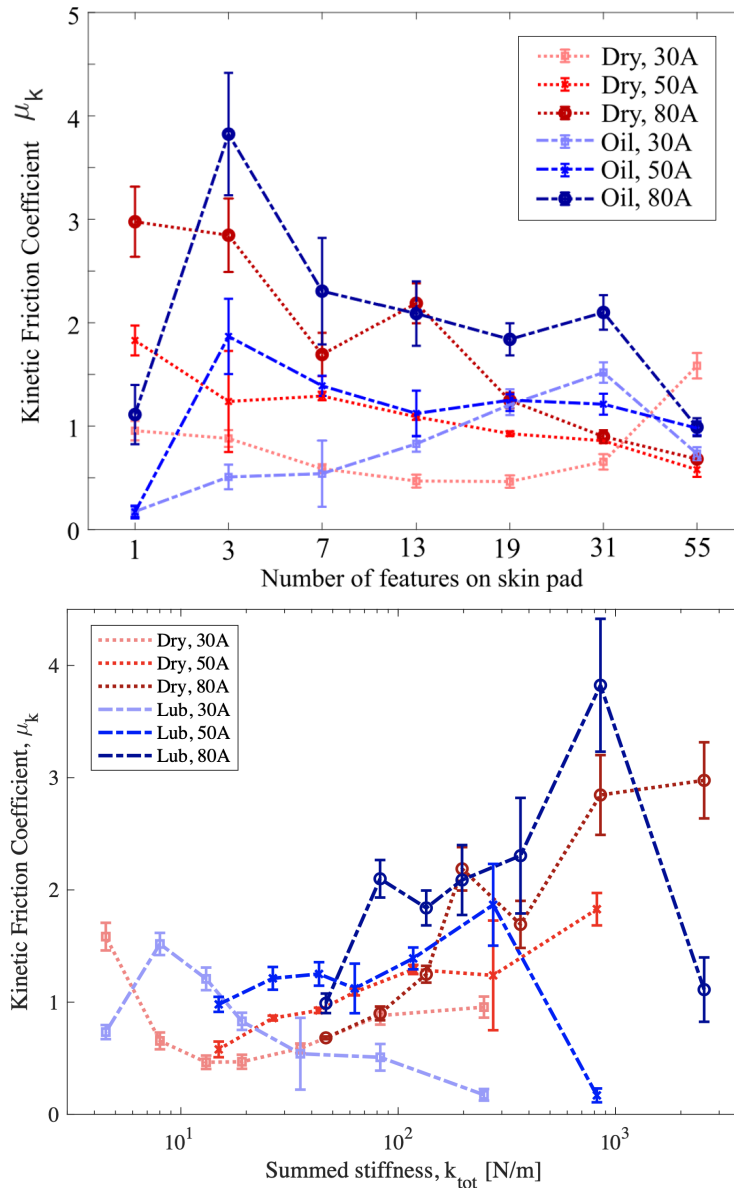
Figure 4.6: Kinetic friction coefficient plotted versus number of surface features (top) and bending stiffness of the soft skin pads (bottom). The test specimen were molded from urethane with hardness of Shore 30A, 50A, 80A. Experimental results are shown for friction on glass for dry (red) and lubricated (i.e. submerged in oil, blue) contact conditions.

stick-slip. When a rigid sphere moves across rubber at a fixed displacement distance, rather than a fixed force, researchers observe waves of contact and detachment and conclude that no true sliding occurs [6], consistent with our observations.

Fluid lubrication enables the skin to move across the glass with a smoother sliding motion. Lubricated friction trends match with those found in the submerged tests, indicating that wet
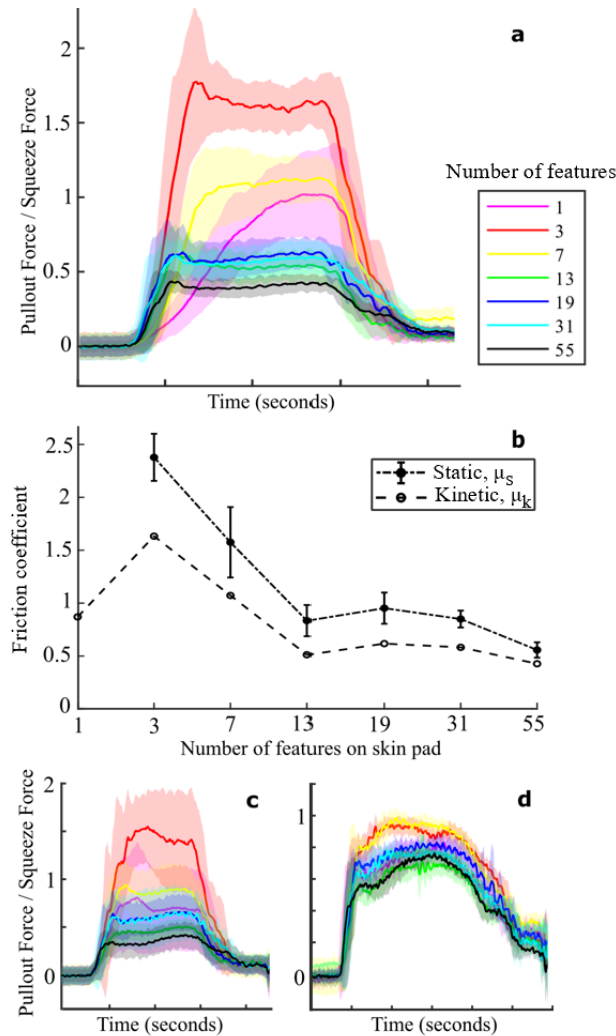
Figure 4.7: Pullout force of the robotic gripper pinching, averaged across 30 trials. (a) shows a pinch and pull test on a glass plate submerged in canola oil, with a squeeze force of approximately $4\,\text{N}$. (b) summarizes data from (a) to display static and kinetic friction coefficient of the skin pads. Additional pullout forces for (c) a light grasp on oily glass and (d) dry wood show that the effect of skin features in submerged conditions does not translate to dry conditions.

and submerged contact behave in similar ways in this study. Whether the two surfaces ever make real contact or are separated by a thin fluid film is unclear. Even if the surfaces make no real contact, shearing of the fluid in the gap produces a restraining force analogous to friction. In our observations, higher normal force increases real contact area as the features initially in contact comply, allowing contact of more features. When friction forces are especially high, we observe pronounced contact at the leading edge of the surface feature. We also note that the contact patches move around as the skin slides in the lubricated case;

	DRY F_N= 1N				
Friction force [N]:	3.2±0.3	2.6±0.2	2.2±0.2	1.8±0.2	1.4±0.2
Contact area [%]:	54±9	43±4	37±4	51±7	46±12

	WET F_N= 2N				
Friction force [N]:	<0.3	2.2±0.3	1.9±0.4	2.1±0.4	1.4±0.1
Contact area [%]:	45±9	51±3	85±14	54±3	23±10
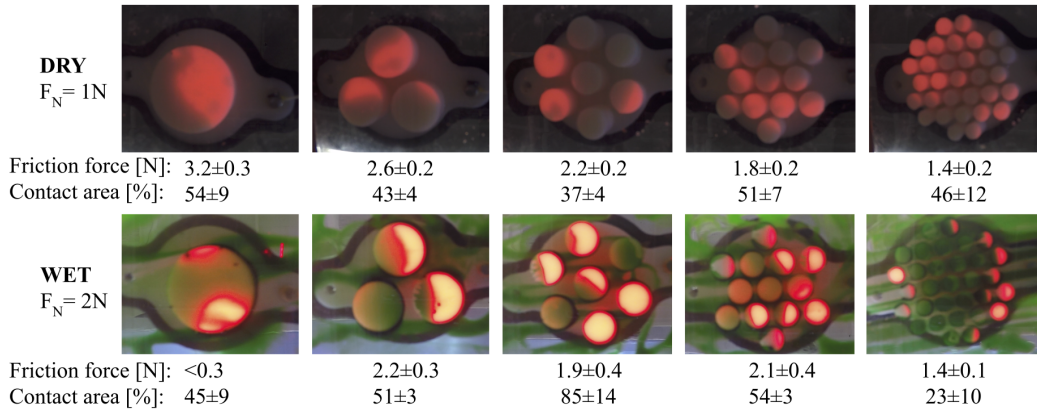
Figure 4.8: Contact area images taken using frustrated TIR for skin pads with 1, 3, 7, 13, and 31 features in dry and wet conditions. Friction and percent of real to nominal contact area are listed (N=4). Skin pads of Shore A 50 hardness are dragged across acrylic with a 1 N normal force. For dry contact, peak friction force and area 0.1 sec prior to total slip are recorded. Force and area measurements are taken midway through sliding in the lubricated case. The skin pads have the same nominal contact area, but exhibit clear differences in contact geometry.

different surface features come into and out of contact with the plate. For the un-patterned pad, the contact patches move towards the trailing edge.

4.5 Discussion

This study supports the expectation that there is a trade-off between feature stiffness and lubrication effect, both related to feature size, in the design of fingertip skin that maximizes friction for the handling of submerged surfaces. For the specific patterns tested, the stiffest skin pad material with three discrete features (each approximately 12 mm in diameter) provides the highest friction in lubricated conditions. This is an atypical robotic finger pad pattern. Increasing friction in this manner can help to improve the ability of robot hands to perform force closure and reduce the chance of dropping slippery objects, as compared with completely smooth or highly-patterned skins. Other robotics works, such as in [18], have discussed how friction predictability proves desirable for the control of robotic devices, rather than simply maximizing peak friction ability. Ultimately, skin selection for dexterous manipulation is a multi-faceted problem.

Future work

This study focused on feature size, while other factors may also affect friction force. A greater range of feature size could bridge the force and length scale from milliscale to microscale [58], providing a more complete guide for future designs. Decreasing the height of features would

make them stiffer and likely increase friction. In addition to the circular contact, different shapes can be systematically studied with quantifiable traits such as perimeter to area ratio, variation in perimeter curvature, etc. The circles were extruded for cylindrical features, where filleted edges may result in lower and more uniform friction. We anticipate that these rounded or hemispherical features will exhibit lower differences between the coefficient of static and kinetic friction, and between dry and lubricated conditions. Testing a number of different skin surface properties will produce new perspectives on parametric scaling properties. We are also interested in the fluid effects on initial contact between two surfaces e.g. dynamic grasping [113]. The treads of tires direct fluid away so the tire makes contact with the road [35], and a similar concept could be applied to robotic fingerpads.

A broadened scope of models and experiments can further establish the underlying mechanisms of slippery surfaces. Lubrication theory and the field of elastohydrodynamics, coupled with numerical modeling of fluid-structure interaction, may provide a more detailed physical explanation to observed behaviors. Additional experiments with canonical geometries and varying tangential velocity could place our system on the Stribeck curve [111]; this would determine if lubrication theory applies and in which lubrication regime we are operating. We note that the measured kinetic friction coefficients in this study are relatively high compared to those of typical lubricated systems such as journal (or plane) bearings. Calculating the fluid film height from plane wall-driven shear (or Couette) flow,

$$h = \frac{\eta V \pi R^2}{F_{fr}} \tag{4.11}$$

for tangential velocity V. Calculated with values from the robotic pinch test, the height of the fluid film is in the tens of nanometers. From Table 1 in [97], the surface roughness of acrylic is on the order of nanometers. These values indicate operation in the hydrodynamic lubrication regime, where a layer of fluid fully separates the two surfaces. We observe instances of a thick fluid film as the green and non-illuminated areas in Fig. 4.8. We used this frustrated TIR technique with pigmented fluid to measure contact area in both dry and lubricated conditions; decrypting the characteristics of this sensor via controlled distance, illumination and force experiments could yield new insights into fluid lubrication on soft structures and is a promising area for future investigation.

4.6 Conclusions

The design of milliscale features on the skin of robotic grippers can improve grasp security. Our results indicate that robots working in lubricated contact conditions may benefit from soft skin with a few surface features – as opposed to one or many – to achieve higher friction. Potential applications for this simple solution range from home assistance to remote exploration, when water and other lubricants are present.

4.7   Appendix

The following shows the derivation of Eqn. (4.8) and (4.10) from Section 4.2-C. We assume a Newtonian and incompressible fluid. Conservation of mass and momentum for a control volume between the two disks can be respectively expressed as $-\dot{h}\pi r^2 = 2\pi r \int_0^h v_r dz$ and $0 = -\frac{\partial p}{\partial r} + \eta \frac{\partial^2 v_r}{\partial z^2}$ with closing velocity $\dot{h}$, gap height h, radius r, and radial velocity v_r. The boundary conditions include no slip at the disk surface, maximum flow at the axial center, and atmospheric pressure (zero gauge pressure) outside the disks: $v_r(z = \pm h) = 0$, $\frac{\partial v_r}{\partial z}(z = 0) = 0$, $p(r = R) = 0$. Integrating the momentum equation twice with respect to z and using boundary conditions to solve for constants, the radial velocity is $v_r = \frac{1}{2\eta}\frac{\partial p}{\partial r}(z^2 - h^2)$. Using this formulation for v_r in mass conservation and integrating over r, pressure at the disk surface is $p = \frac{3}{4}\frac{\eta \dot{h}}{h^3}(R^2 - r^2)$. Integrating over area of the disk, the force the fluid exerts on the disk (Eqn. (4.8)) becomes $F_N = \frac{3\pi}{8}\frac{\eta \dot{h}}{h^3}R^4$. To find the relationship between force and radius or area of disk, we simplify with defining a constant $C \equiv \frac{3\pi}{8}\frac{\eta \dot{h}}{h^3}$ which gives $F_N = CR^4$. The total area A for n surface features of radius R_n is $A = n\pi R_n^2$, where the subscript n denotes multiple surface features. Comparing the force of the un-patterned pad with a single feature to that with n features, $F_{N, tot} = nF_{N, n} = nCR_n^4 = nC\frac{R_1^4}{n^2} = \frac{1}{n}R_1^4$. The total normal force scales with the inverse of feature number, hence $F_{N, tot} \propto n^{-1}$.

Chapter 5

Conclusion

This dissertation seeks to improve the functionality of robots in the real-world with designs at the physical contact interface, focusing on the role of fluids in the design of soft grippers. Defined as matter that cannot resist static shear, liquid and gas are both considered a fluid. As many robots operate in air or under water, designers have the opportunity to make systems that harness the ambient fluid.

AcousTac is a pneumatic tactile sensor that enables adaptive control strategies with no electronics near the end-effector. Inspired by human crossmodal perception, this design uses sound for tactile information. In Chapter 2, we describe the theoretical models relating resonant frequency and geometry, which captures the tube length but does not accurately describe the damped boundary condition of the compliant end cap. We also model the relationship between force and deformation of the hollow, hemispherical end cap, which closely follows the Hertzian elastic contact model. We use a smartphone camera to monitor sound and process it in the spectral domain. Using a robotic arm and force/torque sensor, we experimentally characterized tube length, end cap thickness, and the addition of two cap modifications: hole and mass. With a hole and amplitude thresholding, we can generate a monotonic force-frequency relationship that enables us to use AcousTac for force sensing with simple processing. In the tactile array demonstration, we show how AcousTac can be used for sensitizing soft surfaces. We also implement AcousTac on a suction cup gripper.

Chapter 3 expands this acoustic tactile sensor design to a soft gripper, where we sense finger pose, fingertip contact, and force at the palm. Soft actuators and grippers undergo large material deformations, which is an additional challenge for tactile sensor integration. AcousTac uses pneumatics to emit resonant acoustic frequencies dependent on the geometry of the soft actuators. The frequency is directly related to geometry, and we find the signal to be non-hysteretic, which is rare for tactile sensors and especially unusual for tactile sensing on soft systems. Even with the damping and unidealized deformations of the completely soft structure, length and curvature have linear relationships with frequency. Adding or casting resonant structures is a relatively simple fabrication process. Microphones are small, cheap, and already integrated in many robotic systems. Here, we applied fluid-driven sound to tactile sensing on soft surfaces and a soft gripper, but AcousTac can be implemented on

many more different forms. The AcousTac case study shows how, more generally, sound and fluids hold great potential for new uses in robotic design.

For underwater operation or other applications where liquids are present, the robotic system needs to be adapted to the environment, which requires more than making it waterproof. Water (and potentially biofilms) can be found at the contact surface which makes objects slippery and harder to grasp. Chapter 4 shows how we can increase friction by adding soft surface features to robotic fingerpads. Inspired by the wrinkling of human fingertips, this work mitigates the slippery effects of fluid lubrication. Current theoretical models do not accurately depict the shear force between two surfaces in lubricated conditions. We present theory on dry friction and viscous fluid flow between two plates, and measure the friction forces experimentally. We tested fingerpads of seven patterns and three materials, for a wide range of bending stiffnesses. From the two experimental test setups, fixed force and fixed displacement, the results are consistent; in lubricated conditions, a single or smooth fingerpad exhibits low friction while a fingerpad with a few features exhibits high friction. Through contact imaging using lubricated FTIR, we find that dry contact results in a classical stick-slip, where lubricated fingerpads have an apparent sliding motion across the surface. Of the fingerpad patterns tested, robot fingerpads should have a few stiff features for higher friction, rather than being smooth or finely textured. Adding soft, featured fingerpads onto existing robotic grippers is relatively simple, i.e. engineers do not need to switch out whole gripper and actuation system, yet can still improve grasp capabilities by changing the surface skin. By designing for the contact interface, especially in adversarial conditions such as fluid lubrication, we can enhance robot capabilities in the real-world.

The designs presented in my dissertation are influenced and motivated by my field testing experiences, photographed in Appendix B.1. We field tested a gripper design for sampling hard, plating corals on a human-portable remotely operated vehicle (ROV), detailed in Appendix A. The gripper has rotation-constrained teeth for anisotropic loading to improve grasping in positional uncertainty; objects slide further into grasp with a only couple Newtons of force but require much higher forces, tested up to 57N, to slip out. We integrated this gripper in an off-the-shelf ROV and tested it in the ocean off the coast of Curacao. When the object was within grasp, we were able to successfully grip onto a few corals and other plate-shaped objects. However, I had not accounted for positional uncertainty; maneuvering the gripper to the desired location and station keeping in open water was extremely challenging, resulting in many collisions between the gripper and world. Based on these real-world observations, the designs in my dissertation have soft components, in part to dampen collisions and be able to comply with grasping objects from various positions and angles. Future work includes testing AcousTac and milliscale featured fingerpads in real-world environments. This requires engineering innovation, potentially the development of an untethered pneumatic system to actuate AcousTac. Field testing results will guide how we can utilize fluids to build more capable robots.

Bibliography

[1] Sylvain Abondance, Clark B. Teeple, and Robert J. Wood. "A Dexterous Soft Robotic Hand for Delicate In-Hand Manipulation". In: *IEEE Robotics and Automation Letters* 5.4 (2020), pp. 5502–5509. DOI: 10.1109/LRA.2020.3007411.

[2] Evan Ackerman. *Dishcraft Robotics Takes Over Dishwashing From Humans - IEEE Spectrum*. June 2011. URL: https://spectrum.ieee.org/automaton/robotics/industrial-robots/dishcraft-robotics-takes-over-dishwashing-from-humans.

[3] Alan T. Asbeck et al. "Scaling Hard Vertical Surfaces with Compliant Microspine Arrays". In: *The International Journal of Robotics Research* 25.12 (2006), pp. 1165–1179. DOI: 10.1177/0278364906072511.

[4] Spencer B. Backus and Aaron M. Dollar. "Robust Resonant Frequency-Based Contact Detection With Applications in Robotic Reaching and Grasping". In: *IEEE/ASME Transactions on Mechatronics* 19.5 (2014), pp. 1552–1561. DOI: 10.1109/TMECH.2013.2287761.

[5] Spencer B. Backus et al. "Design and testing of the JPL-Nautilus Gripper for deep-ocean geological sampling". In: *Journal of Field Robotics* (2020). DOI: 10.1002/rob.21934.

[6] M. Barquins. "Sliding friction of rubber and Schallamach waves — A review". In: *Materials Science and Engineering* 73 (1985), pp. 45–63. ISSN: 0025-5416. DOI: 10.1016/0025-5416(85)90295-2.

[7] S. Begej. "Planar and finger-shaped optical tactile sensors for robotic applications". In: *IEEE Journal on Robotics and Automation* 4.5 (1988), pp. 472–484. DOI: 10.1109/56.20431.

[8] Aude Billard and Danica Kragic. "Trends and challenges in robot manipulation". In: *Science* 364.6446 (2019), eaat8414. DOI: 10.1126/science.aat8414.

[9] Lionel Birglen, Thierry Laliberté, and Clément M Gosselin. *Underactuated Robotic Hands*. Vol. 40. Springer Tracts in Advanced Robotics. 2007.

[10] Bruce Bower. "Doubts Aired over Neandertal Bone 'Flute'". In: *Science News* 153.14 (1998), pp. 215–215. ISSN: 00368423. URL: http://www.jstor.org/stable/4010441 (visited on 04/24/2023).

[11] Gerald Brantner and Oussama Khatib. "Controlling Ocean One". In: *Field and Service Robotics, Springer Proceeding in Advanced Robotics*. Vol. 5. 2018, pp. 3–17.

[12] Eric Brown et al. "Universal robotic gripper based on the jamming of granular material". In: *Proceedings of the National Academy of Sciences* 107.44 (2010), pp. 18809–18814. DOI: 10.1073/pnas.1003250107.

[13] John F. Bruno and Elizabeth R. Selig. "Regional Decline of Coral Cover in the Indo-Pacific: Timing, Extent, and Subregional Comparisons". In: *PLoS ONE* 2.8 (2007). Ed. by Rob Freckleton, e711.

[14] Angelo Cangelosi et al. "Embodied Intelligence". In: *Springer Handbook of Computational Intelligence*. Ed. by Janusz Kacprzyk and Witold Pedrycz. Berlin, Heidelberg: Springer Berlin Heidelberg, 2015, pp. 697–714. ISBN: 978-3-662-43505-2. DOI: 10.1007/978-3-662-43505-2_37.

[15] Mark Changizi et al. "Are Wet-Induced Wrinkled Fingers Primate Rain Treads?" In: *Brain, Behavior and Evolution* 77.4 (2011), pp. 286–290. ISSN: 0006-8977, 1421-9743. DOI: 10.1159/000328223.

[16] John W. Coltman. "Sounding Mechanism of the Flute and Organ Pipe". In: *The Journal of the Acoustical Society of America* 44.4 (1968), pp. 983–992. DOI: 10.1121/1.1911240.

[17] Vincent Creuze. "Monocular Odometry for Underwater Vehicles with Online Estimation of the Scale Factor". In: *20th World Congress of the Int. Federation of Automatic Control, Toulouse, France*. 2017.

[18] M. Cutkosky, J. Jourdain, and P. Wright. "Skin materials for robotic fingers". In: *1987 IEEE International Conference on Robotics and Automation Proceedings*. Vol. 4. Mar. 1987, pp. 1649–1654. DOI: 10.1109/ROBOT.1987.1087913.

[19] Mark R Cutkosky. "On grasp choice, grasp models, and the design of hands for manufacturing tasks". In: *IEEE Trans. on Robotics and Automation* 5.3 (1989), pp. 269–279.

[20] Mark R Cutkosky and William Provancher. "Force and tactile sensing". In: *Springer Handbook of Robotics* (2016), pp. 717–736.

[21] Mark R Cutkosky and John Ulmen. "Dynamic tactile sensing". In: *The human hand as an inspiration for robot hand development* (2014), pp. 389–403.

[22] R. S. Dahiya et al. "Tactile Sensing—From Humans to Humanoids". In: *IEEE Transactions on Robotics* 26.1 (2010), pp. 1–20.

[23] Ravinder S Dahiya and Maurizio Valle. *Robotic tactile sensing: technologies and system*. Springer, 2013.

[24] Lemuel M. Diamante and Tianying Lan. *Absolute Viscosities of Vegetable Oils at Different Temperatures and Shear Rate Range of 64.5 to 4835 s-1*. Research Article. 2014. DOI: https://doi.org/10.1155/2014/234583.

[25] D. Dornfeld and C. Handy. "Slip detection using acoustic emission signal analysis". In: *Proceedings. 1987 IEEE International Conference on Robotics and Automation.* Vol. 4. 1987, pp. 1868–1875.

[26] Daniel S Drew et al. "Acoustic communication and sensing for inflatable modular soft robots". In: *2021 IEEE International Conference on Robotics and Automation (ICRA)*. IEEE. 2021, pp. 11827–11833.

[27] Dylan Drotman et al. "Electronics-free pneumatic circuits for controlling soft-legged robots". In: *Science Robotics* 6.51 (2021), eaay2627. DOI: `10.1126/scirobotics.aay2627`.

[28] Eric V Eason et al. "Stress distribution and contact area measurements of a gecko toe using a high-resolution tactile sensor". In: *Bioinspiration & biomimetics* 10.1 (2015), p. 016013.

[29] Norbert Englebert et al. "Lower Mesophotic Coral Communities (60- 125 m Depth) of the Northern Great Barrier Reef and Coral Sea". In: *PLoS ONE* 12.2 (2017), e0170336.

[30] Benoit Fabre et al. "Aeroacoustics of Musical Instruments". In: *Annual Review of Fluid Mechanics* 44.1 (2012), pp. 1–25. DOI: `10.1146/annurev-fluid-120710-101031`.

[31] Thomas Feix et al. "The grasp taxonomy of human grasp types". In: *IEEE Trans. on Human-Machine Sys.* 46.1 (2016), pp. 66–77.

[32] Jeremy A. Fishel and Gerald E. Loeb. "Sensing tactile microvibrations with the Bio-Tac — Comparison with human sensitivity". In: *2012 4th IEEE RAS & EMBS International Conference on Biomedical Robotics and Biomechatronics (BioRob)*. 2012, pp. 1122–1127. DOI: `10.1109/BioRob.2012.6290741`.

[33] N. H. Fletcher. "Air Flow and Sound Generation in Musical Wind Instruments". In: *Annual Review of Fluid Mechanics* 11.1 (1979), pp. 123–146. DOI: `10.1146/annurev.fl.11.010179.001011`.

[34] Y. Fujihira et al. "Experimental investigation of effect of fingertip stiffness on resistible force in grasping". In: *2015 IEEE International Conference on Robotics and Automation (ICRA)*. 2015, pp. 4334–4340.

[35] T. F. Fwa et al. "Effectiveness of Tire-Tread Patterns in Reducing the Risk of Hydroplaning". In: *Transportation Research Record* 2094.1 (2009), pp. 91–102. DOI: `10.3141/2094-10`.

[36] Marco Gabiccini et al. "On the role of hand synergies in the optimal choice of grasping forces". In: *Autonomous Robots* 31.2 (2011), pp. 235–252.

[37] Kevin C. Galloway et al. "Soft Robotic Grippers for Biological Sampling on Deep Reefs". In: *Soft Robotics* 3.1 (2016), pp. 23–33.

[38] Tim Giffney et al. "Soft pneumatic bending actuator with integrated carbon nanotube displacement sensor". In: *Robotics* 5.1 (2016), pp. 1–9. ISSN: 22186581. DOI: `10.3390/robotics5010007`.

[39] M. Guo et al. "Design of parallel-jaw gripper tip surfaces for robust grasping". In: *2017 IEEE International Conference on Robotics and Automation (ICRA)*. 2017, pp. 2831–2838.

[40] Bernard J. Hamrock, Steven R. Schmid, and Bo O. Johnson. *Fundamentals of Fluid Film Lubrication*. New York, New York: Marcel Dekker, Inc., 2004.

[41] Julia Haseleu et al. "Water-Induced Finger Wrinkles Do Not Affect Touch Acuity or Dexterity in Handling Wet Objects". In: *PLoS ONE* 9.1 (Jan. 2014). ISSN: 1932-6203. DOI: `10.1371/journal.pone.0084949`.

[42] William E. Heap et al. "Soft Retraction Device and Internal Camera Mount for Everting Vine Robots". In: *2021 IEEE/RSJ International Conference on Intelligent Robots and Systems (IROS)*. 2021, pp. 4982–4988. DOI: `10.1109/IROS51168.2021.9636697`.

[43] Kosuke Higashi, Shogo Okamoto, and Yoji Yamada. "What is the Hardness Perceived by Tapping?" en. In: *Haptics: Perception, Devices, Control, and Applications*. Ed. by Fernando Bello, Hiroyuki Kajimoto, and Yon Visell. Lecture Notes in Computer Science. Cham: Springer International Publishing, 2016, pp. 3–12. ISBN: 978-3-319-42321-0. DOI: `10.1007/978-3-319-42321-0_1`.

[44] Van Anh Ho and Shinichi Hirai. "Modeling and Analysis of a Frictional Sliding Soft Fingertip, and Experimental Validations". In: *Advanced Robotics* 25.3-4 (Jan. 2011), pp. 291–311. ISSN: 0169-1864. DOI: `10.1163/016918610X552123`.

[45] Dónal P Holland et al. "The soft robotics toolkit: Shared resources for research and design". In: *Soft Robotics* 1.3 (2014), pp. 224–230.

[46] Robert D. Howe. "Tactile sensing and control of robotic manipulation". In: *Advanced Robotics* 8.3 (1993), pp. 245–261. DOI: `10.1163/156855394X00356`.

[47] Tae Myung Huh et al. "A Multi-Chamber Smart Suction Cup for Adaptive Gripping and Haptic Exploration". In: *2021 IEEE/RSJ International Conference on Intelligent Robots and Systems (IROS)*. 2021, pp. 1786–1793. DOI: `10.1109/IROS51168.2021.9635852`.

[48] A. Immas et al. "High-Bandwidth Underwater Wireless Communication using a Swarm of Autonomous Underwater Vehicles". In: *ASME 38th Int. Conf. on Ocean, Offshore and Arctic Eng.* 2019.

[49] K. Ishizu et al. "Preliminary experiments of a human-portable underwater gripper robot for dexterous tasks". In: *OCEANS 2014 MTS/IEEE Taipei*, pp. 1–7.

[50] Hao Jiang, Shiquan Wang, and Mark R Cutkosky. "Stochastic models of compliant spine arrays for rough surface grasping". In: *The Int. Journal of Robotics Research* 37.7 (2018), pp. 669–687.

[51] Roland S Johansson and J Randall Flanagan. "Coding and use of tactile signals from the fingertips in object manipulation tasks". In: *Nature Reviews Neuroscience* 10.5 (2009), pp. 345–359.

[52] K. L. Johnson. *Contact Mechanics*. Cambridge University Press, 1985. DOI: `10.1017/CBO9781139171731`.

[53] Minsu Kang et al. "Applications of Bioinspired Reversible Dry and Wet Adhesives: A Review". In: *Frontiers in Mechanical Engineering* 7 (2021). DOI: `10.3389/fmech.2021.668262`.

[54] Kyriacos Kareklas, Daniel Nettle, and Tom V. Smulders. "Water-induced finger wrinkles improve handling of wet objects". In: *Biology Letters* 9.2 (Apr. 2013). ISSN: 1744-9561. DOI: `10.1098/rsbl.2012.0999`.

[55] Oussama Khatib et al. "Ocean One: A robotic avatar for oceanic discovery". In: *IEEE Robotics & Automation Magazine* 23.4 (2016), pp. 20–29.

[56] J. Kim, S. Song, and S. Yu. "Development of Manipulation Purpose Small Agent Vehicle Using Momentum Gyro Wheel". In: *OCEANS 2018 MTS/IEEE Charleston*, pp. 1–7.

[57] Anastasia Koivikko et al. "Screen-printed curvature sensors for soft robots". In: *IEEE Sensors Journal* 18.1 (2018), pp. 223–230. ISSN: 1530437X. DOI: `10.1109/JSEN.2017.2765745`.

[58] Jiwoon Kwon et al. "Friction enhancement via micro-patterned wet elastomer adhesives on small intestinal surfaces". In: *Biomedical Materials* 1.4 (Oct. 2006), p. 216. DOI: `10.1088/1748-6041/1/4/007`.

[59] Samuel P Landers et al. *Pneumatic Tire Having Improved Wet Traction*. US Patent 6,450,223 B1. 2002.

[60] Cecilia Laschi, Barbara Mazzolai, and Matteo Cianchetti. "Soft robotics: Technologies and systems pushing the boundaries of robot abilities". In: *Science Robotics* 1.1 (2016), eaah3690. DOI: `10.1126/scirobotics.aah3690`.

[61] Haeshin Lee, Bruce P Lee, and Phillip B Messersmith. "A reversible wet/dry adhesive inspired by mussels and geckos". In: *Nature* 448.7151 (2007), pp. 338–341.

[62] Philip J. Leider and R. Byron Bird. "Squeezing Flow between Parallel Disks. I. Theoretical Analysis". In: *Industrial & Engineering Chemistry Fundamentals* 13.4 (Nov. 1974), pp. 336–341. ISSN: 0196-4313, 1541-4833. DOI: `10.1021/i160052a007`.

[63] Monica S. Li et al. "Gripper Design with Rotation-Constrained Teeth for Mobile Manipulation of Hard, Plating Corals with Human-Portable ROVs". In: *OCEANS - Marseille*. June 2019, pp. 1–6. DOI: `10.1109/OCEANSE.2019.8867340`.

[64] Monica S. Li et al. "Resonant Pneumatic Tactile Sensing for Soft Grippers". In: *IEEE Robotics and Automation Letters* 7.4 (2022), pp. 10105–10111. DOI: `10.1109/LRA.2022.3191186`.

[65] Yunquan Li, Yonghua Chen, and Yingtian Li. "Pre-charged pneumatic soft gripper with closed-loop control". In: *IEEE Robotics and Automation Letters* 4.2 (2019), pp. 1402–1408. ISSN: 23773766. DOI: 10.1109/LRA.2019.2895877.

[66] Gabriele Librandi, Eleonora Tubaldi, and Katia Bertoldi. "Programming nonreciprocity and reversibility in multistable mechanical metamaterials". In: *Nature Communications* 12 (2021), p. 3454.

[67] S. Licht et al. "Universal jamming grippers for deep-sea manipulation". In: *OCEANS 2016 MTS/IEEE Monterey*, pp. 1–5.

[68] Stephen T. Mahon et al. "Soft Robots for Extreme Environments: Removing Electronic Control". In: *2019 2nd IEEE International Conference on Soft Robotics (RoboSoft)*. 2019, pp. 782–787. DOI: 10.1109/ROBOSOFT.2019.8722755.

[69] Eric J. Markvicka et al. "An autonomously electronically self-healing liquid metal-elastomer composite for robust soft-matter robotics and electronics". In: *Nature Materials* 17 (2018), pp. 618–624.

[70] Uriel Martinez-Hernandez. "Tactile Sensors". In: *Scholarpedia of Touch*. Ed. by Tony Prescott, Ehud Ahissar, and Eugene Izhikevich. Paris: Atlantis Press, 2016, pp. 783–796. ISBN: 978-94-6239-133-8. DOI: 10.2991/978-94-6239-133-8_57.

[71] S. Maurice, B. Chide, and N. et al Murdoch. "In situ recording of Mars soundscape". In: *Nature* 605.7911 (Apr. 2022), pp. 653–658. DOI: 10.1038/s41586-022-04679-0.

[72] C. Menon, M. Murphy, and M. Sitti. "Gecko Inspired Surface Climbing Robots". In: *2004 IEEE International Conference on Robotics and Biomimetics, Shenyang*. June 2004, pp. 431–436.

[73] Kaori Mizushima et al. "Deformable fingertip with a friction reduction system based on lubricating effect for smooth operation under both dry and wet conditions". In: *Advanced Robotics* 33.10 (2019), pp. 508–519. DOI: 10.1080/01691864.2019.1608299.

[74] Kaori Mizushima et al. "Surface Texture of Deformable Robotic Fingertips for a Stable Grasp Under Both Dry and Wet Conditions". In: *IEEE Robotics and Automation Letters* 2.4 (Oct. 2017), pp. 2048–2055. ISSN: 2377-3774. DOI: 10.1109/LRA.2017.2717082.

[75] Paul R. Muir et al. "High species richness and lineage diversity of reef corals in the mesophotic zone". In: *Proceeding of the Royal Society B* 285.1893 (2018), pp. 1–7.

[76] Domenico Mura et al. "A Soft Modular End Effector for Underwater Manipulation: A Gentle, Adaptable Grasp for the Ocean Depths". In: *IEEE Robotics & Automation Magazine* 25.4 (2018), pp. 45–56.

[77] Richard M. Murray, S. Shankar Sastry, and Li Zexiang. *A Mathematical Introduction to Robotic Manipulation*. 1st. USA: CRC Press, Inc., 1994. ISBN: 0849379814.

[78] Werner Nachtigall. *Biological mechanisms of attachment*. Springer Science and Business Media, 2013.

[79] Philippe Nadeau et al. "Tactile sensing based on fingertip suction flow for submerged dexterous manipulation". In: *2020 IEEE International Conference on Robotics and Automation (ICRA)*. 2020, pp. 3701–3707. DOI: 10.1109/ICRA40945.2020.9197582.

[80] NASA. *MARS Sample Return Mission*. 2023. URL: https://mars.nasa.gov/msr/.

[81] Francesca Negrello, Hannah S Stuart, and Manuel G Catalano. "Hands in the real world". In: *Frontiers in Robotics and AI* 6 (2020), p. 147.

[82] Pho Van Nguyen and Van Anh Ho. "Grasping Interface With Wet Adhesion and Patterned Morphology: Case of Thin Shell". In: *IEEE Robotics and Automation Letters* 4.2 (2019), pp. 792–799. ISSN: 2377-3766, 2377-3774. DOI: 10.1109/LRA.2019.2893401.

[83] Ryuma Niiyama. "Soft Actuation and Compliant Mechanisms in Humanoid Robots". In: *Current Robotics Reports* 3.3 (2022), pp. 111–117.

[84] Shimon Y Nof. *Handbook of Industrial Robotics, 2nd Edition*. Wiley, 1999.

[85] Seita Nojiri et al. "Development of Contact Area Variable Surface for Manipulation Requiring Sliding". In: *2019 2nd IEEE International Conference on Soft Robotics (RoboSoft)*. Apr. 2019, pp. 131–136. DOI: 10.1109/ROBOSOFT.2019.8722754.

[86] Allison M Okamura, Niels Smaby, and Mark R Cutkosky. "An overview of dexterous manipulation". In: *Proceedings 2000 ICRA. Millennium Conference. IEEE International Conference on Robotics and Automation. Symposia Proceedings (Cat. No. 00CH37065)*. Vol. 1. IEEE. 2000, pp. 255–262.

[87] Julie B. Olson and Christina A. Kellogg. "Microbial ecology of corals, sponges, and algae in mesophotic coral environments". In: *FEMS Microbiology Ecology* 73.1 (2010), pp. 17–30.

[88] John M. Pandolfi et al. "Global Trajectories of the Long-Term Decline of Coral Reef Ecosystems". In: *Science* 301.5635 (2003), pp. 955–958.

[89] Gaoyang Pang, Geng Yang, and Zhibo Pang. "Review of Robot Skin: A Potential Enabler for Safe Collaboration, Immersive Teleoperation, and Affective Interaction of Future Collaborative Robots". In: *IEEE Transactions on Medical Robotics and Bionics* 3.3 (2021), pp. 681–700. DOI: 10.1109/TMRB.2021.3097252.

[90] Gaoyang Pang et al. "CoboSkin: Soft robot skin with variable stiffness for safer human–robot collaboration". In: *IEEE Transactions on Industrial Electronics* 68.4 (2020), pp. 3303–3314.

[91] Yong-Lae Park, Bor-Rong Chen, and Robert J. Wood. "Design and Fabrication of Soft Artificial Skin Using Embedded Microchannels and Liquid Conductors". In: *IEEE Sensors Journal* 12.8 (2012), pp. 2711–2718. DOI: 10.1109/JSEN.2012.2200790.

[92] A Parness et al. "A microfabricated wedge-shaped adhesive array displaying gecko-like dynamic adhesion, directionality and long lifetime". In: *J R Soc Interface* 6.6 (2009), pp. 1223–1232. DOI: 10.1098/rsif.2009.0048.

[93] A. Parness and M. Frost. "Microgravity coring: A self-contained anchor and drill for consolidated rock". In: *2012 IEEE Aerospace Conference*, pp. 1–7.

[94] B. N. J. Persson. "Theory of rubber friction and contact mechanics". In: *The Journal of Chemical Physics* 115.8 (2001), pp. 3840–3861. ISSN: 0021-9606. DOI: `10.1063/1.1388626`.

[95] B. N. J. Persson. "Wet adhesion with application to tree frog adhesive toe pads and tires". en. In: *Journal of Physics: Condensed Matter* 19.37 (Aug. 2007), p. 376110. ISSN: 0953-8984. DOI: `10.1088/0953-8984/19/37/376110`.

[96] Brennan T. Phillips et al. "A Dexterous, Glove-Based Teleoperable Low-Power Soft Robotic Arm for Delicate Deep-Sea Biological Exploration". In: *Scientific Reports* 8 (2018), pp. 1–9.

[97] Muhammad Rizwanur Rahman and Prashant Waghmare. "Double-Emulsion Drop Evaporation and Formation of a Daughter Droplet". In: *Langmuir* 35 (Feb. 2019). DOI: `10.1021/acs.langmuir.8b03862`.

[98] Jean-Philippe Roberge et al. "Improving industrial grippers with adhesion-controlled friction". In: *IEEE Robotics and Automation Letters* 3.2 (2018), pp. 1041–1048.

[99] Peter Roberts, Mason Zadan, and Carmel Majidi. "Soft tactile sensing skins for robotics". In: *Current Robotics Reports* 2 (2021), pp. 343–354.

[100] Daniela Rus and Michael T. Tolley. "Design, fabrication and control of soft robots". In: *Nature* 512 (2015), pp. 467–475.

[101] Norimitsu Sakagami et al. "Development of an underwater robotic inspection system using mechanical contact". In: *Journal of Field Robotics* 30.4 (2013), pp. 624–640.

[102] Schilling-Robotics–FMC-Technologies. *Manipulator Systems*. Apr. 2019. URL: `http://fmcenergysystems.com/en/SchillingRobotics/Schilling-Manipulators.aspx`.

[103] James S. Sharp, Stuart F. Poole, and Benjamin W. Kleiman. "Optical Measurement of Contact Forces Using Frustrated Total Internal Reflection". In: *Physical Review Applied* 10.3 (Sept. 2018), p. 034051. DOI: `10.1103/PhysRevApplied.10.034051`. (Visited on 07/13/2019).

[104] Hongshen Shi et al. "Touching the Sound: Audible Features Enable Haptics for Robot Control". In: *IEEE Robotics & Automation Magazine* (2022).

[105] Benjamin Shih et al. "Design Considerations for 3D Printed, Soft, Multimaterial Resistive Sensors for Soft Robotics". In: *Frontiers in Robotics and AI* 6 (2019). ISSN: 2296-9144. DOI: `10.3389/frobt.2019.00030`.

[106] H. Shinoda, K. Matsumoto, and S. Ando. "Acoustic resonant tensor cell for tactile sensing". In: *Proceedings of International Conference on Robotics and Automation*. Vol. 4. 1997, 3087–3092 vol.4. DOI: `10.1109/ROBOT.1997.606757`.

[107] Enrico Simetti et al. "Floating underwater manipulation: Developed control methodology and experimental validation within the TRIDENT project". In: *Journal of Field Robotics* 31.3 (2014), pp. 364–385.

[108] Ana Correia Simões et al. "Designing human-robot collaboration (HRC) workspaces in industrial settings: A systematic literature review". In: *Journal of Manufacturing Systems* 62 (2022), pp. 28–43.

[109] Nina R Sinatra et al. "Ultragentle manipulation of delicate structures using a soft robotic gripper". In: *Science Robotics* 4.33 (2019), eaax5425.

[110] Fredrik Søreide. *Ships from the depths: deepwater archaeology.* Texas A&M University Press, 2011.

[111] R Stribeck. *Kugellager F ur beliebige Belastungen Zeitschrift des Vereins Deutscher Ingenieure.* 1901.

[112] Hannah Stuart, Shiquan Wang, and Mark R Cutkosky. "Tunable Contact Conditions and Grasp Hydrodynamics using Gentle Fingertip Suction". In: *IEEE Transactions on Robotics* (2018).

[113] Hannah Stuart et al. "The Ocean One hands: An adaptive design for robust marine manipulation". In: *The International Journal of Robotics Research* 36.2 (2017), pp. 150–166. DOI: `10.1177/0278364917694723`.

[114] Hannah Stuart et al. "The Ocean One hands: An adaptive design for robust marine manipulation". In: *The Int. Journal of Robotics Research* 36.2 (2017), pp. 150–166.

[115] Huanbo Sun, Katherine J Kuchenbecker, and Georg Martius. "A soft thumb-sized vision-based sensor with accurate all-round force perception". In: *Nature Machine Intelligence* 4.2 (2022), pp. 135–145.

[116] Keita Takeuchi et al. "Development of Multi-Joint Gripper for Underwater Operations". In: *OCEANS Techno-Ocean 2018 MTS/IEEE Kobe*, pp. 1–6.

[117] C Tawk, R Mutlu, and G Alici. "A 3D Printed Modular Soft Gripper Integrated With Metamaterials for Conformal Grasping". In: *Front Robot AI* (2022). DOI: `10.3389/frobt.2021.799230`.

[118] Leavens Theodore. *Dog Whistle.* US Patent 2245484A. Nov. 1940.

[119] Stephen Timoshenko and James N. Goodier. *Theory of Elasticity.* Third. New York: McGraw-Hill, pp. 372–376.

[120] *Tokyo Univ. Technology that supports dish washing with kitchen robots.* 2008. URL: `http://www.irt.i.u-tokyo.ac.jp/en/reform/081217/index.shtml`.

[121] Michael T. Tolley et al. "A Resilient, Untethered Soft Robot". In: *Soft Robotics* 1.3 (2014), pp. 213–223. DOI: `10.1089/soro.2014.0008`.

[122] Hiep Xuan Trinh, Van Anh Ho, and Koji Shibuya. "Theoretical Foundation for Design of Friction-Tunable Soft Finger With Wrinkle's Morphology". In: *IEEE Robotics and Automation Letters* 4.4 (Oct. 2019), pp. 4027–4034. ISSN: 2377-3774. DOI: `10.1109/LRA.2019.2926960`.

[123] Ryan L. Truby et al. "Fluidic innervation sensorizes structures from a single build material". In: *Science Advances* 8.32 (2022), eabq4385. DOI: `10.1126/sciadv.abq4385`.

[124] Ryan L. Truby et al. "Soft Somatosensitive Actuators via Embedded 3D Printing". In: *Advanced Materials* 30.15 (2018), p. 1706383. DOI: `https://doi.org/10.1002/adma.201706383`.

[125] Madeleine J. H. Van Oppen et al. "The role of deep reefs in shallow reef recovery: an assessment of vertical connectivity in a brooding coral from west and east Australia". In: *Molecular Ecology* 20.8 (2011), pp. 1647–1660.

[126] S. M. G. Vidwath et al. "Soft Robotic Gripper for Agricultural Harvesting". In: *Machines, Mechanism and Robotics*. Ed. by Rajeev Kumar et al. Singapore: Springer Singapore, 2022, pp. 1347–1353. ISBN: 978-981-16-0550-5.

[127] Vincent Wall and Oliver Brock. "A Virtual 2D Tactile Array for Soft Actuators Using Acoustic Sensing". In: *2022 IEEE/RSJ International Conference on Intelligent Robots and Systems (IROS)*. 2022, pp. 10029–10034. DOI: `10.1109/IROS47612.2022.9981225`.

[128] Yongbiao Wan, Yan Wang, and Chuan Fei Guo. "Recent progresses on flexible tactile sensors". In: *Materials Today Physics* 1 (2017), pp. 61–73. ISSN: 2542-5293. DOI: `https://doi.org/10.1016/j.mtphys.2017.06.002`.

[129] Shiquan Wang et al. "Spinyhand: Contact load sharing for a human-scale climbing robot". In: *Journal of Mechanisms and Robotics* 11.3 (2019).

[130] Yueping Wang et al. "A biorobotic adhesive disc for underwater hitchhiking inspired by the remora suckerfish". In: *Science Robotics* 2.10 (2017). DOI: `10.1126/scirobotics.aan8072`.

[131] T. Watanabe and Y. Fujihira. "Experimental investigation of effect of fingertip stiffness on friction while grasping an object". In: *2014 IEEE International Conference on Robotics and Automation (ICRA)*. May 2014, pp. 889–894. DOI: `10.1109/ICRA.2014.6906959`.

[132] Nicholas Xydas and Imin Kao. "Modeling of Contact Mechanics and Friction Limit Surfaces for Soft Fingers in Robotics, with Experimental Results". In: *The International Journal of Robotics Research* 18.9 (Sept. 1999), pp. 941–950. ISSN: 0278-3649. DOI: `10.1177/02783649922066673`.

[133] Takeshi Yamaguchi and Kazuo Hokkirigawa. "Development of a High Slip-resistant Footwear Outsole Using a Hybrid Rubber Surface Pattern". In: *Industrial Health* 52.5 (2014), pp. 414–423. DOI: `10.2486/indhealth.2014-0105`.

[134]   Wenzhen Yuan, Siyuan Dong, and Edward H Adelson. "Gelsight: High-resolution robot tactile sensors for estimating geometry and force". In: *Sensors* 17.12 (2017), p. 2762.

[135]   Gabriel Zöller, Vincent Wall, and Oliver Brock. "Acoustic Sensing for Soft Pneumatic Actuators". In: *2018 IEEE/RSJ International Conference on Intelligent Robots and Systems (IROS)*. 2018, pp. 6986–6991. DOI: 10.1109/IROS.2018.8594396.

Appendix A

Marine sampling gripper design and field testing

A mechanism for gripping onto plating scleractinian mesophotic corals is designed, realized and tested, with the goal of collecting samples via human-portable ROVs. Rotation-constrained teeth are employed to grip onto these thin structures which are abundant with surface ridges and asperities. Anisotropic contact conditions allow for gripper positional error on initial approach and grasping; the device can increase grasp engagement passively, allowing plate-like objects to be easily pushed into the gripper with forces on the order of $1\,N$. Yet, the gripper can resist large pull-out forces, tested up to $57\,N$ in the lab. The gripper design is integrated with an ROV, and its capabilities are qualitatively evaluated in field tests. These trials confirm overall expected performance given real-world disturbances and variability. This cheap, additive-manufactured technology is being developed in an effort to make the ocean more accessible for scientific research.

A.1 Introduction

A substantial recent decline in coral ecosystem health has been observed globally, with areas of local extinction [13, 88]. However, little is known about the deeper corals (30-150 m depth), usually referred to as mesophotic coral ecosystems (MCEs). Scientists understand shallow coral ecosystems better than MCEs largely because of the logistical complexity of biological research in deeper waters. Physical samples of coral are usually needed for taxonomic identification, physiological assessments or genetic studies. Current sampling methods for mesophotic corals include submersibles, technical/rebreather diving and remotely operated vehicles (ROVs). ROVs allow scientists and technicians to stay safely above water, out of the extreme ocean environment. *Small-scale ROVs*, sometimes called "inspection-class" or "human-portable," with mass on the order of ~10-30 kg are an attractive technology. They can be inexpensive to purchase, maintain and operate and can be affordably deployed from a pier or yacht. This is in comparison with massive "work-class" ROVs that require large re-
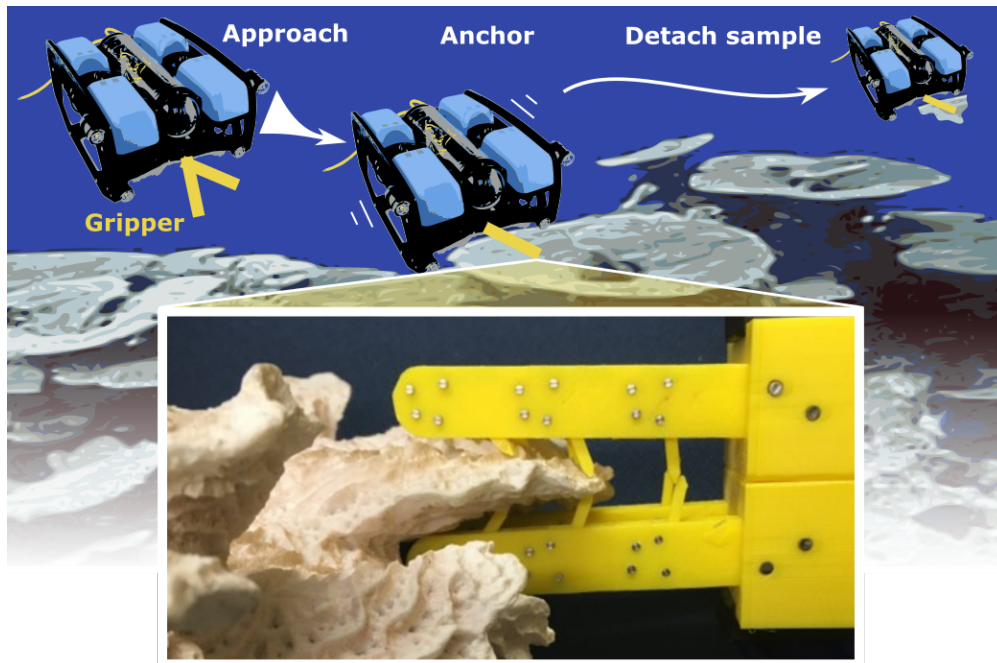
Figure A.1: A human-portable ROV, *BlueROV2*, approaches plating scleractinian corals with positional uncertainty. The ROV then grips substrate using a mechanism with rotation-constrained teeth. This jaw resists pullout forces by passively engaging the teeth on the asperities of the surface. This grasping phase enables precise interactions with the substrate with auxiliary devices, something that is particularly difficult for floating-base, small-scale ROVs. Ultimately, the ROV detaches the gripped sample from the substrate, e.g., to bring it to scientists at the surface.

search vessels with cranes to deploy. Small-scale ROV platforms have the potential to make the ocean, and MCEs, more accessible by providing a scalable field research methodology.

When feasible, divers are typically deployed to perform manual labor under sea, in part because people are highly adept at dexterous manipulation (e.g., using hand-tools to collect samples, etc.). Current ROV mobile manipulators have difficulty matching human dexterity. Manipulation tasks can be especially challenging for floating-base, small-scale, underwater ROVs with limited thrust and inertia. Ocean currents and environmental tugging on the tether make it difficult to accurately control motions and contact forces – a coral sampling task that takes a person seconds to perform could take a human-portable ROV many minutes, if achieved at all. Vehicle stabilization through clever systems designs and control schemes can improve small-ROV station keeping. For example, researchers apply momentum fly wheels to accurately control orientation [56] or use visual odometry to obtain down to 3 cm positional accuracy [17]. Wireless communication between milli-vehicles, e.g. [48], could remove the physical tether altogether, reducing external body forces. Articulated arms and
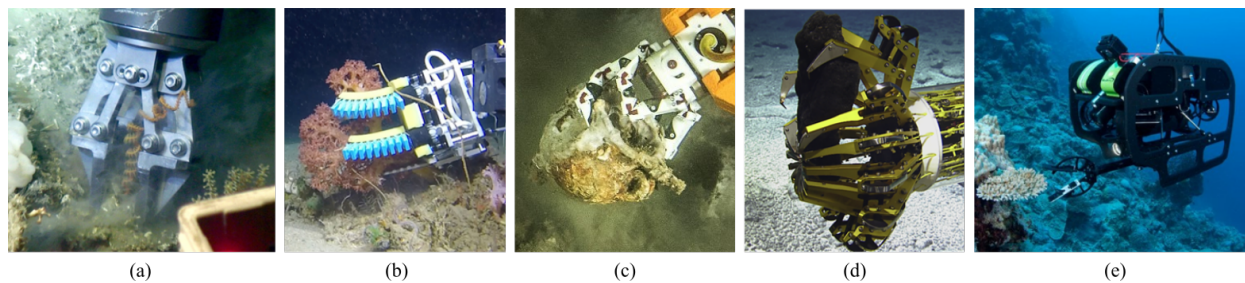
| (a) | (b) | (c) | (d) | (e) |

Figure A.2: Examples of manipulators for underwater environments: **(a)** Single degree of freedom (DOF) industrial style grippers are designed more for the handling of underwater instrumentation and structures than for the gentle grasping of delicate organic tissues, such as this Schilling gripper attempting to pinch a soft coral whip. Courtesy of Prof. Andy Wheeler, University College Cork. **(b)** The rubbery, hydraulic Harvard Red Sea gripper is extremely soft and can gently grip organic tissue. It is designed for enveloping wrap grasps. Courtesy of Dr. Kevin Galloway, Harvard University. **(c)** The Ocean One hand includes soft rubbery joints along with rigid phalanges. Its dual-stiffness transmission provides the operator with a variety of grip strength options. Courtesy of Teddy Seguin/Frederic Osada/DRASSM/Stanford University. **(d)** The JPL Nautilus Gripper consists of an under-actuated set of fingers that end in sharp tips. It is able to anchor onto rocky substrates of many different shapes and sizes. Courtesy of Dr. Aaron Parness, JPL. **(e)** The Seabotix vLVB300 ROV approaching coral to take a sample. Velcro-lined delrin sheets are added to the off-the-shelf 1 DOF gripper for better attachment. Courtesy of the XL Catlin Seaview Survey.

wrists, e.g., [11, 107, 96], have the potential to improve end-effector interactions by reducing or compensating for floating-base motions.

The strategy presented here involves anchoring the ROV onto the substrate using a gripper, such that the ROV is no longer floating relative to the substrate, as demonstrated in Fig. A.1. Using substrate contact to stabilize the body undersea is shown to be a useful way to improve ROV precision [101, 55]. Our anchoring provides more controllable and firm interaction with the coral colony using auxiliary devices, e.g., a mechanism to assist in detaching the sample from the substrate, a swab for collecting surface tissue, etc. We use a small-scale ROV with a gripper directly attached, i.e. without an articulated arm, similar in concept to [49]. We design and test the gripper capabilities, and leave the implementation of the auxiliary devices for future work.

In our case, the design of the stabilizing end-effector is tailored to handle fragile, brittle corals. The goal is to make this gripper passively forgiving to environmental uncertainty, such as skeletal geometry or errors in vehicle position relative to the reef on approach. Once a grasp is achieved the challenge becomes holding on to the coral colony with strength but without unintentionally shattering the substrate. In this work we target plating scleractinian corals (also known as "hard corals") that dominate the mesophotic zone.

Overview

We introduce an opposed-pinch end-effector that can securely grip onto plating coral structures by utilizing passive rotation-constrained teeth, pictured in Fig. A.1. In Section A.2, an overview of undersea gripper technologies is provided and prior work regarding spine gripping on rough and rocky surfaces is described. Section A.3 addresses the design of this gripper device and includes a simple model that relates pullout and internal grasp forces. A prototype is tested in the field, and observations are reported in Section A.4. Conclusions and planned future work, in Section A.5, highlight the need to integrate the anchoring gripper into a complete remotely operated sampling system.

A.2 Background: Undersea Gripping

Small-scale ROVs have been used for mesophotic coral sampling before. Researchers at the University of Queensland outfitted a rigid single degree of freedom (DOF) jaw with compliant delrin sheets and hooked (as opposed to looped) sections of Velcro (a design by ROV-technician David Whillas), pictured in Fig. A.2(e) [125]. Even with the delrin-Velcro addition, grasps on the coral proved relatively unreliable. The jaws would often slip off when trying to break-off a sample. We believe field scientists would benefit from an effective way to sample fragments of coral with human-portable ROVs, in part via more reliable gripping.

Overview of ROV Grippers

Single DOF rigid claws are common end-effectors deployed in the ocean. One example is the industrial Schilling Titan parallel gripper [102]. As shown in Fig. A.2(a), this end-effector is not specialized for the gentle manipulation of fragile organic samples, and is most suited to the precise and firm handling of structures, tools and resilient materials. It has been observed in the field that rigid 1-DOF claws tend to perform ineffectively for scleractinian coral sample acquisition [75, 29]. Grippers with compliant elements and underactuation, as in Fig. A.2(b-c), have recently been developed for nondestructive biological and archaeological tasks undersea, e.g., [37, 114, 76, 116]. Adaptive mechanisms have great potential to evenly distribute contact forces when interacting with objects [9]. This class of gripper tends to trade off precision with conformability and is well suited to gently wrapping around and enveloping objects. There are undersea gripping solutions that do not involve articulated jaws or fingers, but they typically require pumps. The universal jamming gripper modified for underwater purposes can handle irregularly shaped objects in submerged conditions [67]. Suction cups have been applied for artifact gathering in the deep-sea, such as at shipwreck sites [110].

Spines and Teeth

Sharp protrusions, often called spines, are a particularly useful way to engage with the *asperities* – bumps, ridges, cracks, notches, pits, etc. – of rough substrates. Spines can grip onto hard, rocky materials by making frictional contact. In nature, the pointed feet and stiff hairs of some arthropods interlock with asperities on the substrates to which they cling [78]. For undersea operations, the most notable application of spines is the Jet Propulsion Laboratory Nautilus Gripper [5], shown in Fig. A.2(d). Similar to a coring mechanism for consolidated rock in microgravity [93], this design uses a set of fingers, each with a sharp point, and an underactuated transmission for passive adaptation to a variety of surface and object geometries. It is specialized for high-strength anchoring and can resist the large forces and torques associated with geological drilling. Spined gripping mechanisms commonly integrate passive load sharing between contacts to maximize strength. Spine engagement tends to fail when contact slip occurs or the asperity is broken. The latter becomes more common on fragile materials. A significant body of research addresses load-sharing methods for a variety of applications, e.g., in recent articles [50, 129].

Mechanical *teeth* are similar to spines, but rely more on geometric interlocking rather than contact friction to prevent slip. Spur gears are a common example. Directional teeth are used in cable ties and ratcheting mechanisms, where motion is free in one direction and locked in the other. While spine contact conditions tend to be sensitive to tip sharpness, teeth are less sensitive to wear; teeth can be rather dull without significantly hindering performance, and can therefore be made of softer materials.

A.3 End-Effector Design

Coral Substrate Characteristics

Our study is tailored to gripping onto scleractinian corals, whose skeletons are composed predominantly of calcium carbonate. In the mesophotic region, hard corals often grow in thin structures that maximize direct sun exposure [87]; their plate-like shape allows for opposed prismatic pinching along the edge, referring to taxonomic classification [19, 31].

Pachyseris speciosa skeletons from 40 m are used in laboratory validation. Pictured in Fig. A.3, these corals can grow very close the the underlying substrate. The distal edges of these skeleton samples empirically chip under $7 \pm 2N$ with vertical cantilevered loading from a gripper tooth (N=13). The topside coral surfaces tend to have pronounced ridges and troughs with a height to width aspect ratio of $\sim 1:1$.

Device Configuration

The gripper, pictured in Fig. A.4(top), is composed of four jaws, configured in two opposing sets. Each jaw is lined with three teeth. Each tooth can rotate independently and compliantly in one direction, defined in Fig. A.4(bottom) as θ, where $\theta = 0$ is defined with the tooth
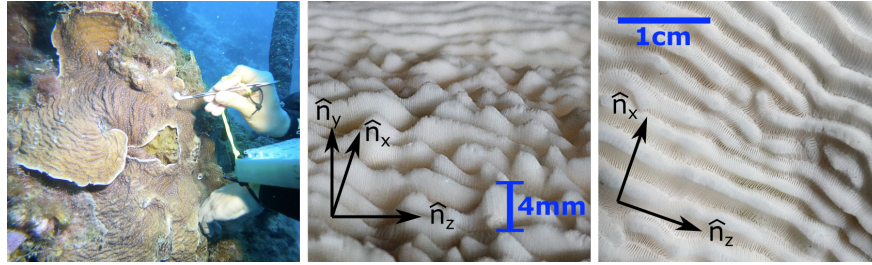
Figure A.3: (Left) Typical scleractinian corals found in the mesophotic zone in the Southern Caribbean Sea. They are plate-like in shape and pictured here are growing on a sloped surface. Courtesy of Pim Bongaerts, California Academy of Sciences. (Middle) and (Right) Close-up images of the top side of a *Pachyseris speciosa* skeleton sample taken from 40 m on the Great Barrier Reef by Pim Bongaerts from the California Academy of Sciences. Surface ridges can vary dramatically in shape and height; on this sample, the ridges have a height to period aspect ratio of ∼1:1. The ridges vary from 1-4mm in height with a spacing of 2.5-3.5mm peak-to-peak measured perpendicular to the ridge. Different coral colonies may present a wide variety of different surface patterns.

perpendicular to the jaw. As shown in Fig. A.5(a), the gripper can open and close by changing the angle between opposing jaws, α. This degree of motion is intended to increase the tolerance to vehicle positional error relative to the plate in the $\hat{n}_y$ direction upon initial approach. As the jaws close around the coral, there is a centering force due to contact that moves the coral toward the center of the jaws, as in Fig. A.5(b)-(c). The angle between a tooth and the average coral plane is defined as β (shown in Fig. A.6). During this initial grasping phase, some teeth may make contact and settle in the $-\beta$ direction because the jaws cannot close all the way to $\alpha = 0$.

Anisotropic shear contact forces, due to the rotational tooth configuration, reduce the required alignment accuracy between the gripper and substrate in the $\hat{n}_x$ direction. If just a couple teeth first engage at the edge, as in Fig. A.5(c), the grip can be improved without reopening the jaws again (c)-(e). When the gripper moves in the $-\hat{n}_x$ direction, the teeth rotate easily in $+\theta$, allowing for slipping and motion that increases the number of teeth engaged. If at any point after initial engagement is made, the jaw is pulled in the $+\hat{n}_x$ direction, the teeth will resist outward motion by jamming into the surface of the coral. As described in Sec. A.3, the harder the ROV pulls away from the coral, the greater the internal grasp force. Once fully engaged with a coral plate, as in Fig. A.5(e), the four jaw configuration can resist forces in the $\hat{n}_y$ direction and moments about $\hat{n}_x$ and $\hat{n}_z$. It is assumed that tooth engagement with surface asperities will adequately resist external forces in the $\hat{n}_z$ and $+\hat{n}_x$ directions and moments about $\hat{n}_y$.
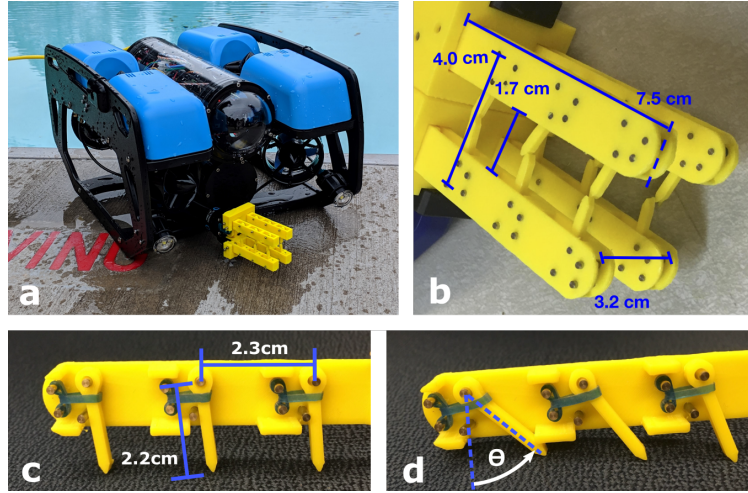
Figure A.4: Gripper prototype **(a)** mounted on the *BlueROV2*, with a linear actuator that allows for opening and closing of the jaws. **(b)** The two sets of opposing jaws, lined with teeth. The form factor is minimized given fabrication tolerances. The opening and closing of the jaws is actively controlled by the operator, and the teeth passively comply to grasped object. **(c)**-**(d)** A row of teeth in an opened jaw housing to show the details of the elastic bands that preload the teeth in a near vertical orientation.

Simplified External-Internal Grasp Force Relationship

Fig. A.6 shows the free body diagram of a single rotation-constrained tooth engaged with a coral plate. This simplified static model assumes that geometric interlocking and friction forces with the coral surface are adequate to prevent slipping, and we neglect the details of contact geometry. Shear pullout force applied externally by the thrust of the vehicle, $F_T \hat{n}_x$ is related to the internal grasp force applied by thrust $F_N \hat{n}_y$ and the angle of the tooth relative to the surface of the coral β such that $F_N/F_T = \cot(\beta)$. Note that this model is no longer relevant when a tooth reaches a hard-stop that constrains its allowable range of motion. While elastic bands provide a small moment about the tooth's mounting point on the jaw, M_k, the resultant contact force, F_k, is small compared with F_T and F_N (refer to Sec A.3) and is neglected for now.

The relationship between external pullout force magnitude F_T and internal squeeze force magnitude F_N is monotonic and nonlinear with angle β, as plotted in Fig. A.6. When the teeth are oriented with low values of β, small pullout forces can increases the internal squeeze force significantly until the jaws are wrenched apart (i.e. α increases while β decreases). This can reduce the number of teeth in contact with the surface. It may also be possible to crush especially thin, fragile pieces of the coral near the edges of the skeleton. For high β values, teeth are more likely to make shallow engagement with asperities, which may lead to superficial scratching and marring of the coral tissue as teeth slip upon increasing F_T.
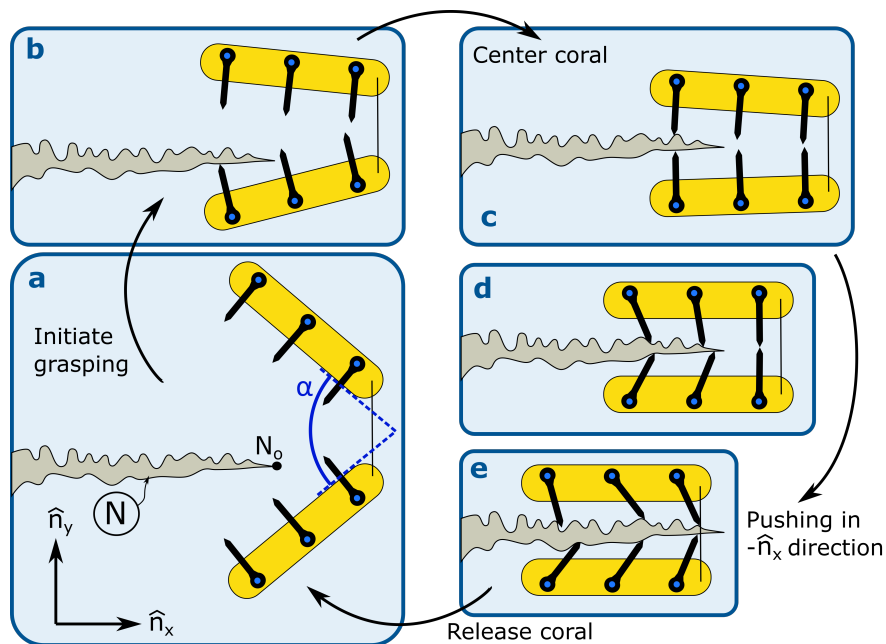
Figure A.5: Gripper diagram showing the recommended operational procedure. **(a)** The gripper is open when first approaching a coral target. **(b)**-**(c)** As the gripper closes contact is initiated and the gripper is approximately centered around the plane of the coral plate. **(d)**-**(e)** When the ROV pushed in the -$\hat{n}_x$ direction, the teeth engage more of the surface, however they resist pullout by jamming on the surface.

In a system of many rotation-constrained teeth – e.g., the 12-tooth gripper design presented in this work – each tooth may have a different orientation β_i, with subscript i denoting the tooth index. The set of tooth angles $\boldsymbol{B}$ depends on the geometry of the coral and the grasping strategy. The analysis of load-sharing between rotation-constrained teeth on *in-situ* corals is complex. It depends on an understanding of living coral colony fracture mechanics and non-idealized gripper models, and is left for future investigations.

System Implementation and Initial Evaluation

A prototype is realized for evaluating the functionality of rotation-constrained teeth on opposing jaws. The gripper has a small form factor; see Fig. A.4(b) for overall dimensions. Each tooth is 2.2 cm in length, has a 0.08 cm^2 cross-sectional area, and is spaced 2.3 cm apart along the jaw as shown in Fig. A.4(c). Pivot points of opposing teeth are 4.0 cm apart and the most distal pivot points are up to 13 cm apart when the gripper is fully open to $\alpha = 75^o$. A linear actuator integrated on the ROV articulates the gripper via a coupling linkage, and was utilized during some field tests. The maximum thickness of an object that can be grasped with the jaws closed all the way and parallel to one another is 0.9 cm. The
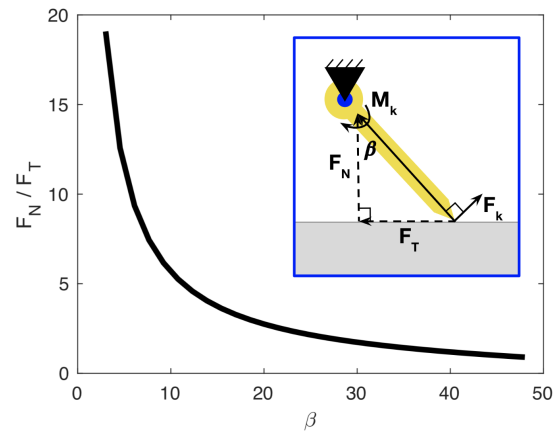
Figure A.6: Ratio of normal and pullout force for a range of tooth angles. The cotangent relationship results in a nonlinear behavior. An increase in angle β requires a much larger normal force F_N to counter the same tangent pullout force F_T. The elastic bands provide a light restorative moment M_k that results in force F_k.

device is constructed from additive-manufactured PLA parts, stainless steel dowel pins and bolts and elastic bands (raw material costs $< \$10$). Dowel pins are press-fit into the printed components and used as the tooth pivot point, hardstop, and mounting for elastic bands. The bands supply a light restorative moment to keep the teeth at θ_{min} in the absence of external loads. This moment M_k is $\sim 5.5\,\text{mNm}$ throughout tooth range of motion, resulting in a contact force F_k of about $0.25\,\text{N}$. Effective spring force varies with the aging and cycling of the elastic bands. The proposed design is easily and cheaply reproduced via desktop 3D printers and basic hardware, which can then be integrated with an existing off-the-shelf
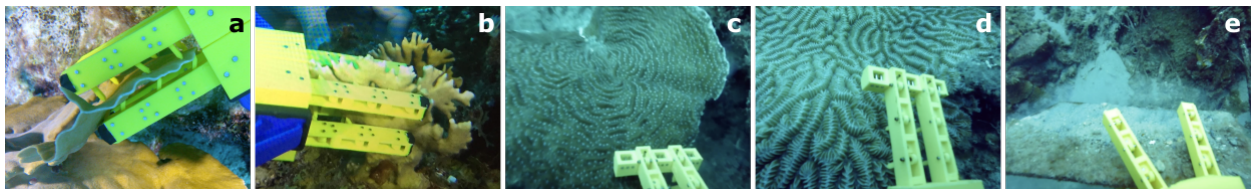

Figure A.7: Field tests of the gripper prototype engaged on coral off the coast of Curaçao. **(a)-(b)** Photos from the initial hand-held tests performed by a diver. Courtesy of Alejandra Hernández-Agreda. **(c)-(e)** Images from the onboard ROV camera during the later remote tests. **(a)**, **(c)** and **(d)** show the gripper attaching to two different plating corals. **(b)** shows a branch-type coral that has a flat enough shape to fit between the jaws in a successful grip. **(e)** shows the gripper picking up a man-made plate found at the sea floor. In all cases, the operator needed to open the jaws in order to release the object.

small-scale ROV.

Initial grasp pullout tests were conducted in the lab on *Pachyseris speciosa* specimen with forces applied in the $\hat{n}_x$ direction. Grasp failure due to asperity fracture occurred with pullout forces of up to $57\,\mathrm{N}$. From these tests, we found the blunt plastic teeth adequate for strong engagement between the gripper and the ridged coral substrate. A typical thin-plating coral insertion, with good alignment between the plate and the center of the gripper, requires forces on the order of $1\,\mathrm{N}$ in the $-\hat{n}_x$ direction; this force is much lower than for pullout, demonstrating the gripper's anisotropic behavior.

Printed plastic parts are easy to manufacture, but the material generally yields under low stresses. Tooth breaks are another common failure mode observed with our device. When the tooth is normal to the substrate plane, i.e. $\beta = \theta = 0$, pullout forces will load the tooth in a bending moment about the hardstop located halfway along the tooth length. Five individual teeth were loaded analogous to this circumstance, under 3-point bending, until failure. A hand-held Mark-10 Series 4 force gauge measured the breaking force to be $39 \pm 3\mathrm{N}$. This corresponds to the maximum tangential force a single tooth can apply to the substrate before it breaks. While this failure mode can be viewed as a strength limitation for the device, it may also acts as a mechanical fuse at times to prevent damaging the coral under accidental loading by a single tooth. Changing the dimensions (e.g., length or thickness) of the tooth will alter the loading conditions under which it breaks. The 12-tooth gripper design presented in this work provides some redundancy, such that it may still function adequately even after a tooth breaks.

A.4 Field Testing

Real-world functionality of the gripper with rotation-constrained teeth was evaluated during two field missions off the coast of Curaçao. They were conducted at the CARMABI (Caribbean Marine Biological Institute) Research Station, Willemstad, in October 2018 and February 2019. The initial tests in October 2018 involved a fully passive hand-held prototype with fixed parallel jaws. It was controlled manually by a diver, and qualitatively tested for ease of attachment and security. Fig. A.7(a)-(b) demonstrates the compliance and adaptability of the teeth to a wavy plating coral specimen and a flat branching coral. The second set of tests in February 2019 used a similar gripper integrated on the *BlueROV2*, an open-source ROV platform from Blue Robotics. It actively opens and closes the jaws using the Blue Robotics Newton Subsea Gripper's linear drive and housing. The gripper is located on the vehicle such that it is visible via the on-board front viewing camera. Fig. A.7(c)-(e) are images taken from that camera during grasping of two different plating corals (c)-(d) and a man-made tile found on the sea floor (e). In cases (c) and (d), the operator applied external forces via the thrusters in order to test grip resiliency and in (e) the item was successfully picked up. In all cases, the gripper kept its hold on the object until the remote operator chose to open the gripper. The ROV's thrusters were directly controlled via manual input commands. As described in Sec. A.1, significant tether disturbance forces made simultaneous

operation of the vehicle's motion and the gripper challenging. Especially on final approach to the target, sudden motions forward and backward in the $\hat{n}_x$ direction caused unintended collisions between the gripper and the coral. The ROV reached $80\,\mathrm{m}$ of depth during this second mission, but only tested the gripper on relatively shallow, thick-plating corals as to not unnecessarily damage the deeper, more fragile ecosystem.

Operating in a real-world ocean environment illustrated the advantages and shortcomings of this toothed gripper design. Qualitatively, large α values upon initial target approach did improve grasp success. However, the thick jaws made it difficult to align with structures in cluttered or sloped environments. We found that, once engaged, a pair of teeth would not likely slip off of the surface, and it was possible to improve engagement by pushing the gripper in the $-\hat{n}_x$ direction. Tooth breakage was a common grip failure mode observed in the field, when using the articulated gripper on the ROV; it appears that a lower number of teeth engage with the surface, increasing individual tooth stress. This is different from the passive design tested during the first mission. We suspect that this is due to the dexterity of the human-diver operating the hand-held version, and to the extra device flexibility introduced by the actuator and plastic linkage transmission of the articulated ROV version.

A.5 Conclusion

The design and evaluation of a gripper for sampling scleractinian mesophotic coral with a human-portable ROV was conducted both in lab and in the field. Rotation-constrained teeth of the device maintain a grasp on the coral with the intended anisotropic behavior. The details of the design, e.g., parameters like tooth angle relative to the coral plate, influence the interaction forces and the ultimate strength of the anchor. Real-world operation presents new challenges for the load sharing between multiple tooth contact points. This device is intuitive to construct and operate. It is one step towards the overall vision of a remote manipulation system that collects and brings coral samples to scientists on the surface in a safe, effective and scalable way.

Future Work

Scleractinian mesophotic corals grow in complex and irregular ways. Understanding the properties and variations in the mechanics of these natural materials can enable new design considerations, such as robust distribution of contact forces across a variety of substrate parameters. Thus far, we address the application of 1-dimensional pullout forces due to ROV thrust; 6-dimensional external wrench loading of these brittle and fragile substrates is a topic for future work.

The overall vision of the project is to create a fully integrated, semi-automated system capable of the entire sampling task. Ongoing work addresses the implementation of auxiliary mechanisms for performing sample detachment, and the sensing, control and automation of robotic behaviors to enhance the efficiency and ease of operations. The focus will remain

on making a system that can be affordably adopted by a wide range of marine science labs. We hope to enable more frequent and productive interactions with mesophotic corals in the field in order to better understand these enigmatic ecosystems.

A.6 Acknowledgements

Appendix B

Photos

B.1 From field testing

Below are photos from field testing the coral sampling robot detailed in Appendix A. In February 2019, we conducted a field test off the coast of Curacao at CARMABI (Caribbean Marine Biological Institute).

(a) Cleaning watertight seals on ROV where we could find clean space, in a biology wet lab.

(b) Preparing equipment in the morning for ROV testing and SCUBA diving.

Figure B.1: Field test at CARMABI, Curacao (Feb 2019). Photos courtesy of Kathryn Whitney from the California Academy of Sciences.
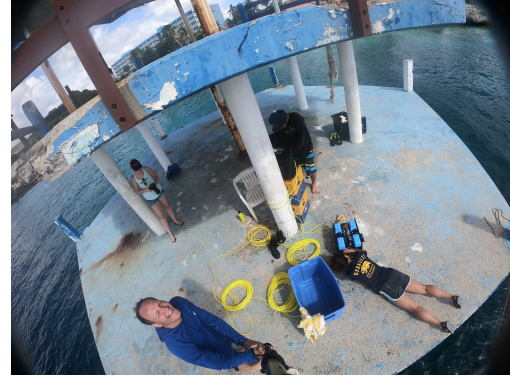
Figure B.2: Field test at CARMABI, Curacao (Feb 2019). Photos from the deployment island, courtesy of Kathryn Whitney and Pim Bongaerts from the California Academy of Sciences.

(a) System check on dry land.

(b) Dr. Rene van der Zande piloting ROV in ergonomic setup with screen cover to reduce sun glare.

Figure B.3: Piloting the ROV. Field test in CARMABI, Curacao (Feb 2019).

In March 2020, we conducted another field test off the coast of Moorea, at CRIOBE (Center for Island Research and Environmental Observatory). The upgraded system included an improved gripper, another end-effector for breaking off coral pieces, and a modified ROV thruster configuration for improved mobility.
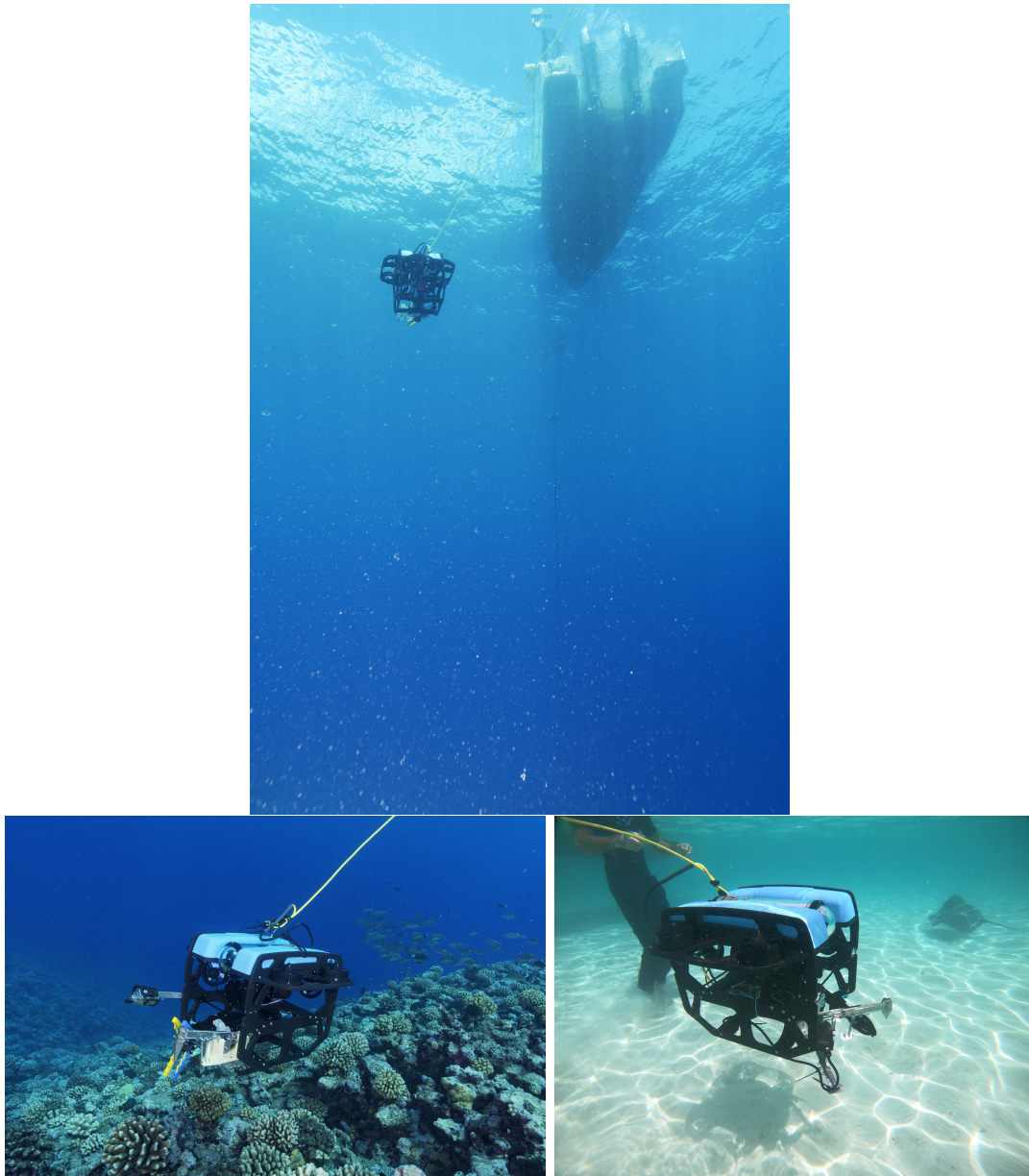
Figure B.4: ROV during underwater testing in CRIOBE, Moorea, French Polynesia (Mar 2020).
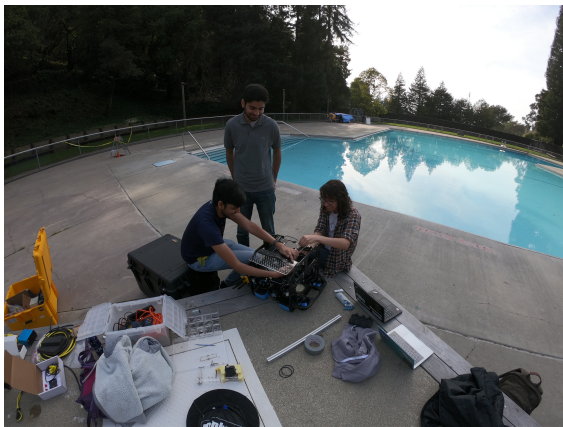
(a) Dr. Serge Planes, Professor Hannah Stuart, and Professor Vincent Creuze on boat en route to dropoff to access deeper waters.

(b) Screen of live video feed during coral sampling. Note the glare even with black sun shade.

Figure B.5: Field test in waters off Moorea, French Polynesia (Mar 2020).

(a) Dominic Melville, Mohammad Kamil Shams, Isabel Parades preparing system for testing.

(b) ROV with new end-effectors: impact breaking and toothed gripper.

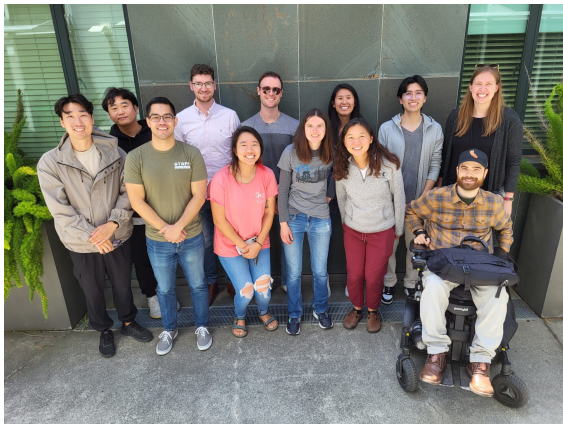Figure B.6: Pool testing ROV. Strawberry Canyon Pool in Berkeley, CA (2020).

B.2 Embodied Dexterity Group (EDG)

(a) Front row: Monica, Laura, Madison, Johnathan, Kristen, Alex. Back row: Dominic, Hannah, Ethan, Michael, Ziqi (Jan 2019).

(b) Zoom lab meeting during the COVID-19 pandemic (July 2020).

(c) Jungpyo, Deaho, Michael, Justin, Cyndia, Yuri, Laura, Erin, Monica, Wilson, Drew, Hannah (May 2023).

(d) EDG taking elevator to group meeting (2022-2023).

Figure B.7: Lab photos of Embodied Dexterity Group. Names from left to right.

(a) Michael, Cyndia, Laura, Hannah, Monica, and Sareum.

(b) Hannah and Monica after hooding.

Figure B.8: Commencement, May 2023